Revealing the Mechanical Properties of Metal Pillars Using Experimental Methods and Molecular Dynamic Simulations

by

Junhua Gu

A thesis

presented to the University of Waterloo

in fulfillment of the

thesis requirement for the degree of

Master of Applied Science

in

Chemical Engineering – Nanotechnology

Waterloo, Ontario, Canada, 2015

Author's declaration

I hereby declare that I am the sole author of this thesis. This is a true copy of the thesis, including any required final revisions, as accepted by my examiners.

I understand that my thesis may be made electronically available to the public.

Abstract

The mechanical properties of nano-crystalline copper pillars were investigated by both experimental methods and Molecular Dynamic Simulations in this study. Electron beam lithography and electroplating were used to fabricate the nano-crystalline copper pillars with various cross-sectional geometries, namely solid core, hollow, c-shaped, and x-shaped. These as-fabricated copper pillars possess three different average grain sizes, which were achieved by changing the compositions of the plating solution. Uniaxial micro-compression tests were applied to deform these nano-crystalline columnar structures. Classical Hall-Petch relationship was observed between the large-grain specimens and medium-grain specimens. An inversed Hall-Petch relationship emerged as the grain size continued to go down to the small grain size region. The mechanical behavior exhibited no signs of sensitivity to the cross-sectional geometries. To understand the deformation mechanisms, Molecular Dynamic Simulations were performed on nano-crystalline copper pillars with different dimensions. The as-constructed models displayed different mechanical behaviors under compressive and tensile deformation. This so-called compression-tension asymmetry was believed to be associated with free surface alongside the nano-crystalline pillars, where the free surface energy made opposite contributions under compression and tension. An inversed Hall-Petch trend was also observed between the nano-crystalline copper columnar structure with the grain size of 13 and 6 nm.

Acknowledgments

I would like first to thank my supervisor, Prof. Ting Y. Tsui, for his continuous support, encouragement, and invaluable help throughout my graduate studies. This thesis would not have been possible without his guidance and suggestions.

I extend my thanks to Prof. Michael K.C. Tam and Prof. Ali Elkamel for serving as my thesis examiners.

Thanks to my colleagues in the past and present: Brandon B. Seo, Joanna M. Jardin, Carlie Kong, Shweta Lad, Lilian Ho, and Abdulilah Alofi.

I appreciate for the computation resources provided by SHARCNET, Mammouth-Parallèle 2 from Université de Sherbrooke, and Guillium from McGill University, all of which are managed by Compute Canada and Calcul Quebec. The electron beam lithography was done at the Emerging Communications Technology Institute in University of Toronto.

Thanks to Dr. Steve Plimpton for developing and maintaining LAMMPS codes, Dr. Alexander Stukowski for providing the visualization software and crystal analysis codes, Dr. Pawel Pomorski for fruitful discussions, and Mrs. Mary Janet McPherson for technical writing support.

I am grateful for the financial support from my supervisor's research funds, the scholarship from University of Waterloo, and the teaching assistantship from the Department of Chemical Engineering.

Finally, thanks to my parents for their unconditional love and supports!

Table of contents

Lists of figures

Chapter 1 : Introduction

1.1 Hall-Petch and inversed Hall-Petch effect

Hall-Petch relationship was raised by E. O. Hall and N. J. Petch in the early 1950s independently [1], [2], and explains how grain size affects the strength of some materials. The relation between yield strength and grain size can be described mathematically:

$$\sigma_y = \sigma_0 + \frac{k_y}{\sqrt{d}} \qquad 1.1$$

where σ_y is the yield stress, σ_o is the material constant for the starting stress, k_y is the strengthening coefficient, and d is the average grain size. Theoretically, according to equation 1.1, infinitely strong material can be achieved with ultra-fine grain size. From micron-scale to bulk-scale grain size range, experimental data has shown that finer grain size yields higher strength [3], a trend explained by the piling up of dislocations. As the grain size decreases, the effect of dislocation blocking goes up, thereby enhancing the strength of materials.

However, when the grain size is reduced to a certain value, the Hall-Petch relationship breaks down [3][4]. As a result, nano-crystalline materials usually show an inversed Hall-Petch relationship. Typically, for some metals [6] this critical size is expected to be below 10 nm. Several models have been proposed to explain this notable inversed effect. The dislocation-based model takes the dislocation as the primary contributor for the plastic flow in nano-crystalline materials. The energy of a dislocation will be reduced by a very tiny crystal, which further affects the

dislocation motion and leads to reduced mechanical strength of the material [7]. Additionally, Molecular Dynamics Simulations [8] of some metals also indicate that the deformation of nano-crystalline material occurs via the dislocation-mediated mechanism. The grain-boundary diffusion model (Coble creep) was first considered by Chokshi et al. [4] as the dominant deformation mode in nano-crystalline solids. Furthermore, Masumura et al. [9] adopted a combined model of the competition between conventional dislocation motion and grain-boundary diffusion to explain the strength softening with the decreasing grain size. The grain-boundary shearing has been observed in various Molecular Dynamic Simulations [10], [11] and been considered as another set of models which are the main cause of the Inversed Hall-Petch effect. In addition, nano-crystalline material is also considered as a composite material with at least two phases, namely a grain interior phase and grain boundary phase, and this model is also well studied and constructed [12], [13]. Song et al. [13] suggested the grain boundary as a continuous material that is strengthened by the grains in much the same way that conventional materials are strengthened by the precipitates. Fan et al. [12] assumed the grain interior deforms elastically under external stresses, while the plastic deformation of the grain boundary layer is governed by the Maxwell's equation. Based on this two-phase model, the strength of the nano-crystalline decreases linearly with the decrease of the grain size. In order to have a deep look into this remarkable phenomenon, several lattice defects are introduced briefly here.

1.1.1 Grain boundary

In polycrystalline material, each grain is separated by the grain boundary, which is in other words the interface between grains and can be regarded as a planar defect. In each single grain, the atoms are arranged periodically, but the whole polycrystalline structure does not have a periodic arrangement of atoms because of the existence of the grain boundary. Most grain boundaries are preferred sites for the onset of corrosion and for the precipitation of new phases from the solid. They are also important to the mechanism of creep.

In general, grain boundaries can be only a few nanometers. In bulk grain-size material, each grain is large compared with the grain boundary, and the grain boundary only accounts for a small portion of the material. As more grain boundaries are introduced into structures, they block the motion of grains and increase the strength of materials. Different scenarios arise when the grain size is reduced. In nano-crystalline materials, the grain boundaries become a significant portion of the total material, and different mechanical phenomenon emerges with the increased portion of the grain boundary. In extreme cases, the amorphous material can be regarded as the 100 percent of the grain boundary, with no grain inside.

1.1.2 Dislocation

Dislocation is regarded as a line defect in material science, the presence of which strongly affects the mechanical properties of the materials. The dislocation to refer to the atomic scale defect was first raised up by Taylor [14] in 1934. Burgers vectors are used to characterize the magnitude and moving direction of the

dislocations. It is defined by means of a circuit around the dislocation on any surface that intersects the dislocation. The dislocation is considered as an edge dislocation when the burgers vector is perpendicular to the dislocation. When the dislocation is parallel with the burgers vector, it is a screw dislocation. However, in real crystals the dislocations observed are commonly mixed.

In coarse-grained materials, plastic deformation is mainly carried out by dislocations within the regular grains. Dislocations can move through the crystal grains and can interact with one another. With the assistance of the grain boundary hindering their transmission, creating a dislocation pile-up at the boundary area gives material higher strength[15]. In nano-crystalline material, a long-standing debate about the interplay of the grain-boundary and dislocation-mediated plasticity exists. Using the technique of Molecular Dynamic Simulations, Brandl et al. [16] suggested the dislocation-mediated plasticity to be a rate-limiting process determining the flow stress in nano-crystalline aluminum. This rate dependency might be understood in terms of thermally activated dislocation mechanisms, which implies the importance of the underlying grain size dependences and the possibility of the existence of a strongest size without changing the rate-limiting deformation mechanism from the dislocation-mediated to grain boundary-mediated. In an other simulation work done by Li et al. [17], results show a competing mechanism of dislocation and GD-mediated plasticity in nano-crystalline aluminum.

1.1.3 Stacking faults

Stacking faults are local regions of incorrect stacking of crystal planes associated with the presence of partial dislocation. Generally, a full dislocation has a

high energy, which is not stable, and could be split into two partial dislocations to reduce the total energy. In FCC crystals, the {1 1 1} plane, the dislocation plane and the stacking plane are all closed-packed planes. The normal stacking sequence for the FCC crystal is …ABCABCABC… When the stacking fault exists, the layer sequence may become …ABCABABC… with one layer C missing. This one-layer interruption carries a certain amount of energy, which is called stacking fault energy. High stacking fault energy means low possibility of a full dislocation splitting into two partial dislocations, and the dislocation glide dominates the material deformation. The low stacking fault energy shows a decreased mobility of dislocation in a material.

1.1.4 Twinning

Deformation twinning is a common and important phenomenon in metals and alloys. The twinning tendency of an FCC metal is largely determined by its stacking fault energy [18]. Twinning is one of the major deformation models that enable a solid to change shape under the action of applied stress at temperatures below those at which individual atoms are mobile. The classical definition of twinning requires that the twin and parent lattice be related by a reflection in some plane or by a rotation of 180 degrees about some axis [19].

Several twinning mechanisms have been raised so far. One is associated with the overlapping of the stacking fault ribbons. When two stacking faults are partially overlapped, the twin can grow thicker by adding more stacking faults on either side of the twin. However, no deformation twins of this type can grow thicker than two layers, which is because of the lack of a continuous mechanism for it to grow and

depends on the incidental overlapping of other slipping dissociated dislocations with stacking faults. There is a variant of this type twinning related to the grain boundary[20]. The deformation twins can also be formed via the emission of Shockley partials from grain boundaries. This type of twinning is commonly observed in nano-crystalline FCC metals. Another one is the dislocation rebound mechanism [21]. At the twin boundaries or the grain boundaries, the elastic field of the partial dislocation can be reflected, and the nucleation of an opposite-sign dislocation can be aided with the reverse shear field.

Twinning has been introduced in nano-crystalline copper by Lu et al. [22] to achieve ultrahigh strength and high electrical conductivity. In their study, a series of samples with different twin densities were prepared, and the tensile testing showed a trend of decreased strength with small twin density, which confirmed the strengthening effect of the twinning in nano-crystalline copper. Li et al. [23] performed Molecular Dynamic Simulation on nano-twinned copper by testing the mechanical strengths with different twin spacing. Results showed the smaller the grain size, the smaller the critical twining spacing, and the higher the maximum strength of the material.

1.2 Mechanical testing

The mechanical properties of nano- and micro-scale materials have been of the focus of research for a long time. It has been well recognized that the phenomenon under this small dimension shows a difference with that under bulk scale. Different test methods have been developed to study these novel properties, two of which will be discussed here.

1.2.1 Nano-indentation test

The indentation technique has been popular among material scientists for almost a century. It is the most-commonly used technique to perform mechanical measurement of some materials. At the beginning of the 20th century, indentation tests were first used by Brinell, with spherical and smooth balls to measure the plastic properties of materials. After which, this method was adopted by the industry and various macro and micro indentation tests were also developed [24]. In the early 1970s, it was recognized that the elastic modulus could potentially be measured through the load-displacement curve, which greatly accelerated the development of indentation tests [25]. Therefore, nowadays, the indenter systems are capable of measuring the load force as small as nanonewtons and the displacement around 0.1 nm accurately. The study of mechanical properties of materials on the nano-scale has received much attention, and the advancement of nano-indentation makes it possible to perform indentation tests in this small scale. The nano-indenter is regarded as an important tool to probe the mechanical properties of small volumes of materials and give the load-displacement curve, which contains lots of information. Many mechanical properties such as hardness and elastic modulus can be determined just from the curve.

Oliver-Pharr method [26] is the mostly used approach to analyze indentation load-displacement data. Based on Sneddon's analysis [27] for contact of an elastic half space by a rigid axisymmetric indenter, the indentation modulus, M, of a homogeneous material is related to the contact stiffness, S, and the projected area, A:

$$M = \frac{\sqrt{\pi}}{2}\frac{S}{\sqrt{A}} \tag{1.2}$$

In an elasto-plastic indentation, S is measured as the derivative of the indentation load, P, with respect to the elastic part of the unloading. The projected area, A, needs to be determined through the contact depth, h_c:

$$A = F(h_c) \tag{1.3}$$

The function form, F, is established by the experiments, and the contact area can be reached as follows:

$$h_c = h_{max} - \epsilon\frac{P_{max}}{S} \tag{1.4}$$

where the h_{max} is the maximum displacement of the indentation, and the second term is elastic deflection of the surface. It is determined by the load, P_{max}, and stiffness. The constant, ϵ, depends on the shape of the indenter, with 1 for the flat punch and 0.72 for the conical tips. As well as the modulus, the hardness can also be determined if the contact area is know:

$$H = \frac{P_{max}}{A} \tag{1.5}$$

Some disadvantages exit in this conventional indentation technique. No direct measurement can be achieved to get the flow stress, which can only be calculated with the assumption that the hardness and yield strength have linear relationship. The geometry of the indenter tip can affect the measured mechanical properties of some materials. In Mirshams's study [28], nickel has been used to test the effects of different geometries of the indenter tips. Results indicate a strong dependency of the measured values to the shape of the indenter. The highest value

was observed for the conical indenter tip, and the lowest for the Berkovich tip. The substrate effect is another concern when testing the hardness of thin films. Saha and Nix [29] conducted experiments to determine the mechanical properties of soft films on a hard substrate and hard films on a soft substrate, using the nano-indentation technique. In the case of soft films on a hard substrate, the effect of the substrate hardness on film hardness was negligible, because plastic deformation was contained within the film and the substrate yielded plastically only when the indenter penetrated the substrate. Substrate hardness was observed to affect the measured film hardness for the case of the hard film on a soft substrate, since the substrate yields at indentation depths less than the film thickness. As a result, the true hardness of the film could be determined from the indentation data only if the indentation depth was less than 10% of the film thickness.

1.2.2 Micro-compression test

Uniaxial compression test was first implemented by Uchic [30], [31] to study the size effect on the mechanical properties of some metals. This technique is evolved from the nano-indentation method, and the indenter is also used with the tip changing from Berkovich to a flat diamond tip, which allows a homogeneous stress-strain to be distributed throughout the specimen.

The specimen used in the micro-compression test is usually the pillar structures, which need special preparation steps. There are two widely used approaches, focused ion beam (FIB) milling and electroplating. The FIB milling applies localized sputtering to micro-machine small compression samples into the surface of bulk materials. FIB systems are uniquely suitable tools in their abilities to

fabricate 3-D structures while maintaining the sub-micron precision in a variety of metallic and non-metallic systems [32]. Gallium ion is commonly used in the FIB system. A drawback of this method is potential defects caused by the Ga^+ ions penetration into the pillar through the FIB milling process [33]. In addition to the Ga^+ ions implantation problem, another disadvantage of the FIB technique is that the test specimen is not free standing, since one end of pillar is fixed to bulk material. Another method to fabricate the micro-compression test specimens is electroplating. Lithography technique is first used to make patterns in the PMMA photoresist, and metals can then be deposited to these photoresist patterns. After removing the rest of the PMMA, we can get the pillar structures on the substrate. This method is Ga^+ ions free and without the concern of its induced defects.

Dr. Tsui [34]–[39] has done lots of fantastic work using the micro-compression test along with the electroplating method. Indium pillars with solid and hollow cylindrical shape were prepared using lithography followed by the electroplating fabrication method. The uniaxial compression tests of the solid pillar revealed a dramatic increase in strength over that of the bulk indium and approach nearly ideal strength [34]. The investigations of Cobalt sub-micro columnar structures with four different cross-sectional geometries show a shape-independent mechanical strength regardless of their different surface ratios [36]. Nano-crystalline nickel pillars with different grain size and dimensions were fabricated to study the grain-size and dimension-size effect on the mechanical strength of the nickel sub-micron structures. Results indicate that the larger dimension (~1000nm outer diameters) structures with finer microstructures is stronger than larger grain

size, and size dependent softening effect exists at the small grain size region (~9.4nm to 13.2 nm) [37].

1.3 Molecular Dynamic Simulations

Since the invention of the ENIAC (Electronic Numerical Integrator And Computer) in 1946, computers have changed the world dramatically. It has also made great impact in scientific researches of different disciplines. In material science [40], computer simulations allow the researchers to perform experiments under tightly controlled conditions in order to determine the specific responses to certain external stimuli. It provides a much new understanding of various phenomena. In Biology [41], computer simulation is applied to biological macromolecules to give the fluctuation in the relative positions of atoms in a protein or in a DNA as a function of time, which provides researchers with the insights into biological phenomena such as the role of flexibility in ligand binding and the rapid solvation of the electron transfer state in photosynthesis. Additionally, computer simulations are used to determine the protein structure from the NMR. In Chemistry [42], computer simulations can provide a powerful tool for understanding enzyme catalysis, and it is clarified that all properly condensed simulation studies have identified electrostatic preorganization effects as the source of enzyme catalysis. In Physics [43], computers can solve the complicated problems in the quantum world.

MD simulation deals with problem in the atomic level, which requires the specification of an empirical classical interatomic potential function with parameters fitted to the experimental data. Figure 1 shows the classification of material modeling and simulation in terms of the length. Below the atomic level is

the electronic structure. The length scale can be a few angstroms. The electrons have to be dealt with directly using the Schrodinger equation of quantum mechanics. This is an extremely computation intensive process, and the technique of *ab initio* is used. Above the atomic level, the relevant length is the microns. The simulation technique commonly used in this level is finite-element calculation method (FEM). This level is critical for the material design since many useful properties of the material are governed by the microstructures in a system. However, to carry out such calculations needs information like material-specific physical parameters from either the experiments or the calculations at atomic or electronic structure levels. To a large extent, the same can be said for the continuum level, and the parameters to perform calculations, such as computational fluid dynamics (CFD) and continuum elasticity (CE), need to be supplied externally.

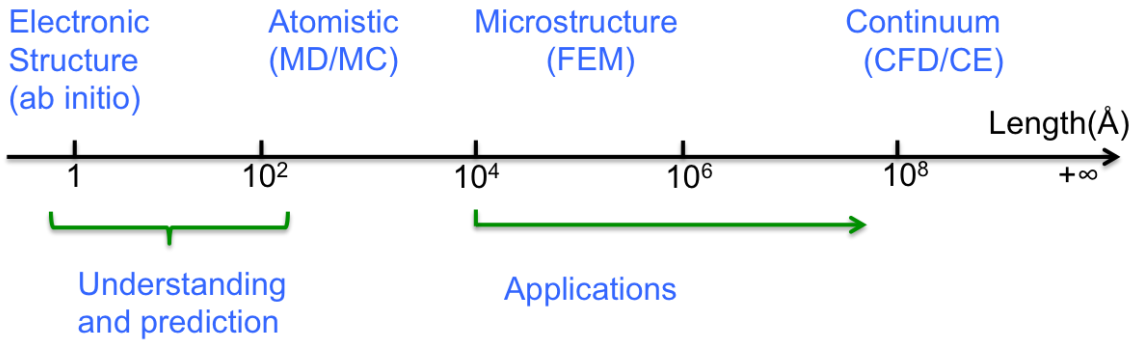

Figure 1.1 Length scale in multi-scale material modeling [44].

In Molecular Dynamics (MD) Simulations, the trajectories of atoms and molecules in the context of N-body system were solved based on the classical Newton's equation of motion. According to Newton's second law:

$$F_j^{\beta} = m_j \frac{d^2 x_j^{\beta}}{dt^2} \quad j = 1,2,\dots,N \quad \beta = 1,2,3 \qquad 1.6$$

where F_j^β is the force on atom j in the β direction, m_j is the mass of the atom j, x_j^β is the Cartesian coordinates of the atom j in the β direction. On the other hand, the force on an atom can be computed by calculating the derivation of the total energy with respect to the position of the atom, which is given as:

$$F_j^\beta = -\frac{\partial U}{\partial x_j^\beta} \quad j = 1,2,\dots,N \;\; \beta = 1,2,3 \tag{1.7}$$

where U is the potential energy of the system. Additionally, in molecular simulation, the motion of atoms is not independent of one another, thus the equation of the motion must be coupled. The Verlet algorithm has been widely used to integrate the Newton's equation of motion, and it is one of the simplest and most efficient approaches, of which the basic idea is to write two Toylor expansions for the position *r(t)*, one forward and one backward in time:

$$r(t+\Delta t) = r(t) + \frac{dr}{dt}(t)\Delta t + \frac{d^2r}{2dt^2}(t)\Delta t^2 + \frac{d^3r}{6dt^3}(t)\Delta t^3 + O(\Delta t^4) \tag{1.8}$$

$$r(t-\Delta t) = r(t) - \frac{dr}{dt}(t)\Delta t + \frac{d^2r}{2dt^2}(t)\Delta t^2 - \frac{d^3r}{6dt^3}(t)\Delta t^3 + O(\Delta t^4) \tag{1.9}$$

Adding the equation 1.8 and equation 1.9 gives:

$$r(t+\Delta t) = 2r(t) - r(t-\Delta t) + \frac{d^2r}{dt^2}(t)\Delta t^2 + 2O(\Delta t^4) \tag{1.10}$$

This is the basic form of the Verlet algorithm, and the third term in the equation is just the force divided by the mass. From the equation 1.10, we can see the position of certain atom at time t can be simply determined by its previous position. The error in the Verlet algorithm is of the order of Δt^4 where Δt is the time-step in the

simulation. Furthermore, the velocity can also been obtained by subtracting equation 1.8 with equation 1.9:

$$r(t+\Delta t) - r(t-\Delta t) = 2\frac{dr}{dt}(t)\Delta t + O(\Delta t^3) \quad 1.11$$

$$v(t) = \frac{dr}{dt}(t) \approx \frac{r(t+\Delta t) - r(t-\Delta t)}{2\Delta t} \quad 1.12$$

As we can see from the all above equation, the time-step, Δt, plays an important role in the MD simulation, which must be appropriately chosen. Theoretically, the smaller the time-step is, the more detailed vibration of atoms can be captured throughout the whole simulation period. However, due to the limitation of current computation power, too small time-step means much more resources need to be pledged into the simulation. Therefore, a characteristic time can be derived based on intrinsic material properties:

$$\tau = \sigma\sqrt{\frac{m}{\epsilon}} \quad 1.13$$

where the σ is bond length, m is atomic mass, and ϵ is cohesive energy of a bulk atom. The time-step is then to be chosen around 0.005 τ. Actually, utilizing quantum mechanics is a more accurate approach in simulations by solving the time-independent Schrödinger equation. However, it is too computation intensive, and even for very small model using most advanced computation resources, this is still not realistic.

1.3.1 Embedded-atom method potential

Embedded-atom method (EAM) potential is a semi-empirical, many-atom potential for computing the total energy of metallic system developed by Daw et al.

[45]–[47] in 1983. It is extremely usefully dealing with large unit cell systems. For metals with empty or filled d bands, it is also appropriate. Using the EAM potential, point defect, alloying, grain boundary structure and energy, dislocations, fracture etc. can be investigated. The total energy, E_i, of atom *I* is given by:

$$E_i = F_\alpha(\sum_{j \neq i} \rho_\beta(r_{ij})) + \frac{1}{2}\sum_{j \neq i} \phi_{\alpha\beta}(r_{ij}) \quad 1.14$$

where F is the embedded energy function, ρ is the electron density, ϕ is the two body pairwise potential between atom *i* and *j* separated by the distance r_{ij}. Then the total internal energy of all the atoms on the system E_{tot} is:

$$E_{tot} = \sum_i E_i \quad 1.15$$

Unlike pairwise potential, EAM potential also takes electron density into consideration. In metallic system, each atom is embedded in a host electron cloud system created by its neighboring atoms, and this interaction is much more complicated than simple pairwise model. However, it is necessary to include this electron gas influence on the energy to describe a multi-body interaction.

The EAM potential has been used to solve various problems related to the properties of the metals, and the information on the structure, phase transitions, diffusion, and dynamics can be obtained from the EAM. Foiles [48] used the EAM potential to compute the structures of twist grain boundary in gold. The atomic positions near the boundary are computed and found to agree with the X-ray diffraction results well. Majid et al. [49] have also carried out a joint experimental and theoretical study of the grain boundary in the gold. They computed the X-ray diffraction expected from the grain boundary based on the atomic structure that is

simulated from the EAM potential. These computed intensities were then compared with the experimental X-ray diffraction intensities. The results showed a reasonable agreement between the computed and measured intensities suggesting that the EAM can provide a good description of the grain boundary structure.

EAM potential is also a good candidate to investigate the mechanical properties of the metals. Dislocation motion plays an important role in the mechanical properties. With the copper EAM potential, the perpendicular intersection of extended dislocation has been studied [50]. This investigation provides insights into some complex atomistic process, such as junction formation, unzipping, partial dislocation bowing, cutting and unit jog formation in face-centered cubic lattice. Kelchner et al. [51] modeled an indentation on a metal surface by combining a hard-sphere indenter and an atomic metal with EAM potential. It provided atomistic imaging of the dislocation nucleation during the displacement controlled indentation process. Specifically, for gold surface, nucleation of the partial dislocation loops can be observed under the indentation area.

In Zimmerman's work [52], different EAM potentials have been tested to investigate the stacking faults energy of different metals. The resulting curves showed similar characteristics but vary in their agreement with the experimental estimates of the intrinsic stacking faults energy. These curves were also used to estimate the unstable stacking fault energy that was a quantity used in the criterion for the dislocation nucleation. With the establishment of the dimensionless unstable stacking faults energy in their work, they found this quantity was constant, which

implied that for a given type and amount of deformation, the material response is identical irrespective of specific material model, if the crystal structure and the operating slip lane are the same.

1.3.2 Boundary conditions

Typically, most molecular simulations are carried out inside a simulation box, which contains all the atoms during the whole process of simulation. The simulation box occupies a defined volume in coordinate space, and all the integration calculation is restricted to this space. At the edge of the simulation box, one of the two boundary conditions, periodic boundary condition and non-periodic boundary condition, has to be assigned, and these conditions will be applied in each of the primary directions, orthogonal to the box edges.

It is well known that the behavior of a finite system is very different from that of an infinite system. In some cases, properties at the bulk scale are desired when performing Molecular Dynamic Simulations. With a reasonable computation time and resources, the typical number of particles can be handled in MD simulation can be more than a million. However, compared with a macroscopic system, this number of particles is still not enough. In a macroscopic system, only a small portion of particles is located at the surface area, while for a typical simulation system, the fraction of surface particles is much more significant and the behavior would even be dominated by the surface effects. Therefore, the periodic boundary condition was adopted to solve both the problem of the finite size of the simulation system and to minimize the surface effects to get the macroscopic properties. When the periodic boundary condition is imposed, particles located at the boundaries of the simulation

box will not be considered as free surface particles, and if the periodic boundary condition is imposed at all the directions of the simulation box, that group of particles inside the simulation box will be treated as a representative section of a continuous bulk material. In the pioneer MD simulation work done in 1998 [40], the periodic boundary condition was imposed at all the three spatial directions. The effect of the varying grain sizes on the mechanical strengths of nano-crystalline copper was investigated. The periodic boundary is very important in this case, since surface effect also has an influence on the mechanical strength, which will interfere with the grain size effect.

Non-periodic boundary condition is also used to meet some specific requirements. In some cases, free surfaces are desired in the simulation model, and the non-periodic boundary condition will be adopted in that particular direction. If the non-periodic boundary condition was specified in one direction, the simulation represents a sheet of atoms of finite thickness and infinite span. When non-periodic boundary condition is specified in two directions, a rod of atoms is represented of infinite length but with a finite cross-sectional geometry. In the simulation work of nanowires (NT) and nanotubes (NW) [53], [54], the non-periodic boundary condition is widely used, and in most cases, the boundary condition is imposed along the object's axis direction and the lateral directions are kept free, which enables the investigation of the effects of NT/NW size and free surfaces on the mechanical strengths.

1.3.3 Energy minimization

Energy minimization calculation (Molecular static method) is performed without the thermal contribution to the total energy of the system. This calculation is solely based on the positions of the atoms according to the interatomic potential, which is independent of time. The molecular dynamic calculations give the physical motion of atoms, including velocities and positions at each time step, which is relatively computational expensive and its feasibility is limited by the time scale. In most cases, when the simulation objects are built, they are usually not at the energetically favorable sate. As a result, energy minimization steps are applied to find a configuration of system with minimum potential energy at the beginning of the whole simulation process. Performing an energy minimization of a system is by iteratively adjusting the atoms coordinates. The iterations are terminated when one of the stopping criteria is satisfied. These stopping criteria can be included but not limited to stopping tolerance of energy, stopping tolerance of force etc. Addtionally, in all cases, the objective function being minimized is the total potential energy of the system as a function of the N-atom coordinates:

$$E(r_1, r_2, \dots, r_n) = \sum_{ij} E_{pair}(r_i, r_j) + \sum_{ij} E_{bond}(r_i, r_j) + \sum_{ijk} E_{angle}(r_i, r_j, r_k) + \sum_{ijkl} E_{dihedral}(r_i, r_j, r_k, r_l) + \sum_{ijkl} E_{improper}(r_i, r_j, r_k, r_l) + \sum_{fix} E_{fix}(r_i) \quad 1.16$$

where the first term is the sum of all non-bonded pairwise interactions including the long-range Columbic interactions, the second term to fifth term are bond, angle,

dihedral and improper interactions respectively, the last term is due to the fixes in the simulation process, which act as constraints or apply forces to the atoms.

Many algorithms can be used to perform the energy minimization calculation, such as Monte Carlo method, genetic algorithm, and conjugate gradient method. In my simulation work, conjugate gradient (CG) method was applied to carry out the energy minimization step. The CG method is designed to solve the linear equation:

$$\boldsymbol{A}\boldsymbol{x} = \boldsymbol{b} \tag{1.17}$$

where $\boldsymbol{x}$ is an unknown vector, $\boldsymbol{b}$ is a known vector, and $\boldsymbol{A}$ is the matrix, which is symmetric and positive defined. The corresponding quadratic form of equation 1.17 can be written as:

$$f(\boldsymbol{x}) = \frac{1}{2}\boldsymbol{x}^T\boldsymbol{A}\boldsymbol{x} - \boldsymbol{b}^T\boldsymbol{x} + c \tag{1.18}$$

$f(\boldsymbol{x})$ is minimized by the solution to the equation 1.17. In MD simulation, at each iteration the force gradient is combined with the previous iteration information to compute a new search direction conjugate to the previous search direction and this process will stop upon certain criteria is satisfied to get the minimum energy configuration of the simulation system.

1.3.4 Thermostat and Barostat

In order to maintain reasonable computation power consumptions, certain constraints have to be applied to the MD simulation process. In addition to the boundary condition control, the ensemble types also play an important role. In MD simulations, different variables like amount of particles (N), temperature (T),

volume (V), pressure (P), energy (E), and enthalpy (H) can be controlled under different ensemble types. In my MD simulation, two ensemble types, canonical ensemble (NVT) and isothermal-isobaric ensemble (NPT), are applied to simulate metal structure deformation processes.

1.3.4.1 Canonical ensemble

In the canonical ensemble (NVT), the amount of particles (N), volume (V), and temperature (T) are kept as constant. This approach is developed by Nose and Hoover [55]–[58], and based on an extended Lagrangian equation. The extended Lagrangian approach was originally introduced by Andersen [59] in the context of constant-pressure simulation, and Nose [55] made the best of it by adding additional coordinates and velocity. In the N-body system, the extended Lagrangian is defined as:

$$L = \sum_{i=1}^{N} \frac{m_i}{2} s^2 \dot{r}_i^2 - \phi(r^N) + \frac{Q}{2}\dot{s}^2 - lkT_{eq}\ln(s) \qquad 1.19$$

where s is the introduced additional degree of freedom, and it acts as an external system. The interaction between the physical system r and additional system s is expressed through the scaling of the velocity of the particles, which can be interpreted as an exchange of heat between the physical system and the external system. The external system can be regarded as a heat reservoir. The second term is potential energy. The third term is the kinetic energy, which is introduced in order to be able to construct a dynamic equation for s. The parameter Q is the effective mass associated with s and determines the time scale of the temperature fluctuation. The last term is the potential energy related to the external system s, in which l is a

fixed parameter representing the number of degrees of freedom in the physical system, k is the Boltzmann constant, and T_{eq} is the externally set temperature. The Hamiltonian of this extended system is given by:

$$H = \sum_{i=1}^{N} \frac{p_i^2}{2m_i s^2} + \phi(r^N) + \frac{p_s^2}{2Q} + lkT_{eq} \ln(s) \tag{1.20}$$

where p_i and p_s are the momenta conjugate to physical system r and external system s, and they can be derived directly from the equation 1.19,

$$p_i = \frac{\partial L}{\partial \dot{r}_i} = m_i s^2 \dot{r}_i \tag{1.21}$$

$$p_s = \frac{\partial L}{\partial \dot{s}} = Q\dot{s} \tag{1.22}$$

The equations derived by Nose can be further simplified through Hoover's work [57]. The thermodynamic friction coefficient ξ is introduced, and the equations of motions become:

$$\dot{p}_i = -\frac{\partial \phi(r^N)}{\partial r_i} - \xi p_i \tag{1.23}$$

$$\dot{r}_i = \frac{p_i}{m_i} \tag{1.24}$$

$$\dot{\xi} = \frac{\sum_i \frac{p_i^2}{m_i} - lkT_{eq}}{Q} \tag{1.25}$$

where p_i and r_i are the momenta and coordinates of the physical system, respectively. The friction constant ξ is a variable that characterizes the coupling of the physical system and the external system. The choice of the value has a great influence on the detailed nature of dynamics.

1.3.4.2 Isothermal-isobaric ensemble

In the isothermal-isobaric (NPT) ensemble, amount of particles (N), pressure (P), and temperature (T) are conserved. In addition to the thermostat, the barostat is also needed to control the system. In order to maintain a fixed internal pressure, the volume of system must be allowed to change, and the system also exchanges heat with a thermal reservoir, maintaining a fixed temperature. Compared with NVT ensemble, it is somewhat more difficult to generate because both the instantaneous pressure fluctuation and correct kinetic energy should be generated according to the distribution function. The NPT ensemble is often used for purposes of equilibrating a system, allowing it to adjust to an appropriate density for computing equilibrium properties under isobaric conditions, such as Gibbs free energy [60].

The idea of the NPT is straightforward from the NVT ensemble. Hoover [58] introduced the reduced coordinates:

$$x = \frac{r}{V^{\frac{1}{D}}} \tag{1.26}$$

where V is the volume, and D is the dimension of N-body system. The equations of motion become:

$$\dot{p}_i = -\frac{\partial \phi(r^N)}{\partial r_i} - (\dot{\epsilon} + \xi) p_i \tag{1.27}$$

$$\dot{x}_\iota = \frac{p_i}{m_i V^{\frac{1}{D}}} \tag{1.28}$$

$$\dot{\varepsilon} = \frac{\dot{V}}{DV} \tag{1.29}$$

$$\ddot{\varepsilon} = \frac{(P - P_{ext})V}{\tau^2 kT} \tag{1.30}$$

where ε is the strain rate, P_{ext} is the fixed external pressure, and τ is the relaxing time. From the equations above, we can see the momentum of the particles changes through both their adiabatic coupling to external pressure P_{ext} by the strain rate ε and relaxing time τ, and coupling to an external heat bath s of temperature T by parameters Q and ξ.

1.3.5 Virial stress

Virial stress is the mostly used definition of stress in the discrete particles, which was generalized from the virial theorem. The virial theorem was developed by Clausius [61] to determine the stress field applied to the surface of a fixed volume containing interacting particles. The basic idea of the virial theorem is to relate the kinetic energy of a system to the inter-particle forces acting on them, and the expression of the kinetic energy is:

$$E_k = -\frac{1}{2}\sum_{i=1}^{N} F_i r_i \tag{1.31}$$

where N is the total number of particels in a system, F_i is the inter-particle force on particle i, and r_i is coordinates. The virial stress for a system [62][63] based on the generalization of the virial theorem includes two parts and is defined as:

$$\Pi^{\alpha\beta} = \frac{1}{\Omega}\left(-\sum_i m_i v_i^{\alpha} v_i^{\beta} + \frac{1}{2}\sum_i \sum_{i\neq j} F_{ij}^{\alpha} r_{ij}^{\beta}\right) \tag{1.32}$$

where Ω is the volume of the system, m_i and v_i are the mass and velocity of the particle i, F_{ij} and r_{ij} are the force and distance between the atom i and atom j, and the indices α and β denote the Cartesian components. The first summation term on the right of the equation 1.32 is due to the thermal vibration and it is zero in a static

simulation. The second summation term in the right side of the equation 1.32 is owing to the inter-particle force. Furthermore, the virial stress at the atomic level can be decomposed from the equation 1.32, and the atomic level virial stress for atom *i* is defined as:

$$\pi_i^{\alpha\beta} = \frac{1}{\omega_i}\left(-m_i v_i^{\alpha} v_i^{\beta} + \frac{1}{2}\sum_{i \neq j} F_{ij}^{\alpha} r_{ij}^{\beta}\right) \quad 1.33$$

$$\Pi^{\alpha\beta} = \frac{1}{\Omega}\sum_i \omega_i \pi_i^{\alpha\beta} \quad 1.34$$

$$\Omega = \sum_i \omega_i \quad 1.35$$

where ω_i is the effective volume of atom *i*, and it can be approached by dividing the volume of whole particle system with the number of particles.

In MD simulation, virial stress is widely used to get compression flow stress, tensile flow stress, and even Young's modulus. Diao et al. [62] got the Young's modulus of the gold nanowire by fitting the relationship between the virial stress and the strain, showing an increase in Young's modulus with a decrease of cross-sectional area in the nanowires that did not undergo a phase transformation experience. Cao et al. [64] revealed the relationship between the grain size and maximum flow strength of nickel nanowires through the flow stress curve, which was calculated by adding the local virial atomic stress along the loading direction of all atoms and divided by the deformed nanowire volume.

1.3.6 Voronoi tessellation

In MD simulation, the model generation is of great importance, and it is used to resemble the objects in real world. For single-crystalline material, the construction of model is just the repeat of the basic lattice structures. However, for poly-crystalline structures, the grains should be arranged randomly and Voronoi tessellation technique has been used to generate the model [65].

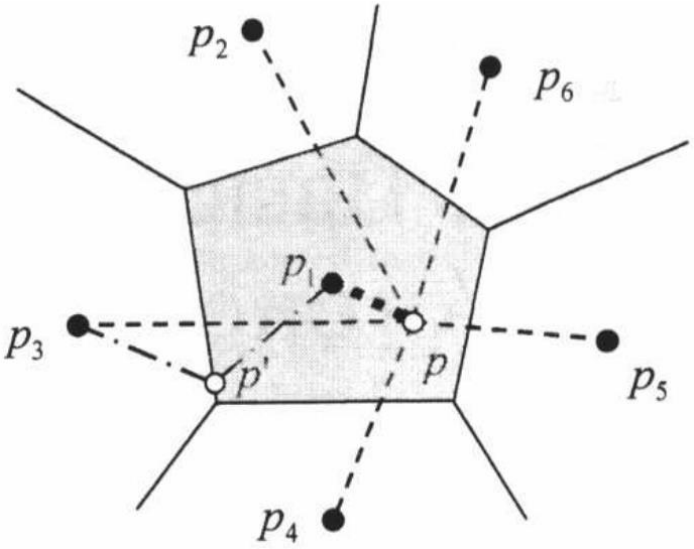

Figure 1.2: A 2-D Voronoi diagram [66].

The Voronoi tessellation, also called Voronoi diagram or Voronoi decomposition was defined by Georgy Voronoy, a Russian-Ukrainian mathematician. The Voronoi diagram of a set of sites is a collection of regions that divide up the plane. Each region corresponds to one of the sites, and all of the points inside the region will be closer to the corresponding site than any other site. Where there is no closest point, there is the boundary. As illustrated in figure 1.1, the point p is closer to p_1 than any other points. The point p' is on the boundary between p_1 and p_2, which is equal distance to the both points. The shaded region is the set of points that are all

closer to p_1 than any other points. Hence adjacent regions overlap only on their boundaries. The set of the regions is collectively exhaustive and mutually exclusive except for the boundary parts.

Similarly, 3-D Voronoi tessellation is used to divide the space into several parts. In the grain configuration generation process of the poly-crystalline models, the dimension of the model and the amount of the grains in the model are first defined. Then each grain will be assigned to one point just like p_1 to p_5 in figure 1.1, based on which the polygons would be constructed. All the Voronoi tessellations in my MD simulations are performed using the Quickhull algorithm that is implemented in the software called Qhull [67].

1.3.7 Structure identification methods

The product of MD simulation is usually a set of combinations of particle coordinates, which cannot give much useful information without appropriate interpretation. In order to visualize and analyze the results, the different structure types, such as face centered cubic (FCC), body centered cubic (BCC), hexagonal closed packed (HCP), should be assigned to certain particles based on their local environment, and the coloring scheme will be performed according to their different structure types. Furthermore, dislocations, stacking faults and other structure defects can be addressed from the observation of the structure identification. Many computational structure identification methods have been developed in the past, and I will discuss two mostly used ones, common neighbor analysis (CNA) [68] and bond angle analysis (BAA) [69].

1.3.7.1 Common neighbor analysis

Common neighbor analysis (CNA) method employ complex, high dimensional signatures to characterize arrangements of atoms, which is usually better in discriminating between several structures, and the characteristic signature is computed from the topology of bonds that connect the surrounding atoms. In the CNA method, one important parameter of cutoff distance has to be defined. Usually, two atoms are considered to be neighbors, when they are within the specific cutoff distance. For the FCC structure, the cutoff distance is set to be halfway between the first and second neighbor shell [70]. As shown in figure 1.2, for particle p, the first nearest and second nearest particle are p_1 and p_2 respectively, and the cutoff distance of the FCC structure is defined as:

$$r_c = \frac{1}{2}(L_1 + L_2) \approx 0.854a \qquad 1.36$$

where a is the lattice constant of the FCC structure, and it differs with different types of material. Similarly, the cutoff distance of BCC and HCP structure can also be obtained with the this approach.

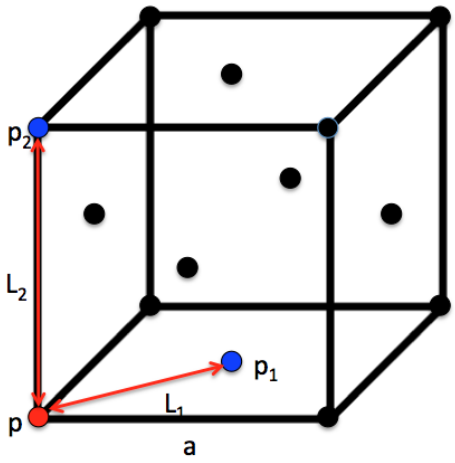

Figure 1.3: Illustration of FCC lattice structure.

To assign a local crystal structure to an atom, three characteristic indices should be computed for each of the N-neighbor bonds of the central atom. The index, *j*, is the number of neighbor atoms of the central atom and its bonded neighbor have in common. The index, *k*, is the total number of bounds between these common neighbors. The index, *l*, is the number of bonds in the longest chain of bonds connecting the common neighbors. The amounts of these three indices set, which are compared with a set of reference signatures, assign a structural type to the central atom. For example, the atom in BCC structure has eight bonds of index (6 6 6) and six bonds of index (4 4 4). Any central atom corresponding to these indices set will be assigned as a BCC atom.

1.3.7.2 Bond angle analysis

The bond angle analysis (BAA) was proposed by Ackland and Jones [69], which has also been named as Acklend-Jones Analysis method. The BAA method is based on a heuristic algorithm to define and analyze the local structure and display the results by color-coding particles to distinguish the regions with BCC, FCC or HCP structures. As shown in figure 1.3, the angular distribution function is described by eight numbers (X_i). The number of angles in regions of θ_{ijk} reflects the angles formed between the central atom *i* and neighbor atoms *j* and *k*. When three atoms are in a straight line, the angle cosine turns to X_0 region, which is a very useful measure, since most perfect crystalline structure has a higher local symmetry than the defects. It is a challenge to distinguish FCC structure from the HCP structure. Although there is an obvious difference in the X_2 peak in the HCP structure, it will overlap two other peaks when it is too wide. As a result, a combination of the

numbers of certain X_i will be used. For example, both (X_0, $X_0+X_1+X_2$) are examined, of which, for FCC structure, the value is (6, 6) and, for HCP, the value is (3, 9). This usage of the combination has the advantage of eliminating the effects of the overlapping between the nearby neighbors.

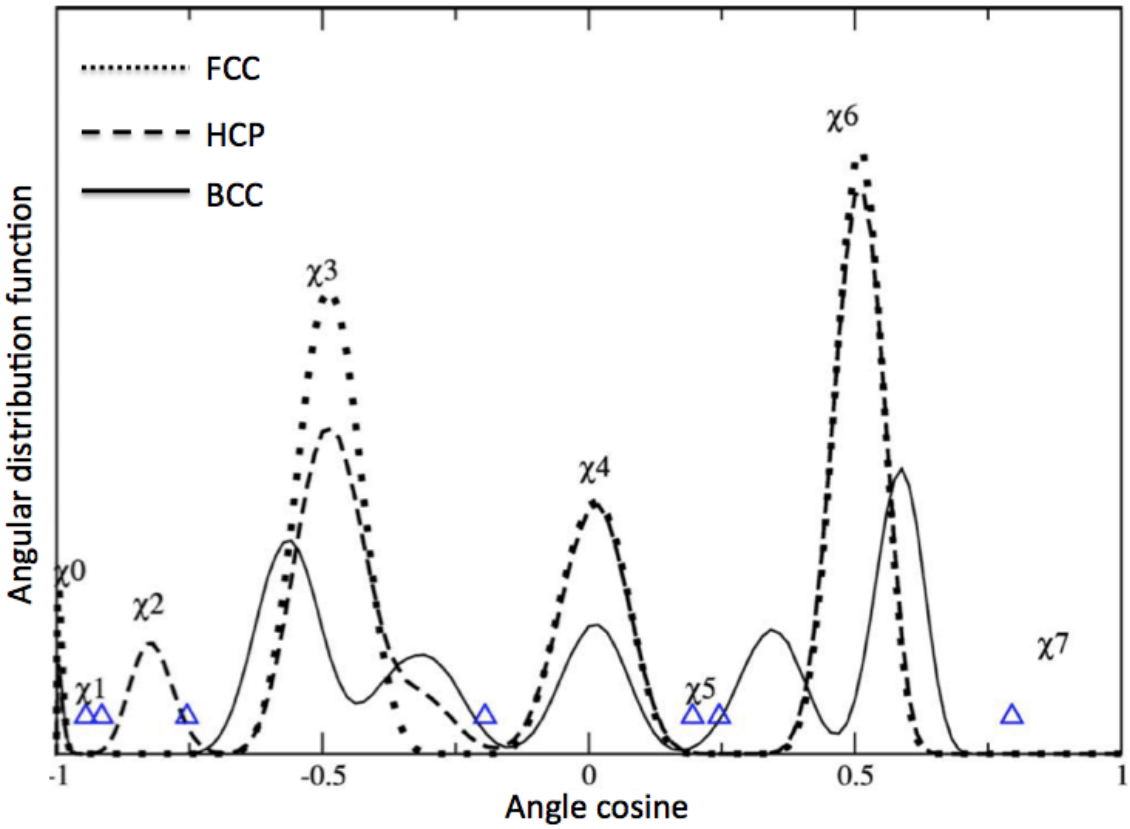

Figure 1.4: Representative angular distribution functions of FCC, HCP and BCC structure[69].

The typical procedure starts by evaluating the mean square separation distance r_0 of the particle i for its nearest six particles, which is given by:

$$r_0^2 = \sum_{j=1}^{6} \frac{r_{ij}^2}{6} \qquad 1.37$$

The number (N_0) of neighbors of the particle i and the bond angle cosines (θ_{ijk}) between all the neighbors of particle i can be evaluated with the condition of $r_{ij}^2 <$

$1.45r_0^2$. From the bond angle cosine value (θ_{ijk}), the X_i is determined. For example, if X_0 is 7, the particle is BCC; if X_0 is 6, the particle is FCC; if X_0 is 3, the particle is HCP. Any particle with the value of N_0 smaller than 11 will be assigned as an unknown particle.

1.3.8 Local atomic strain analysis

Shimizu et al. [71] developed the Least-Square Atomic Strain method, which is widely used in the process of atomic strain analysis. Two atomistic configurations, the reference and the current, are needed to calculate the local atomic strain, since strain is defined as a relative measurement. An integer, N_i, is defined as the number of neighbors of atom, I, in the present configuration. For each neighbor, j, of atom, i, their present separation is:

$$\boldsymbol{d}_{ji} = \boldsymbol{X}_j - \boldsymbol{X}_i \tag{1.38}$$

Their old separation was:

$$\boldsymbol{d}_{ji}^0 = \boldsymbol{X}_j^0 - \boldsymbol{X}_i^0 \tag{1.39}$$

A transformation matrix, $\boldsymbol{J}_i$, is desired to best map:

$$\{\boldsymbol{d}_{ij}^0\} \rightarrow \{\boldsymbol{d}_{ij}\} \quad \forall j \in N_i \tag{1.40}$$

By minimizing [72]:

$$\sum_{j \in N_j^0} \left| \boldsymbol{d}_{ji}^0 \boldsymbol{J}_i - \boldsymbol{d}_{ji} \right|^2 \tag{1.41}$$

The transformation matrix, $\boldsymbol{J}_i$, can be determined as:

$$\boldsymbol{J}_i = \left(\sum_{j \in N_j^0} \boldsymbol{d}_{ji}^{0T} \boldsymbol{d}_{ji}^0 \right)^{-1} \left(\sum_{j \in N_j^0} \boldsymbol{d}_{ji}^{0T} \boldsymbol{d}_{ji} \right) \tag{1.42}$$

For each $\boldsymbol{J}_i$, the local Lagrangian strain matrix is computed as:

$$\boldsymbol{\eta}_i = \frac{\boldsymbol{J}_i \boldsymbol{J}_i^T - \boldsymbol{I}}{2} \quad 1.43$$

The local shear invariant of atom, *I*, is:

$$\eta_i^{Mises} = \sqrt{\eta_{yz}^2 + \eta_{xz}^2 + \eta_{xy}^2 + \frac{\left(\eta_{yy} - \eta_{zz}\right)^2 - (\eta_{xx} - \eta_{zz})^2 - \left(\eta_{yy} - \eta_{xx}\right)^2}{6}} \quad 1.44$$

Based on the magnitude of the local von Mises strain, a coloring scheme is assigned to the simulated model, which can visualize the lattice slip in the crystals.

Chapter 2 : Revealing mechanical properties of Cu pillars using Micro-compression test

2.1 Literature review

Micro-compression test technique [30][31] is evolved from the Nano-indentation technique, and has been used heavily to test the mechanical properties of different metal pillars [33], [35], [37]–[39], [73]–[79], demonstrating its success in the determination on the mechanical characterization of metals.

2.1.1 Micro-compression test on gold pillars

This experiment was carried out by Greer et al. [80] in 2006 to reveal the deformation behavior of gold pillars. Gold pillars ranging in diameter between 200 nm and several micrometers were fabricated using focused ion beam (FIB) machining and lithography-electroplating technique. The former fabrication technique utilizes FIB machining [30] to etch patterns of interest into single crystal gold. In order to reduce the possible effect of Ga^+ ion implantation during the machining process, the lithography-electroplating technique was adapted by depositing gold to form the gold pillars [33]. Uniaxial micro-compression tests were conducted, with a flat punch diamond tip, on pillars of varying sizes and aspect ratios. The loading mechanism in this study was displacement-rate controlled rather than load-controlled. This method was designed to simulate a constant displacement rate, and therefore a nearly constant strain rate. Load-displacement data were collected in the continuous stiffness measurement (CSM) mode. The load-

displacement data obtained during the compression process were converted to uniaxial stress and strain using the assumption that the plastic volume was conserved throughout the deformation.

Results have shown a strength increase with a reduced diameter of the gold pillars. The concept of dislocation starvation was raised to explain this size effect. In ordinary plasticity, dislocation motion leads to dislocation multiplication by double cross-slip, invariably leading to softening before strain hardening occurs through elastic interaction of dislocation. In sub-micron crystals, dislocation can only travel very small distances before annihilate at free surface, reducing the overall dislocation multiplication rate. The overall dislocation density decreased with the more dislocation leaving the crystals than their multiplication. Such process would lead to a dislocation-starved state requiring very high stress to nucleate new dislocations. This dislocation starvation theory corresponded well to their experimental observation data of the evolving of the dislocation density during the deformation.

2.1.2 Micro-compression test on single crystalline copper pillars

Single crystalline copper pillars were fabricated by electroplating Cu into array of electron beam patterned holes in a PMMA matrix by Jennings et al. [75]. Uniaxial compression test was performed on these [1 1 1] oriented, FIB-less Cu pillars with diameters between 100 and 500 nm. Pillars smaller than 250 nm were compressed in SEMentor, a custom-built in situ mechanical deformation instrument [77]. All compression tests were carried out at nominally constant displacement

rate of 2 nm/s with simultaneous stiffness measurement option and the load-displacement data were converted to the stress-strain relationship.

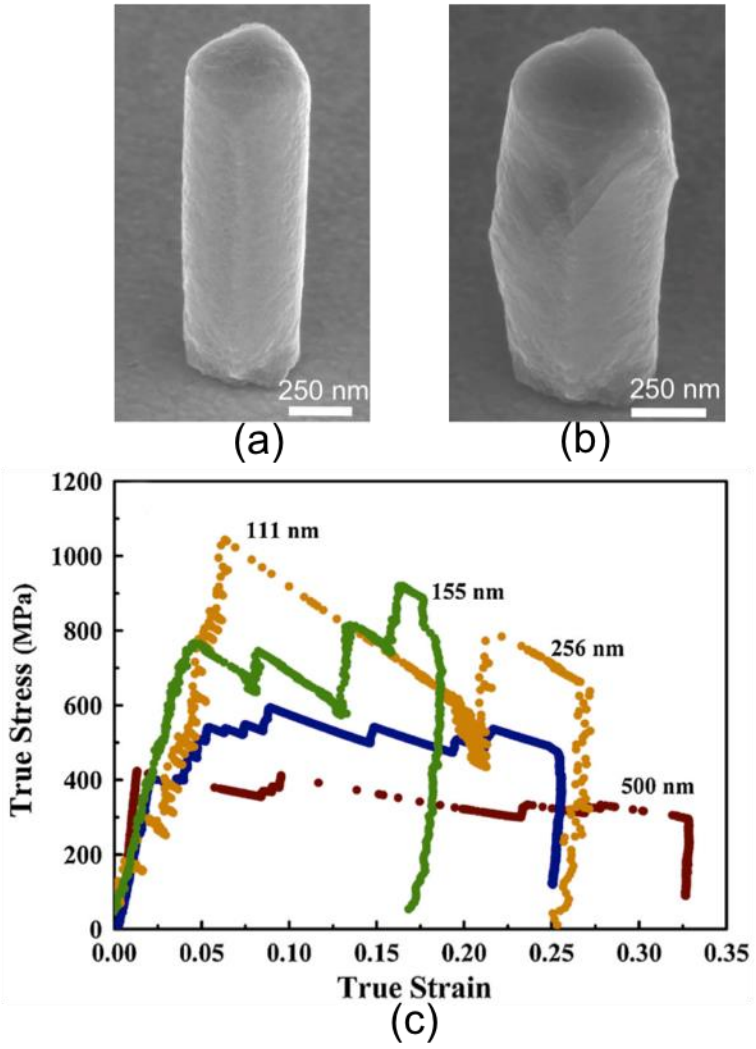

Figure 2.1: Representative SEM images of 500 nm diameter electroplated copper pillar (a) before compression (b) after compression. (c) Representative true stress – strain curves (the number above each curve corresponds to pillar diameter [75].

A typical as-fabricated Cu pillar is shown in figure 2.1 (a) and some surface roughness as well as the slightly imperfect pillar substrate can be observed. Figure 2.1 (b) shows the same pillar after compression. Representative true stress-strain curves corresponding to the deformation of pillars of four different diameters are

displayed in figure 2.1 (c). Initially, all the four runs underwent an elastic loading, and then followed by an intermitted, discrete strain bursts. At the end of each strain burst, the pillar had a short, nearly elastic loading until the stress was large enough to induce a new strain burst. Their results also gave a distinguished size effect: smaller pillars attained higher stresses compared with larger ones. Their finding convincingly showed that plasticity at sub micron scale was truly a function of microstructure, which in turn defined size effect. At small scales, no size effect can be achieved, which means the material can yield and deform at near theoretical strengths, if the structure is initially pristine without any dislocation. However, at nano-scale, crystals with nonzero initial dislocation density displayed remarkable dependence on size.

2.1.3 Micro-compression test on nano-crystalline nickel pillars

Schuster et al. [76] developed a two-step fabrication method to produce the micro-sized compression specimens with minimum use of focused ion beam. This process applied use of micro-electro-discharge-machining (micro-EDM) combined with polycrystalline diamond grinding (PCD) and was capable of producing multiple compressive specimens that were well aligned, have relatively uniform dimension [81]. Micro-EDM was originally developed to drill micrometer-sized holes in inkjet nozzles. This noncontact form of machining relied on pulsating for material removal. They made several improvements to adapt a three-axis stage to allow for a three-dimensional milling. The nominal dimensions of the finished pillars are 20 micrometers on a side with a square cross-sectional geometry and a respect ration

of 2 (figure 2.2 (b)). The single pillar was in the array of 4 × 5, as shown in figure 2.2 (a).

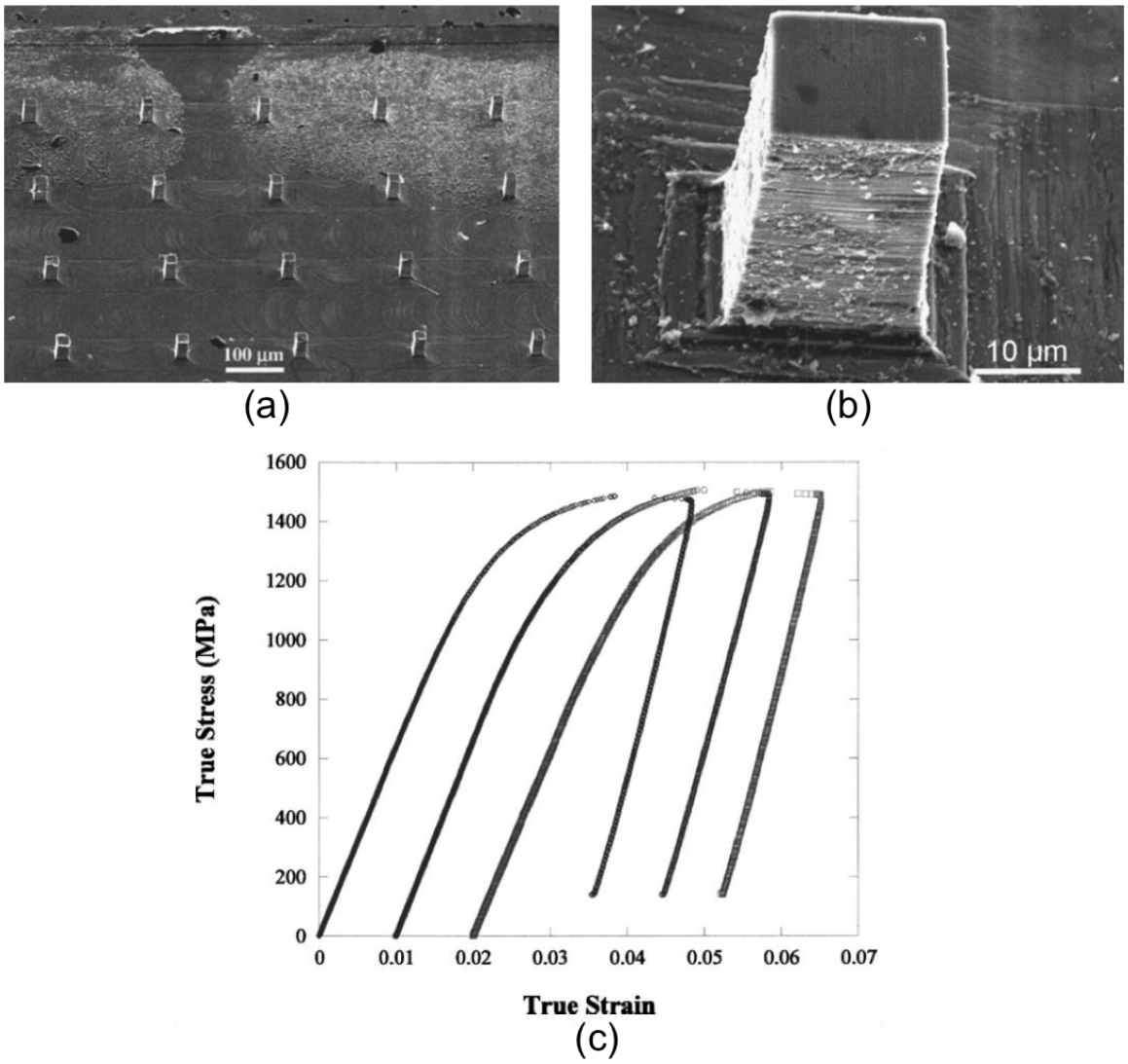

Figure 2.2 (a) SEM image of array of the nano-crystalline nickel from micron EDM followed by PCD grinding. (b) SEM images of a single pillar with a nominal dimension of 20 micrometers and aspect ration of 2. (c) Repeatable compressive response of nano-crystalline nickel pillars with constant yield strength and peak strength. [76]

Micro-compression test was carried out on the nano-crystalline nickel pillars using an MTS Nanoindenter XP with continuous stiffness measurement (CSM) extension. The load and displacement along with the corresponding stiffness were

recorded for these specimens deformed at a strain rate of 10^{-3} s^{-1}. Figure 2.2 (c) shows the resulting stress-strain curve. The compressive yield strength at 2% offset was 1210 +/- 20 MPa. The maximum strength was repeatable for each case and was 1498 +/- 10 MPa. Structure failure or buckling could be observed at some specimen with less than 10% strain. Local material variation was blamed to trigger such failures. Compared with tensile test done by Wang et al. [82] on the same batch of the material, a compression-tension asymmetry of 1.16 was reported. They adopted the models proposed by Lund et al. [83] and Cheng et al. [84] to explain this asymmetry phenomenon. They related the uniaxial strength of material to the self-energy of a dislocation under pressure and demonstrated a gradual increase in compression-tension asymmetry with decreasing grain size in their samples.

2.2 Experimental

2.2.1 Pattern generating

Copper pillars were fabricated using the electron beam lithography (EBL) and electroplating method [85], which were illustrated in figure 2.3 showing the schematic process steps. The silicon wafer was coated by electron beam evaporation with around 25 nm titanium layer followed by around 30 nm gold seed layer, as illustrated in figure 2.3 (a). Then the substrate was spin coated with poly (methyl methacrylate) (PMMA), and different thickness of the PMMA can be obtained using different spin speed, which could further determine the height of the pillars during the electroplating procedure. Vistec EBPG 5000+ Electron Beam system at the University of Toronto operating with 100 KV acceleration voltages was used to

generate the via-hole patterns. After the exposure, the PMMA was developed with a solution of methyl isobutyl ketone and isopropyl alcohol.

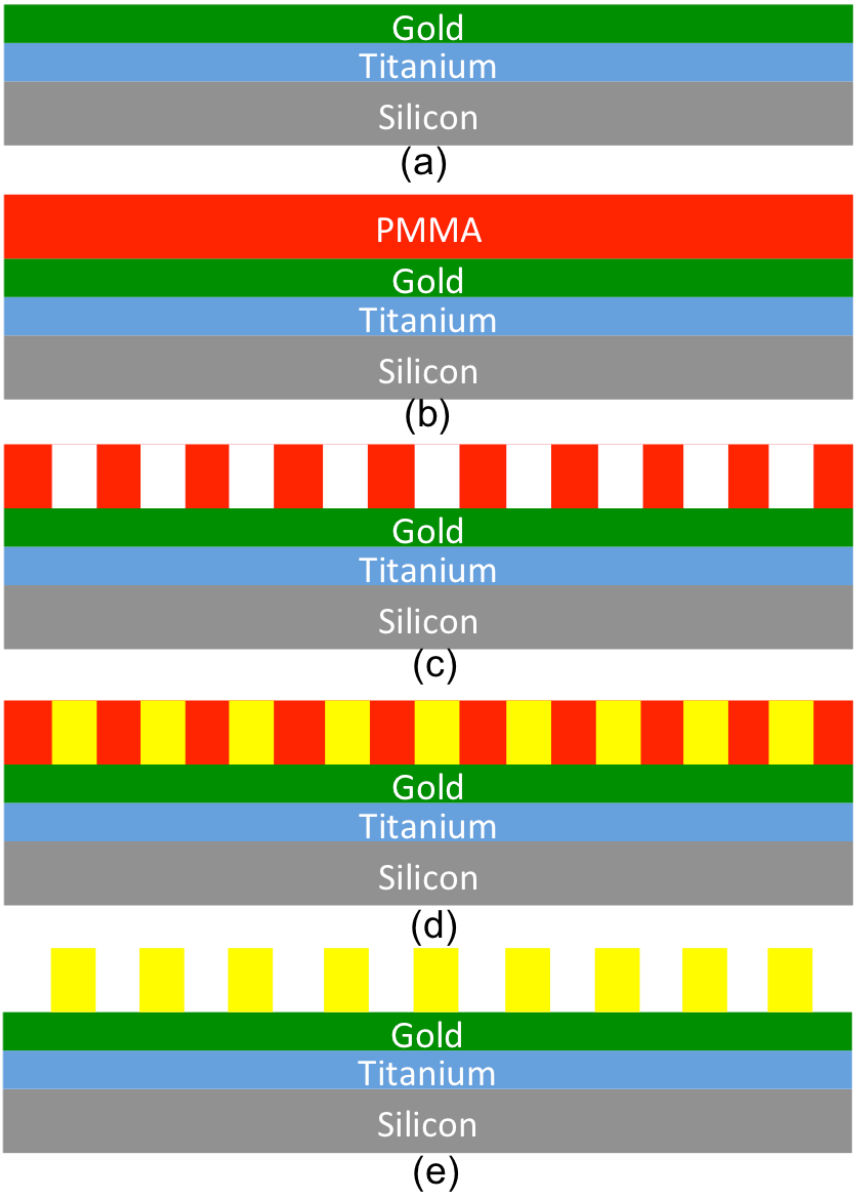

Figure 2.3 Schematic process of Electron Beam Lithography and Electroplating used to fabricate the copper pillars. (a) Deposition of titanium and gold. (b) Deposition of PMMA. (c) Electron Beam Lithography. (d) Deposition of copper. (e) Removal of PMMA.

2.2.2 Electroplating solution preparation

In order to fabricate pillars with different grain sizes, three different batches of electrolytes (summarized in table 1) based on Hakamada et al. [86] were prepared. All plating solutions consisted of copper (II) sulfate pentahydrate (220 g/L) and sulfuric acid (60 g/L). The batch A solution was intended for the large grain size specimen with no additives added. The medium and small grain size plating solutions were prepared by adding 0.01 g/L and 0.02 g/L Thiourea into the base solution respectively. All the chemicals used were purchased from Sigma Aldrich with purity of greater than 98%.

Table 2.1: Copper electroplating solution compositions.

Batch	$CuSO_4 .5H_2O$ (g/L)	H_2SO_4 (g/L)	Thiourea (g/L) CH_4N_2S	Target grain size
A	220	60	None	Large
B	220	60	0.01	Medium
C	220	60	0.02	Small

2.2.3 Electroplating

The prepared wafer was then diced into around 1 × 1 cm square chips with PMMA patterns template in the center, and the electroplating technique was used to deposit copper onto the chip. The prepared solution was stirred about 20 minutes at room temperature, prior to the plating, to ensure its homogeneity. A blanked gold coated chip almost same area as the PMMA patterned chip was chosen as the dummy chip. The dummy chip and the target chip mounted in separated clips acted as cathode, facing the copper metal sheet in the bath solution. Before mounting, the PMMA on one edge of the target chip should be scratched off to ensure its

conductivity. The deposition was carried out at ambient conditions with direct current density of 30 mA/cm^2 for small and medium grain size specimens, and 50 mA/cm^2 for large grain size specimen. The plating duration time for the small, medium and large grain size samples were 22 s, 28 s, and 10 s respectively. The post-plated chips were then kept in acetone for around 40 minutes to dissolve the remaining PMMA.

2.2.4 Uniaxial micro-compression

Uniaxial micro-compression tests on the copper pillars were carried out under an in situ nanoindenter (Nanomechanics Inc., Knoxville, Tennessee, USA) equipped with a custom-made diamond flat punch tip of a square cross-sectional dimension of 8×8 micrometers. Prior to starting compression, the sample was mounted on the sample holder and kept inside the Nanoindenter box for nearly 12 hours as to ensure the sample's mechanic and thermal stability. A small piece of indium was stuck on the sample surface for the microscope to indenter calibration. A prescribed deformation rate of 2 nm/s was selected, and the corresponding strain rate is around 0.002 s^{-1}. The nanoindenter drift rate was required to be less than 0.05 nm/s for all the pillars.

2.2.5 SEM characterization

All the pillars were characterized using field emission Scanning Electron Microscope (Zeiss LEO 1550) before and after deformation. Both flat and 70 degrees tilted stubs were used to mount the samples. The electron acceleration voltage was

set to be 10 KV with the system pressure less than 1.5×10^{-5} mbar. No gold coating is needed during the sample preparation.

2.3 Results and discussion

2.3.1 Copper pillar geometries

Representative titled and top-down SEM images of as-fabricated copper pillars with four different cross-sectional geometries, namely solid core, hollow, x-shaped, c-shaped are shown in Figure 2.4. The outer diameter of the solid core pillars for small, medium, and large grain are 564 +/- 7, 561 +/- 9, and 551 +/- 7 nm respectively. The wall thickness of hollow pillars for small, medium, and large grain are 166 +/- 10, 158 +/- 7, and 150 +/- 11 nm respectively. The wall thickness of the c-shaped pillar is larger than that of hollow pillars with 198 +/- 7, 205 +/- 9, and 187 +/- 9nm for small, medium, and large grain respectively. The pillars with different grain sizes share similar dimensions for each geometry. Top-down views of hollow and c-shaped pillars reveal their interior are clear and without residues during the fabrication process. With the careful inspection of SEM images for all the pillars, all pillars with different grain sizes have smooth sidewall surface, and the sidewall are nearly perfect vertical alignment with the substrate surface with the exception of noticeable tapering near the base of x-shaped structures. The SEM micrographs also reveals slightly off-centered placement of the cylindrical hole inside the hollow pillars.

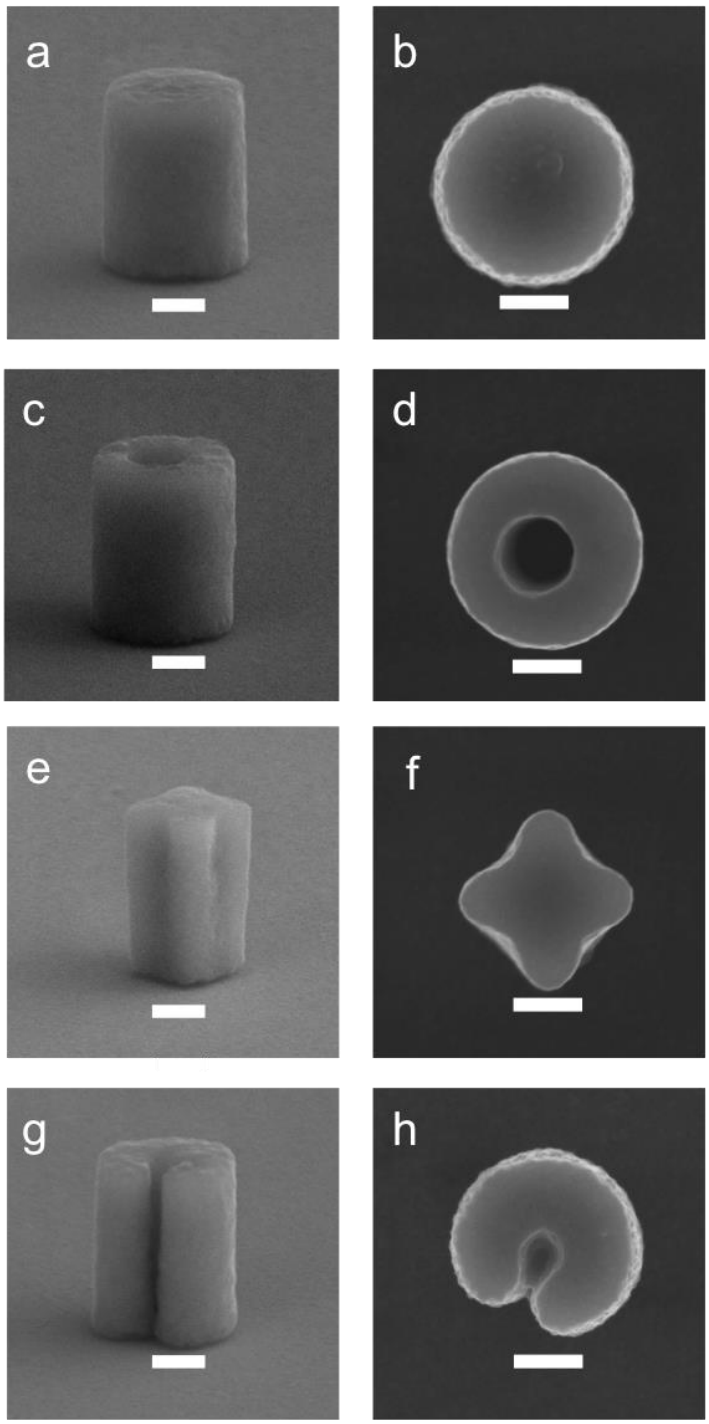

Figure 2.4: Representative tilted (70°) and top-down SEM images of as-fabricated sub-micron medium grain copper structures with different geometries. (a) Solid core pillar. (c) Hollow pillar. (e) X-shaped pillar. (g) C-shaped pillar. (scale bar representing 200 nm)

Copper pillars with small and medium grain possess a smooth top surface compared with the pillar of large grain size. As shown in Figure 2.5, the top surface of the large grain pillar is rough. Similar copper pillars with 1000 nm diameter have been fabricated with the exact same solution and procedure in our group before and the only difference is the dimension. As a result, we assume same grain size distribution can be achieved for large grain copper pillars. From the grain size measurement based on the high-resolution TEM images of the previous copper pillar, the grain size for the large-grain copper pillar can be around 50 nm. Therefore, one possible explanation can be that the rough top surface results from the packing of large grain in a relatively small space. The rough top surface could cause non-uniform stress distribution during the initial contact of the pillar and indenter tip. Herein, in the final stress-strain analysis of the large-grain pillar, only pillar with relatively smooth top surface was accounted.

In order to confirm the chemical composite of electroplated copper pillars, X-ray photoelectron spectroscopy (XPS) was used to analyze the blanked copper thin film that has underwent the same plating procedure as the copper pillar. XPS results reveal these copper films composed of the copper with less than 2 atomic % of oxygen that is believed to originate from the surface native oxide layer. Grazing-angle x-ray diffraction (GAXD) experiments were also performed on the copper blanked films and confirmed the crystalline nature of copper specimens. This chemical composites analysis result was also taken from the previous experiments in our group. As mentioned above, the electroplating solution and the electroplating

procedure are exactly the same and the same chemical composites can be anticipated for these two sets of samples.

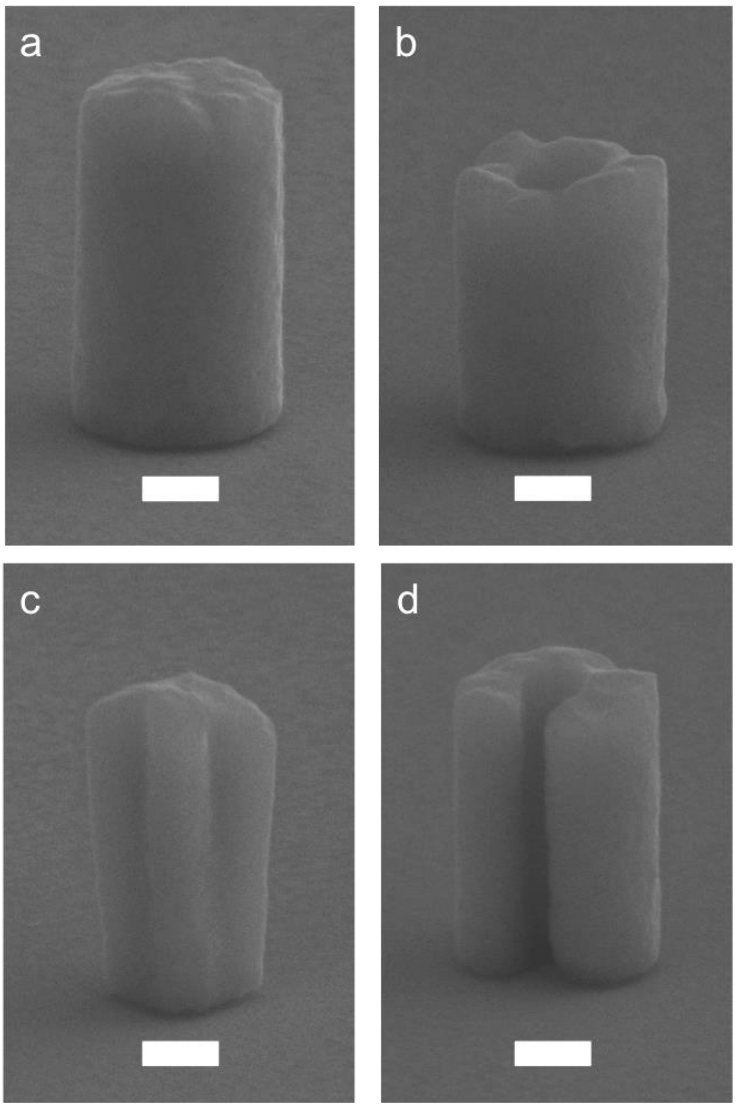

Figure 2.5 Representative titled (70°) SEM images of as-fabricated copper pillars with large grain size. (a) Solid core. (b) Hollow. (c) X-shaped. (d) C-shaped. (scale bar representing 200 nm)

2.3.2 Post compression analysis

All the compressed columnar structures were inspected using high-resolution SEM. Some pillars exhibited buckling, tilting, or bending, of which the data were discarded from the stress-strain analysis. During the compression

process, some pillars underwent catastrophic failure, exhibiting knocking down, partial compression and collapsing. Tsui et al. [79] carried out micro-compression tests on rhodium pillars with complex geometries. 36% plastic strain was achieved in hollow rhodium pillar. They observed buckling on this hollow rhodium pillar, however, there is no formation of crack on the specimen's sidewall.

Figure 6 shows typical post deformation SEM images of medium-grain copper pillars. The top surface becomes smoother after being compressed. These pillars maintain the same cross-sectional geometries throughout the compression process, which is a strong indication that compressive stress incurred during the deformation was uniformly distributed through specimens, and no stress concentration took place during the compression process. No obvious crack can be observed along the sidewalls of the pillars. For the large-grain copper pillars, there are some cracks on their top surface. As shown in figure 2.5, the top surface of the large-grain pillar is very rough and if the displacement is not enough, the top surface is still rough even after compression. The top surface crack can also be observed on some pillars with small and medium grain. Since the top surface of the small and medium grain pillar is relatively smoother than large-grain pillars, I assume the crack results from the grains separating from each other along the grain boundaries. This post compression feature demonstrates that the copper pillar deformation is assisted by grain boundary sheering.

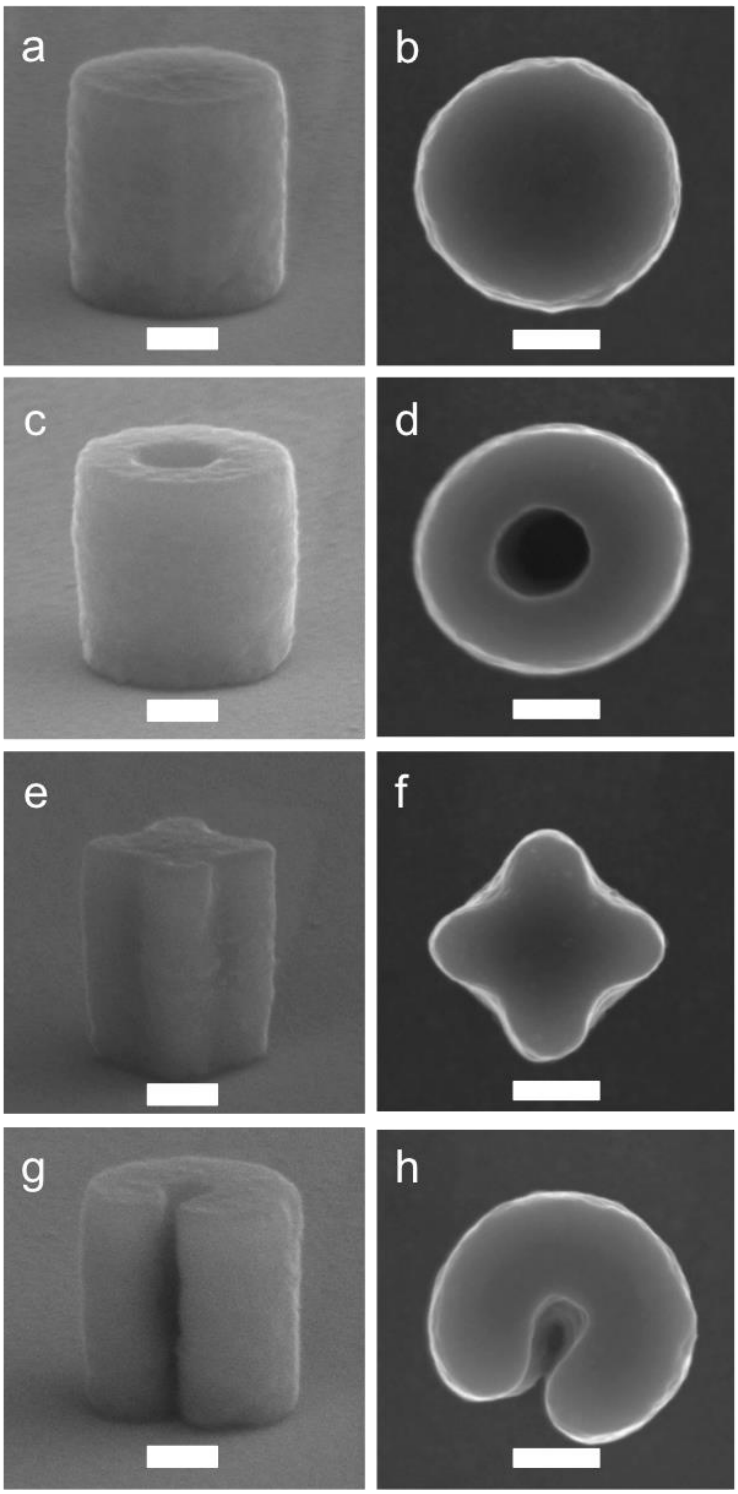

Figure 2.6 Representative tilted and top-down SEM images of compressed medium-grain copper pillars with four different geometries. (a) Solid core. (c) Hollow. (e) X-shaped (g) C-shaped. (scale bar representing 200 nm)

2.3.3 Load-displacement behavior

Typical load-displacement curves of copper pillars with solid core, hollow, x-shaped and c-shaped cross-sectional geometries are shown in Figure 2.7. Each of these figures consists of the results from samples with small, medium and large grain. As displayed in figure 2.7, the curves for the small and medium grain are smooth and without any discontinuities, which is expected for polycrystalline copper. However, the curves for the large grain sample show serrated curves, and this is caused by the relatively rough top surface of the pillar structures. Each curve consists of elastic deformation part, plastic deformation part and unloading part. The load increases steeply with the displacement at the elastic region, while at the plastic deformation region, the load increases slightly with the ongoing displacement because of the steady enlargement of cross-sectional area during the deformation. The load decreases dramatically when the unloading takes place.

Figure 2.7 (a) – (d) reveal all of the large specimens with four different cross-sectional geometries bear smaller load than those with medium-grain specimens. This trend is corresponding to the Hall-Petch effect with sample of smaller grain size maintaining a stronger strength. Interestingly, an opposite effect is observed when comparing the results between the small-grain and medium-grain specimens. The small-grain pillars deform at slightly lower loads tan the pillars with medium grains, and the inversed Hall-Petch effect must occur at these grain size regions.

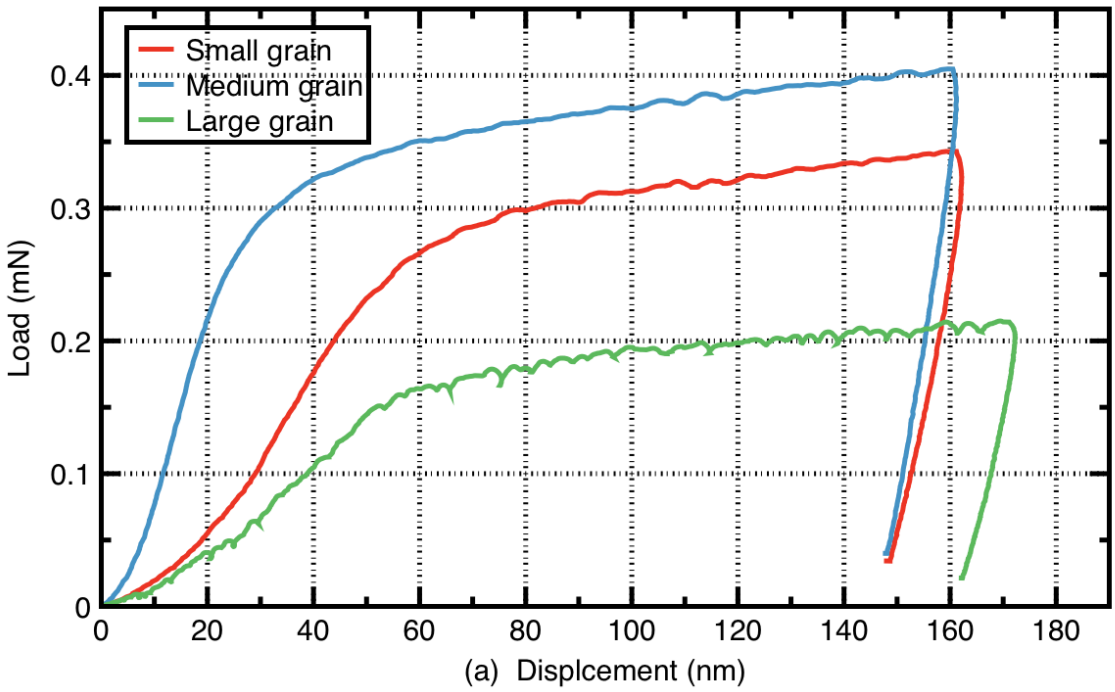
Small grain
Medium grain
Large grain
Load (mN)
0
0.1
0.2
0.3
0.4
0
20
40
60
80
100
120
140
160
180
(a) Displcement (nm)

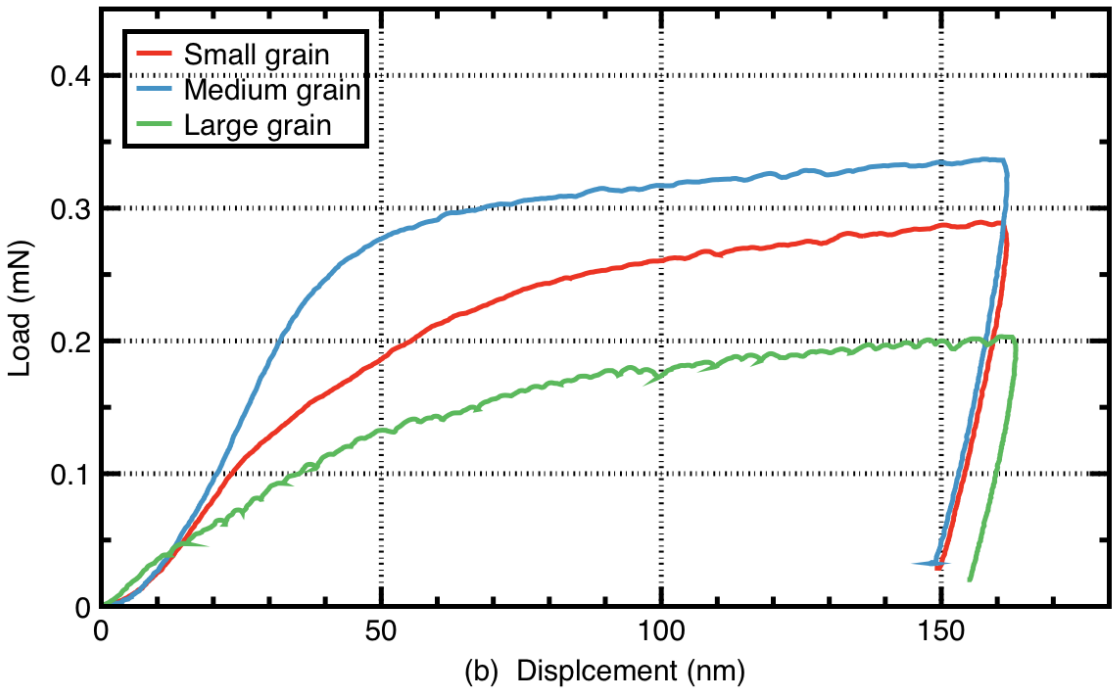
Small grain
Medium grain
Large grain
Load (mN)
0
0.1
0.2
0.3
0.4
0
50
100
150
(b) Displcement (nm)

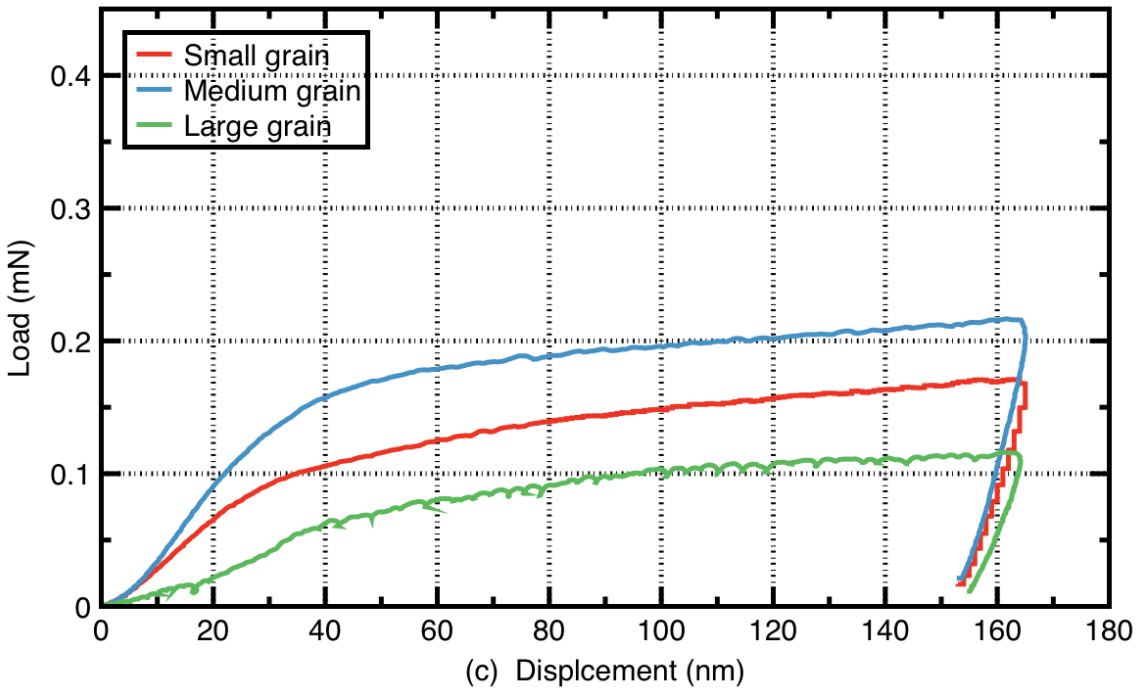

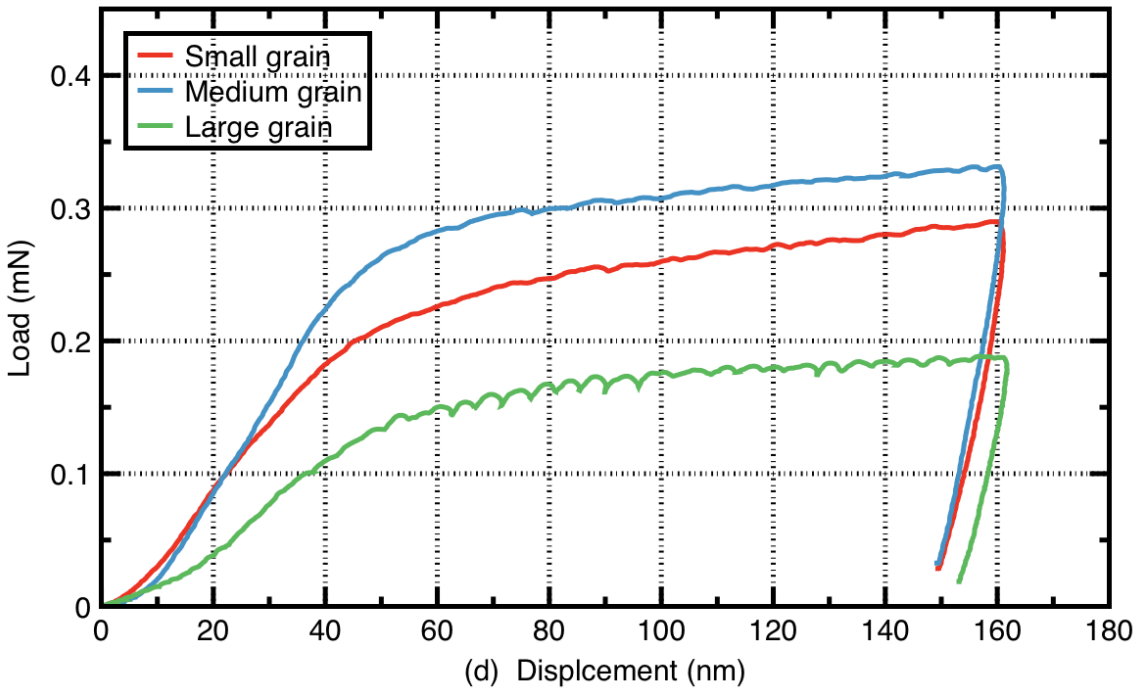

Figure 2.7: Representative load-displacement curves collected during uniaxial compression of copper pillars with four different cross-sectional geometries. (a) Solid core. (b) Hollow (c) X-shaped (d) C-shaped.

Cyclic compressive deformation has also been carried out on the solid core pillar with small, medium and large grain size. The whole deformation process was divided into 5 cycles and each cycle was set to deform the equal length. Typical load-displacement curves of small, medium, and large grain pillars are displayed in Figure 2.8, where each curve is corresponding to one cycle. In Figure 2.8 (a), the nominal displacement of each cycle was set to be 45 nm, and the nominal total displacement of 225 nm can be achieved after 5 cycles. However, discrepancy was found when comparing this displacement data from the curves with that from the measurement. The pre- and post- deformation heights of pillar were measured through the SEM images, and the true displacement was around half of the nominal displacement. Generally, these cyclic load-displacement curves are similar to the regular curves with load of each cycle is higher than its previous deformation, which can be explained by the change of the cross-sectional area during each deformation.

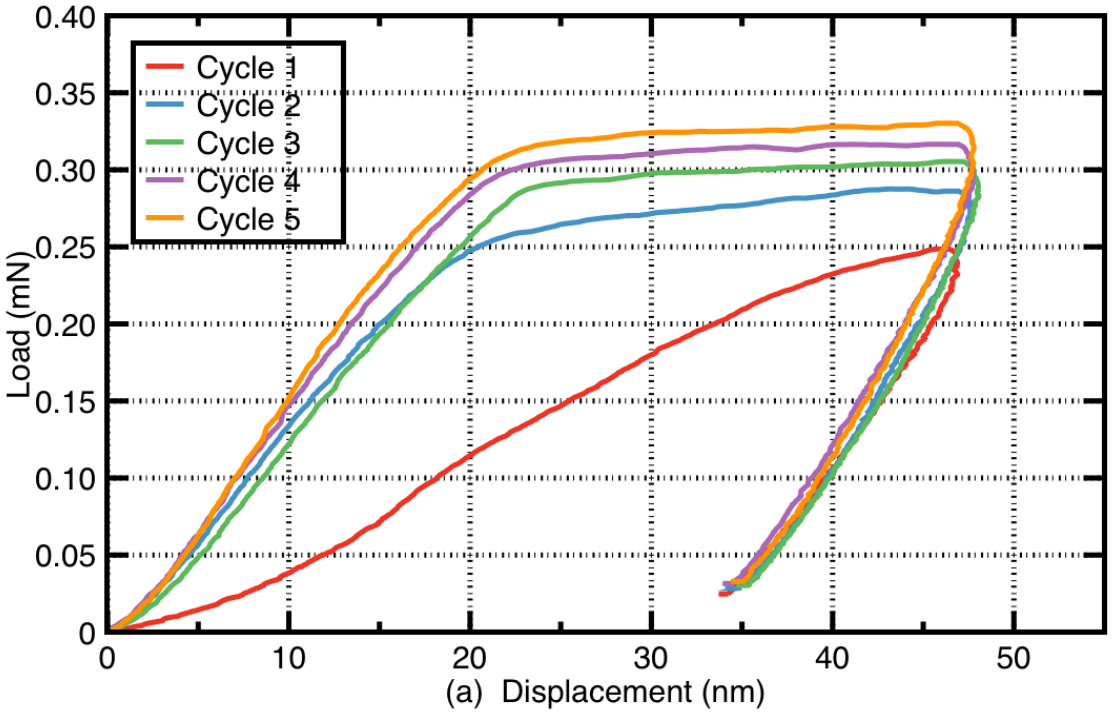

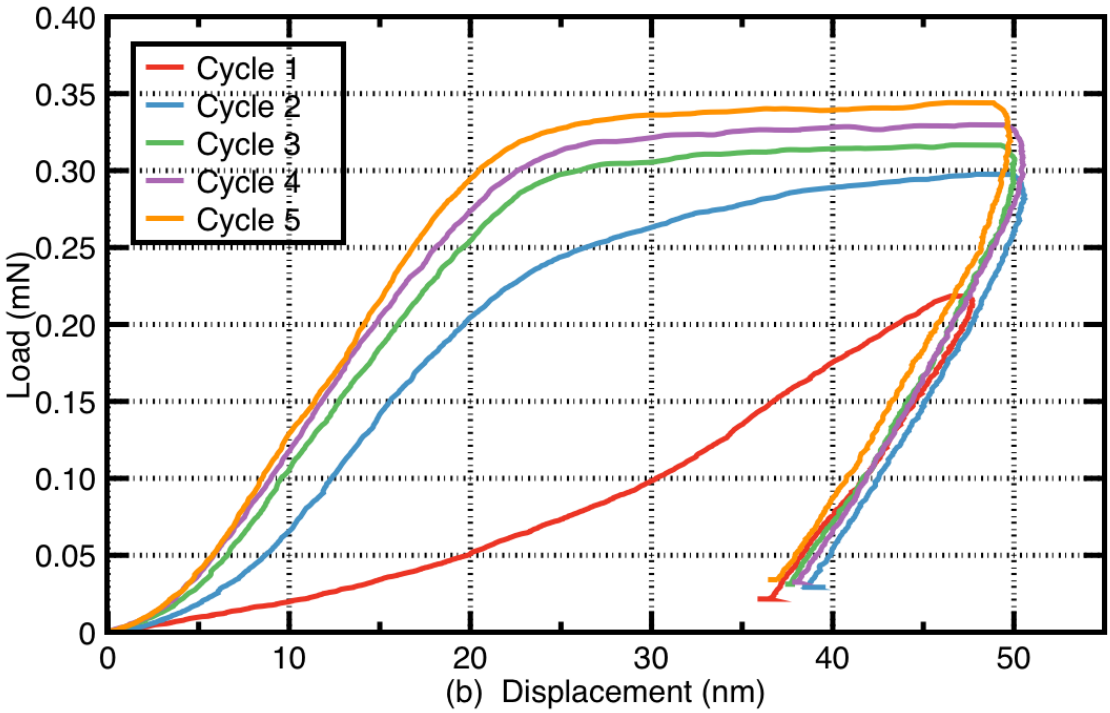

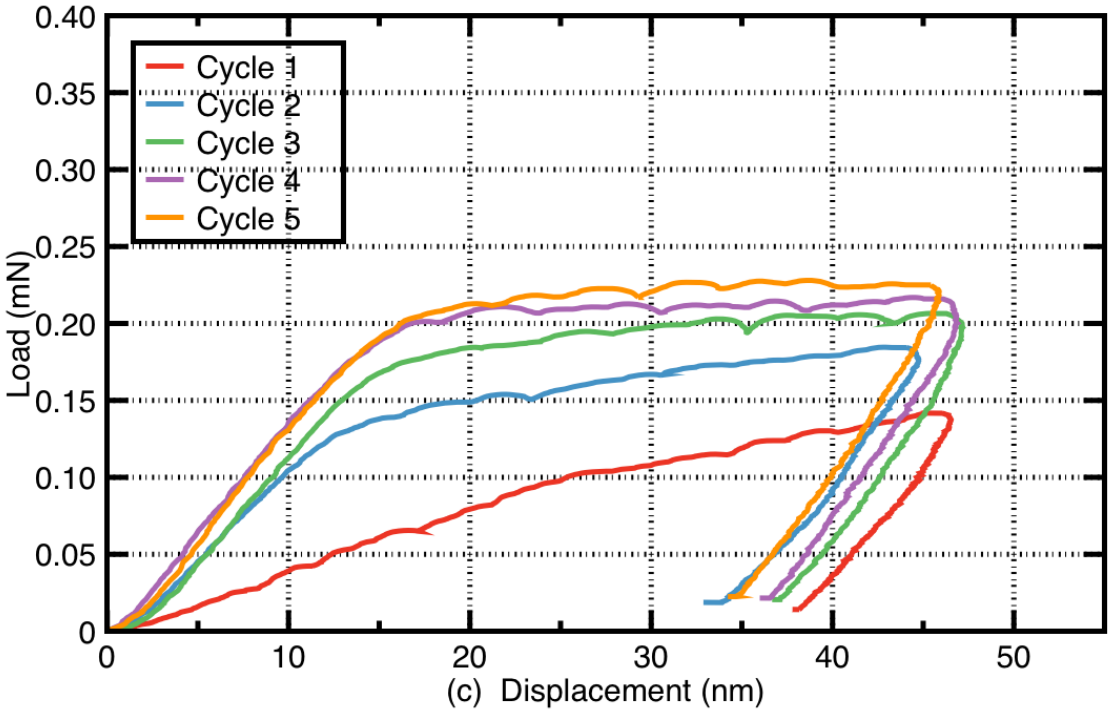

Figure 2.8 Representative load-displacement curves of solid core copper pillars with different grain sizes. (a) Small grain. (b) Medium grain. (c) Large grain.

2.3.4 Stress-strain behavior

To understand the mechanical behaviors of these pillars, true flow stress and plastic strain of the copper pillars were calculated. According to Greer's method [33], the load-displacement curve can be converted to stress-strain curve directly by assuming the plastic volume of pillar structures conserved during the deformation and no substrate contributions. Since our copper pillars were deposited on silicon substrates coated with two thin film layers, the displacement generated from the compression tests contained both elastic and plastic deformation from the compliant materials and the copper pillars. In order to eliminate the mechanical effects from the films and substrates, the raw load-displacement curves were not used to convert to stress-strain curves directly. Instead, the true stress and strain relationship was calculated on the data generated from the indenter and SEM images. Plastic flow stress was defined as the ratio between maximum loads applied on the pillar and the top-down cross-sectional area of the post-deformation copper pillars. The measurement error is within 1%. The maximum load was acquired directly from the data generated from the indenter, and the actual area of the post compression pillar was accurately measured from the top-down SEM images as shown in figure 2.6 (b)(d)(f)(h). The resolution of nano-indenter is around 50 nN, which is less than 0.1% difference error. This flow stress measurement approach provides a highly accurate method to determine the true plastic stress experienced by the copper pillars since both the maximum load and the contact area are measured directly, independently and verifiable without the need of any theoretical assumption or modeling. The plastic strain was simply calculated at the ratio

between the final and initial heights, and both of these heights were obtained by measuring the 70 degrees titled SEM image both before and after deformation.

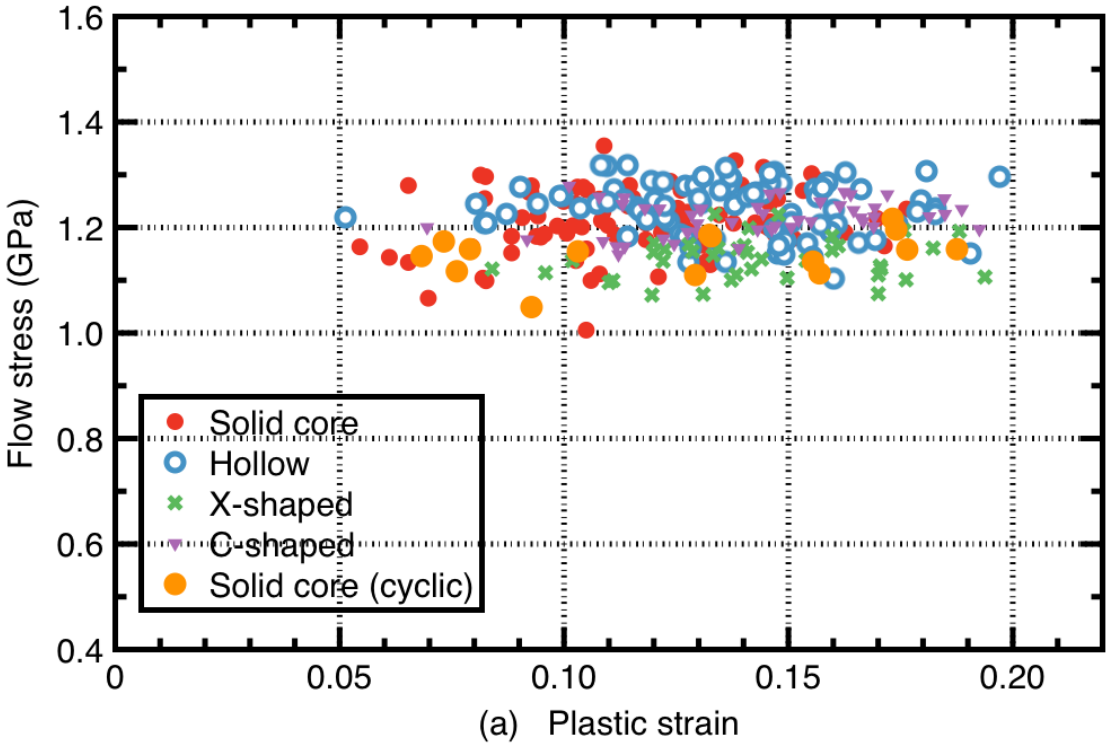

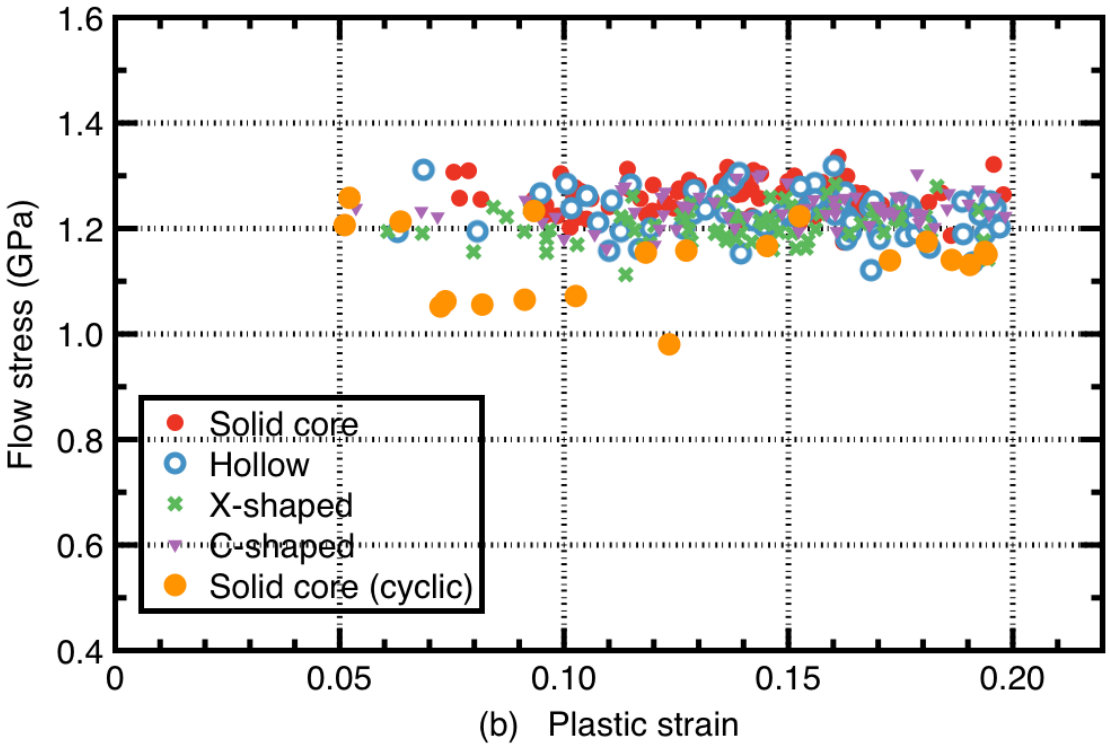

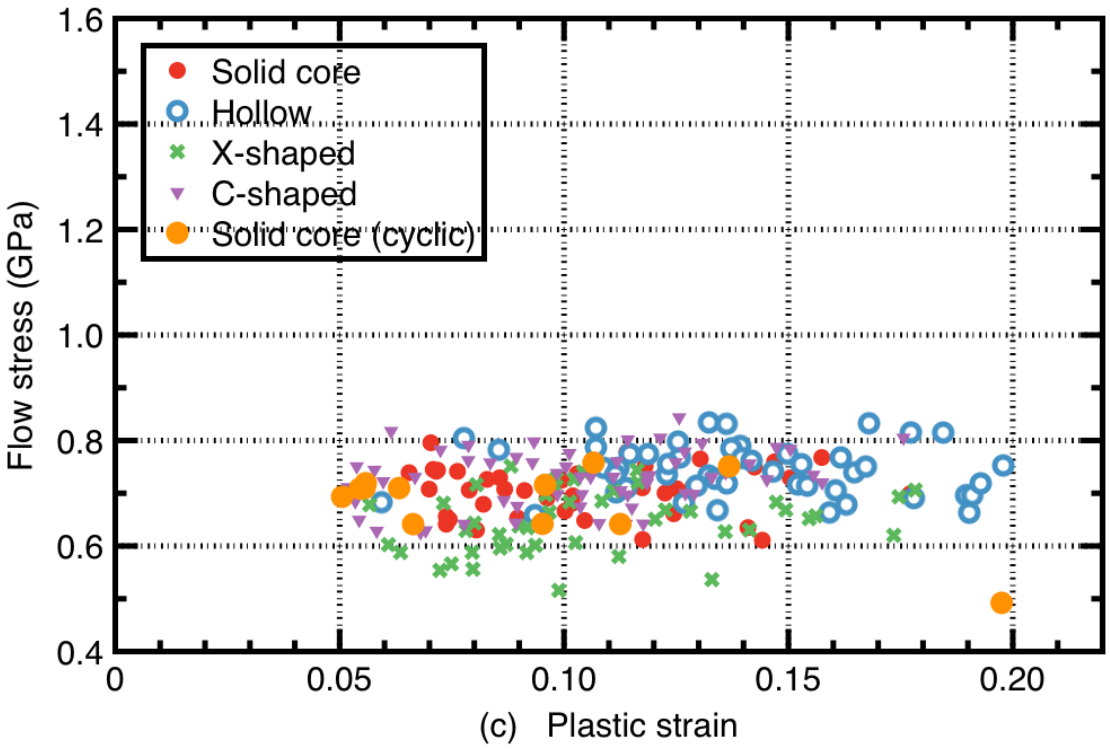

Figure 2.9: Flow stress of copper pillars with four different cross-sectional geometries and grain sizes. (a) Small grain. (b) Medium grain. (c) Large grain.

True flow stresses of the copper pillars with small, medium, and large grains are plotted as a function of plastic strains in Figure 2.9. Each figure shows data collected from pillars with different grain sizes, and each data point shown in Figure 2.9 represents the result of one single compression test on the copper pillar. Only results lying within the plastic strain range of 5% to 20% were selected in these figures. Results collected from larger deformation (> 20% strain) were not included in these figures due to greater tendency for the pillars to buckle. The average flow stress of each specimen is shown in Figure 2.10 with the error bar representing one standard deviation. As displayed in Figure 2.9, regardless of the different cross-sectional geometries of the copper pillars, they all exhibit nearly perfect plastic

deformation. Farrokh et al. [87] has also observed similar stress-strain response in nano-crystalline copper. Additionally, plastic deformation behavior has also been observed under cyclic deformation for all the grain size regimes.

Figure 2.9 (c) shows flow stress-strain relationship for the copper pillar with large grain, and each data point refers to the result of compression test of the single pillar. The average stress of the large-grain copper pillars with cross-sectional geometries of solid core, hollow, x-shaped and c-shaped are 0.71 +/- 0.05, 0.75 +/- 0.05, 0.65 +/- 0.06, and 0.72 +/- 0.05 GPa respectively (Data spreads indicate one standard deviation). Furthermore, no statistically distinguishable mechanical strengths among the pillars with four different cross-sectional geometries have been observed from figure 2.9 (c). It is interesting to notice that copper pillars with different cross-sectional geometries have different surface ratio, and this indistinguishable mechanical behavior shows the evidence of no surface ratio effect on the mechanical properties of the large-grain copper pillars. The results of the solid core copper pillar with large grain under cyclic deformation are also plotted in figure 2.9 (c), of which the average stress is 0.68 +/- 0.06 GPa. This value is almost the same as the average flow stress of solid core copper pillar under regular deformation mode.

The stress-strain behavior of medium-grain copper pillars is displayed in Figure 2.9 (b). Results show the copper pillars with four different cross-sectional geometries of solid core, hollow, x-shaped, and c-shaped have the average flow stress of 1.26 +/- 0.03, 1.23 +/- 0.04, 1.21 +/- 0.03, and 1.23 +/- 0.03 GPa. Similar to the large grain-size copper pillars, there is no shape-related mechanical difference

existing among the medium-grain pillars with various cross-sectional geometries. The medium-grain copper pillars show a 70% stronger than the large-grain copper pillars shown in figure 2.9 (c), which is corresponding to the Hall-Petch effect. The medium-grain pillar with cross-sectional geometry of solid core shows a 10% decrease of mechanical strength under cyclic compression.

Mechanical strengths of small-grain copper pillars are plotted in Figure 2.9 (a). The average flow stresses of the specimens with cross-sectional geometries of solid core, hollow, x-shaped, and c-shaped are 1.21 +/- 0.06, 1.24 +/- 0.05, 1.14 +/- 0.04, and 1.21 +/- 0.03 GPa respectively. Except for the x-shaped pillar with a slightly lower strength, the others exhibit no shape dependency of mechanical strength. Moreover, compared with the medium-grain specimen, the strength of the small-grain pillar was reduced slightly when the grain size becomes smaller, which does not correspond to Hall-Petch effect. The small-grain copper pillar with solid core cross-sectional geometry also shows a slightly reduced strength of 1.15 +/- 0.05 GPa under cyclic compressive deformation.

Guduru et al. [88] has conducted tensile test on the nano-crystalline copper structures with the average grain size of 74 nm that is comparable to the grain size of the large-grain pillars. Their results showed the strain rate sensitivity with higher strain rate corresponding to higher strength. At the strain rate of 2.5×10^{-3} s^{-1}, which is similar to what used in our pillar compression, the true flow stress can reach to 0.78 GPa. This result is identical to the flow stress of the large-grain pillars in our experiments. Chen et al. [89] carried out hardness test using nano-

indentation. Dividing the hardness value by 3 to get the yield stress, their results still followed the Hall-Petch effect even for the grain size down to 10 nm.

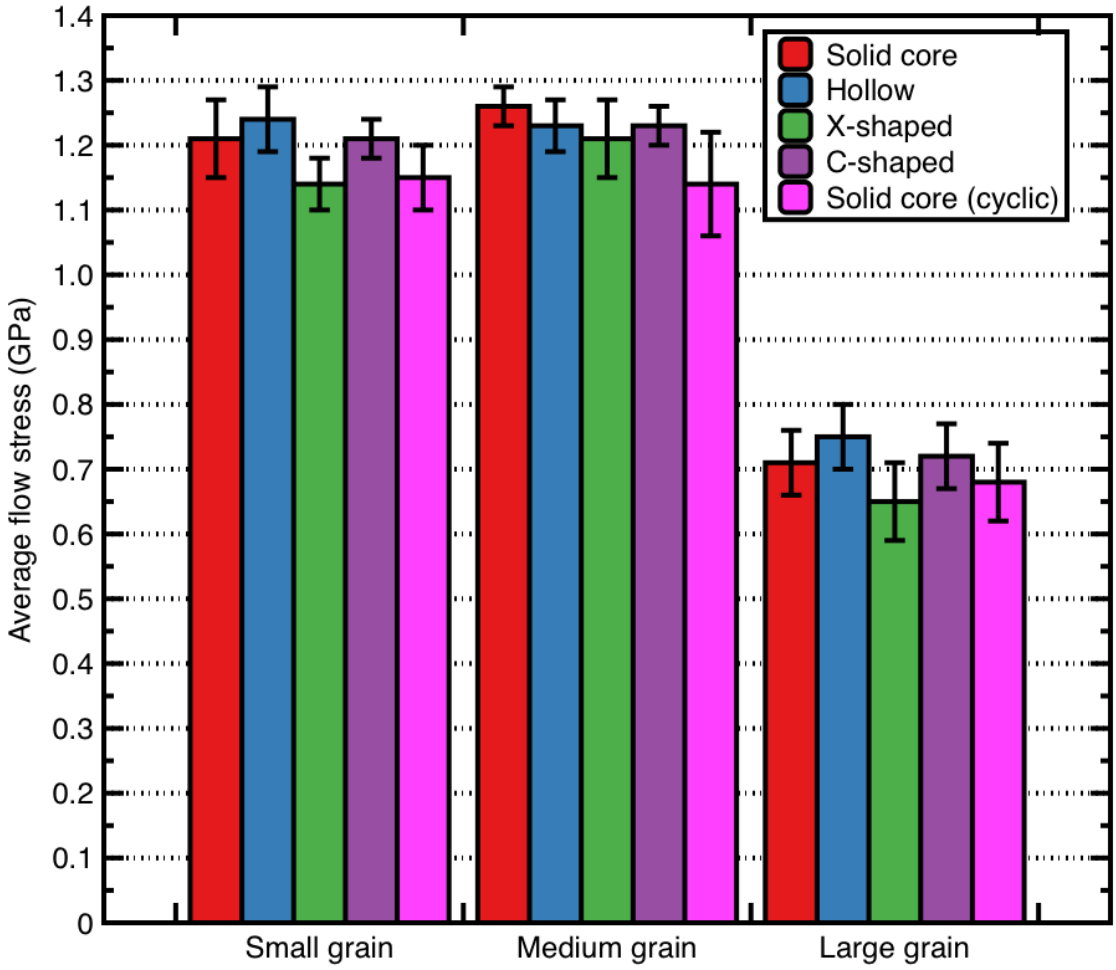

Figure 2.10: Average flow stress of copper pillars with various cross-sectional geometries. (Error bar stands for one standard deviation)

The average stresses of each shape with different grain sizes are summarized in Figure 2.10. Taking the standard deviation into account, these copper pillars have flow stresses statistically indistinguishable from each other for the same grain size specimens. This shape-independent phenomenon has been observed by Tsui et al. in columnar structures of nickel [37], rhodium [79], rhenium-nickel alloy [78], and

cobalt [36]. These series of experiments have provides a strong evidence of no geometries effects on the mechanical properties of the metals.

Based on the previous high-resolution TEM image measurement, the average sizes of small, medium and large grain in solid core copper pillars are 4.4, 24.5, and 37.4 nm respectively. The mechanical strengths of nano-crystalline specimens increased considerably when their grain size reduced. For the medium grain size samples, the true flow stresses of the solid core specimens increased from 0.71 +/- 0.05 GPa (Large grain size of 37.4 nm) to 1.26 +/-0.03 GPa (Medium grain size of 24.5nm). This strength enhancement is corresponding to classical Hall-Petch effect, which is caused by grain boundary strengthening mechanism. In contrast to the strengthening at the large grain to medium grain regime, no further mechanical strength enhancement can be observed from medium grain size to small grain size. The lack of strength enhancement with reduction of grain size suggests the termination of the grain boundary strengthening mechanisms. This is an indication of deformation mechanism transition from classical Hall-Petch to inversed Hall-Pecth relationship. For the solid core copper pillars, the average flow stresses for medium and small grain are 1.26 +/- 0.03 and 1.21 +/-0.06 GPa respectively, which represents a slight decrease. This medium grain to small grain regime indicates that the critical grain size threshold for transition between classical and reverse Hall-Petch relationships of copper pillars is within the rage of 4.4 nm and 24.5 nm. This threshold size regime is consistent with the bulk nano-crystalline copper, where the threshold is in the range of 10 and 20 nm [90].

Figure 2.10 also shows the average flow stresses of solid core pillars with different grain sizes under cyclic deformation. The cyclic deformation has been used to study the fatigue [91] and strain hardening [92] of some metals. Schiotz [93] used atomic-scale simulation to investigate the strain-induced coarsening in nano-crystalline copper under cyclic deformation. In his simulation, the whole system was deformed under tension until a nominal strain of 10% was reached, then the deformation direction was revered and the sample was compressed until a strain of 10% was reached. The deformation was then reversed again, and the sample was elongated back to initial dimensions (0% strain). They repeated these cycles multiple times. In our actual experiments, the copper was compressed 5 times with the same nominal displacement each time. The results showed slightly softening compared with the solid core pillars under regular deformation test. The copper pillars under cyclic deformation were also observed the same grain-size effect as that under regular deformation.

Chapter 3 : Revealing mechanical properties of Cu pillars using MD simulations

3.1 Literature review

Cu is a typical FCC metal, which is ductile. It is widely used as the power cable because of its supreme electricity conductivity and relatively low prices. It is always desirable to combine its good electrical property with higher mechanical strength. As a result, lots of contributions have been made to study the mechanical properties of Cu [5], [94]–[101]. The investigation of Cu with the MD simulation has been made possible due to the massive development of the computation technology.

3.1.1 Indentation tests on Cu thin film by MD simulations

MD simulation of nano-indentation on Cu thin film was carried out by Fang et al. [99] to study Young's modulus and hardness. As shown in Figure 3.1 (a), the model consists of a mono-crystalline Cu layer and a rigid diamond that acts as the indenter tip, which is identical to the normal nano-indentation test. Periodic boundary conditions were imposed in the X and Y directions, and the bottom three layers of Cu atoms were fixed during the simulation process. The direction of the indentation was vertical to the sample surface along the Z-axis. The Morse potential instead of EAM potential was applied [102] with the purpose to reduce the computation consumption, however the results were comparable [103] under both potentials. Furthermore, different temperatures were used to investigate the

temperature effects on the mechanical properties of the Cu thin film. In my MD simulation, the temperature is fixed at 300K.

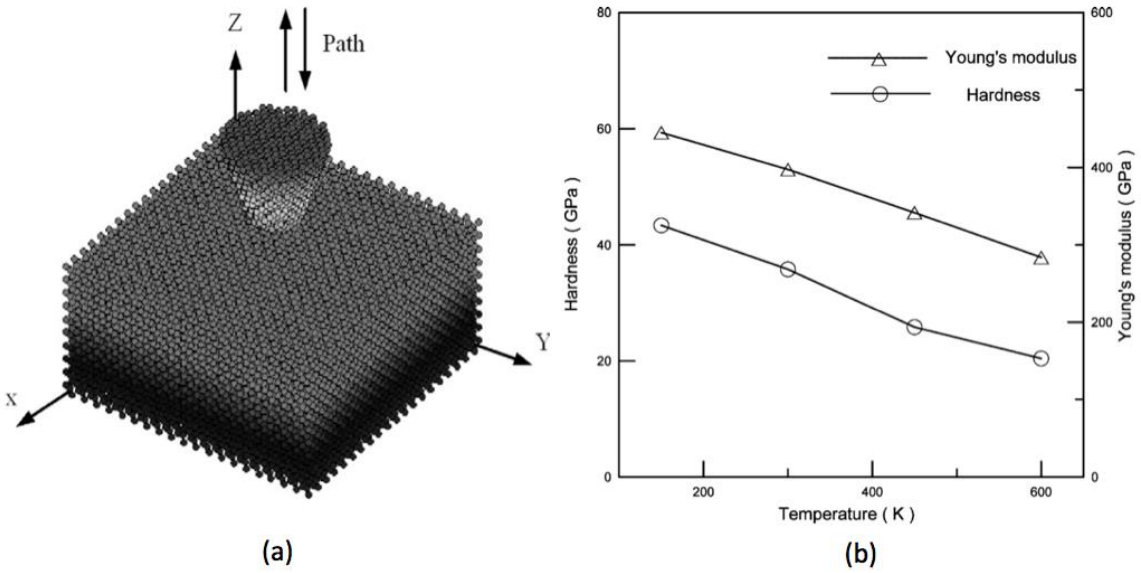

Figure 3.1: (a) Illustration of the MD simulation model. (b) Young's modulus and hardness of the simulated structure at different temperatures [99].

Temperature effects on the mechanical properties of Cu thin film are shown in Figure 3.1 (b). It was obvious that both the Young's modulus and hardness decreased with the increase of the temperature, which was consistent with the macro behavior and the elastic recovery was smaller at a high temperature. Compared with actual experiments, both the values of Young's modulus and hardness were higher. However, considering the scale difference between the micro-scale of experimental indentation and the nano-scale of MD simulation, this discrepancy was understandable. From the author's view, this can be explained by the different defect mechanism under deformation of micro- and nano-scale, and the surface energy to the elastic modulus with the decreasing thickness of thin films.

3.1.2 Tension tests on nano-crystalline Cu by MD simulations

This work was done by Zhou et al. [100] in 2014, carrying out the tension test to study the mechanical properties of the nano-crystalline copper by MD simulation. They built three-dimensional nano-crystalline copper samples with various mean grain sizes from 2.6 to 53.1 nm using Voronoi tessellation. In order to study the grain shape effects, two different grain shapes, spherical and cylindrical (shown in Figure 3.2 (a) and (b) respectively), were implemented in their models. Periodic boundary condition and EAM potential developed by Zhou et al. [104] were used in the MD simulation. Meanwhile, the temperature was fixed at 300 K during both the relaxing steps and tensile deformation steps. They set the strain rate at $10^8 s^{-1}$ to achieve a maximum strain of 20%.

The relationship between the flow stress and mean grain size from their results was displayed in Figure 3.2 (c). The maximum flow stress appears at a mean grain size of 8 - 20 nm. They identified three regions that were outlined in Figure 3.2 (c) and claimed that in each region the flow stress had a linear relation of different slopes with $d^{-1/2}$. A softening of nano-crystalline metal was observed when the grain size was smaller than 8 nm. The formation of three regions was explained with different deformation mechanism in each part. In the region with smallest grain size, the plastic deformation was observed in grain boundaries. In the middle region, the deformation twinning and detwinning were proposed to be a competitive mechanism. In the largest grain size region, no detwinning process was observed. Figure 3.2 (b) shows the effects of grain shapes on the flow stress of the nano-crystalline Cu. It is noticeable that the grain shapes had little effect on the flow stress,

which implied that, for different grain shapes, the plastic deformation mechanism was the same as long as the mean grain size kept equal. However, they observed the influence of grain shapes on the Young's modulus in their MD simulation, which the spherical grain had a higher Young's modulus.

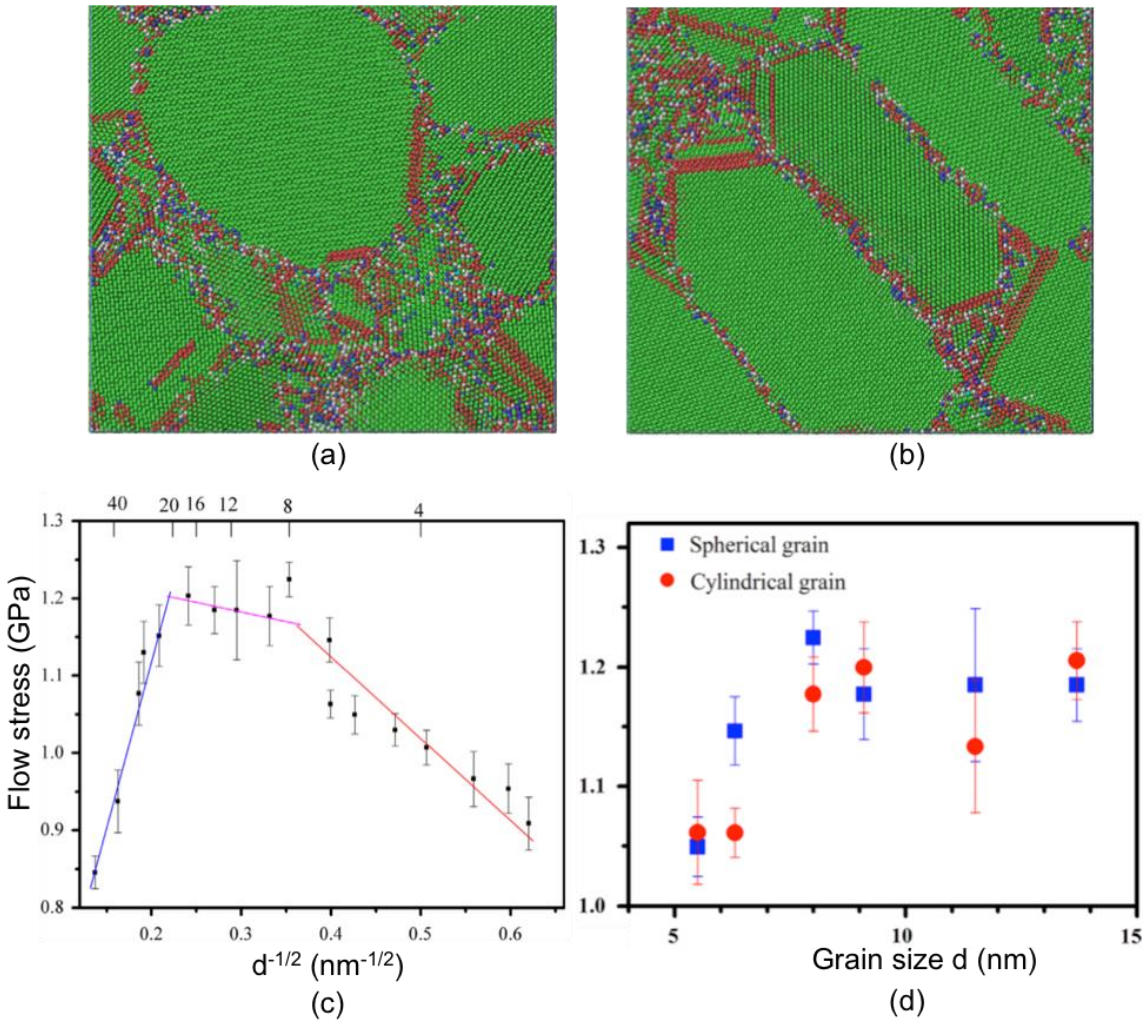

Figure 3.2: (a) (b) Illustration of the constructed MD models with spherical and cylindrical grain shapes respectively. (Only Y-Z plane is presented) (c) Plot of flow stress as a function of mean grain size. (Flow stress is defined as the average stress at an interval of strain from 12% to 20%) (d) Plot of flow stress versus grain size of samples with spherical and cylindrical grain shape [100].

3.1.3 Compression tests on nano-crystalline Cu by MD simulations

This MD simulation work done by Zhang et al. [101] focused the effects of the compaction of the nano-particles on the deformation of the nano-crystalline copper. The degree of the crystallinity (DOC) was used to describe the compaction, which was associated with three features, particle sizes, packing arrangement, and temperature. Generally speaking, the larger the particle size, the higher the DOC of the nano-crystalline materials. The FCC packing arrangements give the highest DOC and lower temperature favors a higher DOC number. The prepared nano-crystalline Cu samples were used to perform uniaxial compression along the X direction. The EAM potential proposed by Finnis et al. [105] was applied. Figure 3.3 (a) - (d) show the whole process from the preparation of sample to the compression.

They revealed the packing arrangements and the size of the compacted particles and the preparation temperature did affect the mechanical behaviors of the prepared nano-crystalline Cu, however, no unique relationship was observed between the DOC and the yield strength of the simulated structures. At a low temperature, the softening effects occurred during the compression process, while elastic-perfectly-plastic deformation was obtained at higher temperature. Additionally, the increase in the externally applied strain resulted in a decrease in the DOC value due to the mass shedding of the grains and thickening of the grain boundaries, which also had a negative effect on the formation of the voids and cracks in the nano-crystalline Cu.

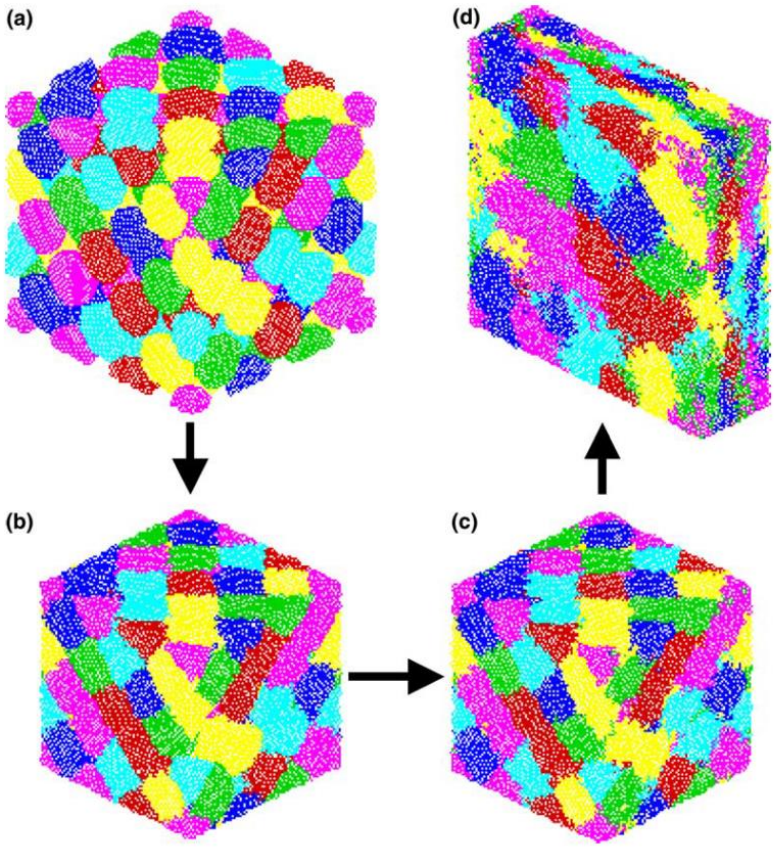

Figure 3.3: Illustration of the modeling sequence of the preparation and deformation of nano-crystalline copper under condition of FCC Packing, T=700k and with the particle size of 3.25nm. (a) The initial configuration of the packed copper particles. (b) After the compaction. (c) After relaxation. (d) After uniaxial compression [101].

3.2 MD simulation methods

3.2.1 Model building

The nano-crystalline model was built using the computer code implemented with Voronoi tessellation developed by Traiviratana [65], which can specify the dimensions and the number of grains inside the model. The original rectangular prism has a dimension of 30 × 30 nm in base and 42 nm in height, of which the mean grain size is 6 nm. The total number of atoms in this model is about 3,100,000.

This code enables a random orientation of each grain, which is desirable in MD simulation. A rectangular prism model of nano-crystalline copper structure is presented in Figure 3.4 (a). The solid core shaped and hollow shaped models can be achieved through cutting out of the rectangular prism model (shown in Figure 3.4 (b) and (c) respectively). For solid core shape, we built seven models with the varying outer diameters D, 30 nm, 21 nm, 18 nm, 15 nm, 12 nm, 10nm, and 9 nm. Hollow shapes are constructed with a fixed outer diameter 30 nm and the changing inner diameters d, 21nm, 20 nm, 18 nm, 15 nm, 12 nm, and 9nm. The aspect ratio of all Cu structures is kept at 1.4. This model construction method will ensure all the models of same mean grain size are from the exact same original model without grain orientation, grain boundary, or defect differences [106].

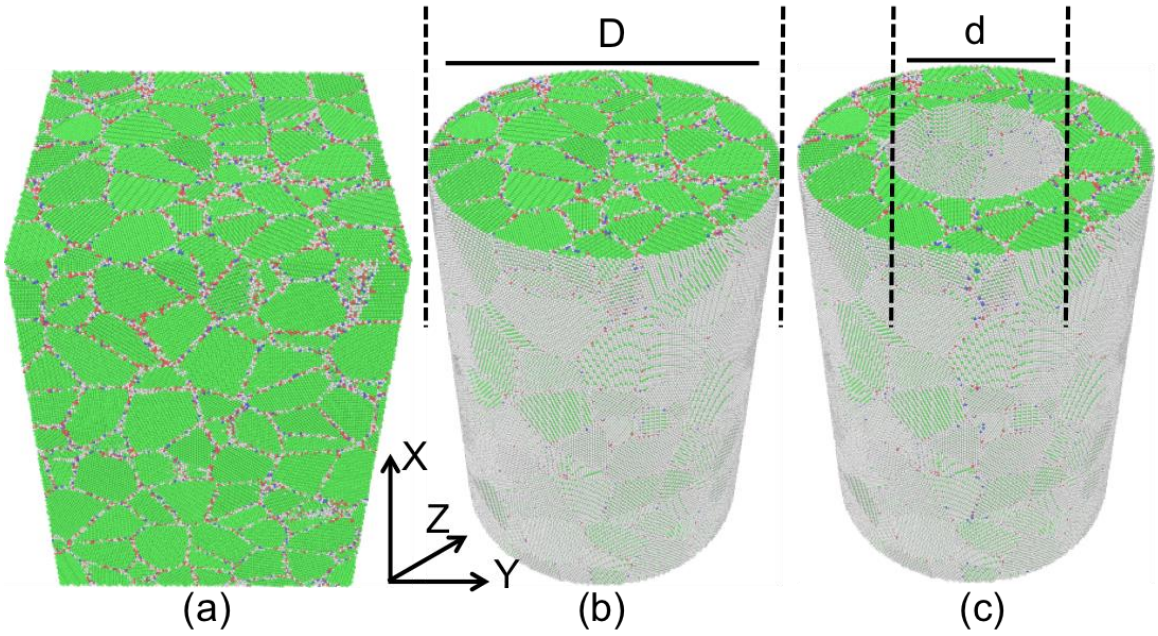

Figure 3.4: Representative models of constructed nano-crystalline copper with the mean grain size of 6 nm (Color coding based on Ackland and Jones analysis). (a) Rectangular prism with the dimensions of 30 nm, 30 nm and 42 nm. (b) Solid core shape with 30 nm in diameter and 42 nm in height. (c) Hollow shape with 30 nm in outer diameter, 15 nm in inner diameter and 42 nm in height.

3.2.2 Simulation setup and running

MD simulation is carried out using Large-scale Atomic/Molecular Massively Parallel Simulator (LAMMPS), a powerful classical Molecular Dynamic code, developed by Plimpton [107] in Sandia National Laboratories, Albuquerque. The LAMMPS codes are complied at the high performance computers (HPC) in Calcul Quebec, which are managed by Compute Canada and funded by the Canada Foundation for innovation (CFI) and other governmental agencies. The number of CPU cores used in all the simulations described in this thesis is kept 600.

The EAM potential for Cu extracted by Zhou et al. [104] was applied to characterize the inter-molecular forces. Periodic boundary condition was imposed along pillar axis (X direction), and the other two directions were kept free for the pillar structures. The simulation time step was set to be 5 femtoseconds, which was computation sufficient and still produced reliable results [53] (Effects of different time step length will be discussed in the results and discussion section).

Prior to the deformation steps, energy minimization steps were first carried out using the conjugate gradient (CG) method. Subsequently, the atoms were assigned a random velocity at the beginning and the simulation model was relaxed under zero pressure using isothermal-isobaric (NPT) ensemble with Nose-Hoover thermostat for 40,000 steps that equal to 200 picoseconds (Effects of relaxation time will be discussed in the results and discussion section).

Deformation steps started upon the completion of relaxation steps. Both compression and tension were tested along the pillar height axis (X direction) using canonical ensemble (NVT) for 400,000 steps (2,000 picoseconds). This process was

carried out by straining the simulation box along its designated direction at a constant strain rate of $10^8\ s^{-1}$. This high strain rate in the MD simulation compared with that in actual experiments is a compromise of the limited computation resources, however, it can still produce reliable results and has been used by lots of researchers [17], [53], [54], [64], [100], [108]. The maximum strain can reach up to 20% with the combination of the strain rate of $10^8 s^{-1}$ and the deformation time of 2,000 ps. The deformation steps took place at the fixed temperature of 300 K. The calculation of flow stress was done on the fly during the deformation steps by adding the local Virial stress [62] along the loading direction over all the atoms and divided by the volume of the model.

3.2.3 Visualization

The visualization of atomistic configurations and structure identification were done by using the software OVITO, which was developed by Stukowski [109]. The dump file data was loaded to the software and the images can be produced based on the coordination information included in the file and certain analysis method, such as CNA, BAA, can be imposed to generate the detailed structural information. Dislocations were first analyzed using the computer code CrystalAnalysis implemented with the dislocation extraction algorithm, which was written by Stukowski [110] and then visualized using open-source software ParaView developed by Sandia National Laboratory, Kitware Inc. and Los Alamos National Laboratory.

3.3 Results and discussion

3.3.1 Relaxation time and time step effects

In order to validate the effects of the relaxation time, simulations were carried out at four different time lengths, 50 ps, 200 ps, 300 ps, and 600 ps, with time steps of 5 ps. All other parameters were kept exactly the same. The model used in this batch of simulations is the hollow shaped pillar with a grain size of 6 nm and the inner diameter of 21 nm, since this model contains relatively fewer atoms and can reduce the running time.

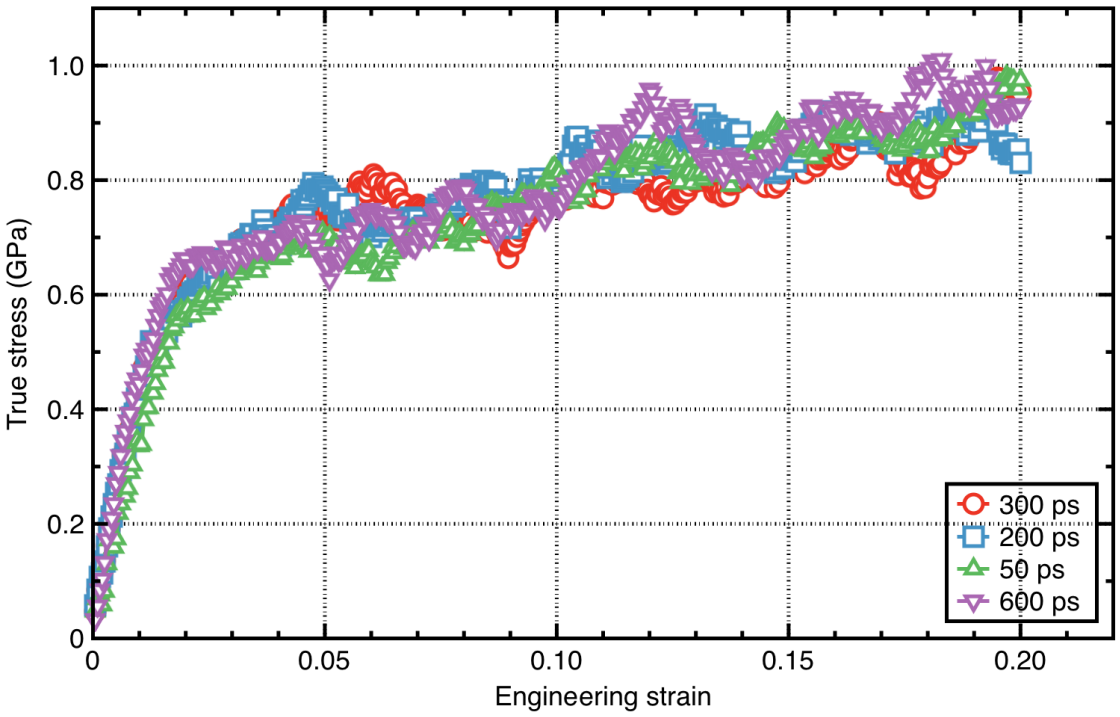

Figure 3.5: Plot of stress – strain curves with each color representing different relaxation times (carried out under compression)

Figure 3.5 shows the stress-strain curves of each relaxation time. Generally, no significant difference is observed from the curves and each curve gives a similar

mechanical response. The flow stress and Young's modulus are calculated using the stress-strain data. The average flow stress (5% strain to 20% strain) for all the four relaxation times is within the range of 0.80 – 0.84 GPa, and taking the standard deviation into consideration, the values are roughly the same. The Young's modulus for the 50 ps relaxation time is 20.72 GPa (0.2% strain), which is less than half of the Young's modulus of the other 3 relaxation time lengths (51.11 GPa for 200 ps, 44.53 GPa for 300 ps and 50.27 GPa for 600 ps). Therefore, when running MD simulations, too little relaxation time can be a concern because it results in a low Young's modulus. A 200 ps relaxation time in my simulation is the point keeping both the resources efficient and results reliable.

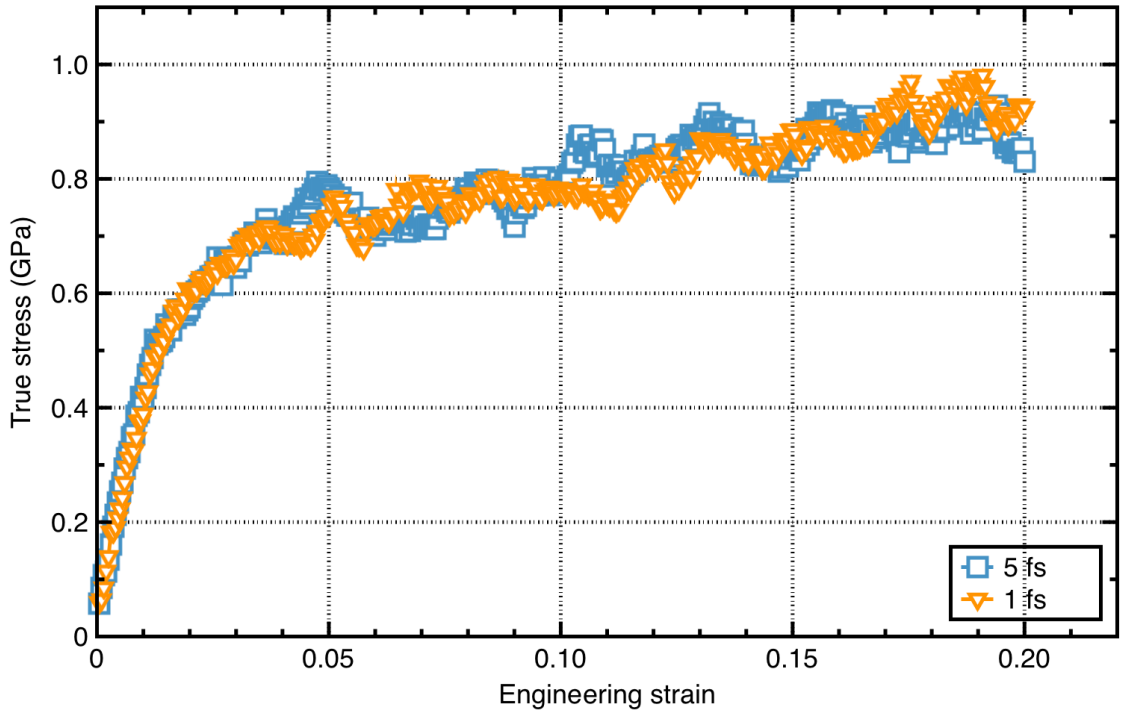

Figure 3.6: Plots of stress-strain curves with each color representing different time steps. (carried out under compression)

Different time steps of the MD simulation have also been tried to test the time step effect. As displayed in Figure 3.6, the stress -strain curves for the 1 fs and 5 fs are very similar, and these two time steps share almost the same elastic deformation part. The flow stresses for both time steps are around 0.82 GPa. The Young's modulus for the 1 fs is 44.13 GPa, which is a little lower than that for the 5 fs. As a result, 5 fs is preferred in all the runs, which can save a significant amount of computation time. Theoretically, to achieve the same amount of deformation with the same strain rate, the whole running process for 5 fs only needs one fifth the time needed for 1 fs.

Herein, we keep consistent with our relaxation time of 200 ps and time step of 5 fs throughout all the simulation models.

3.3.2 Results from compression tests

3.3.2.1 Stress-strain behavior

Figure 3.7 shows the stress-strain behavior of solid core shaped pillars with various dimensions under compression. It can be observed that the flow stress is dependent on the size. The solid core pillar with a 10 nm outer diameter has an average flow stress of 0.73 +/- 0.08 GPa, while the pillar with the largest outer diameter of 30 nm has an average flow stress of 1.15 +/- 0.02 GP. Additionally, the yield stress also represents a "smaller is softer" effect [106]. It is noticeable that the pillars with larger dimension possess a smoother stress curve, compared with the smaller-dimension pillars. In particular, the stress-strain curve for the 9 nm outer diameter pillars fluctuates a lot with the highest stress of 1.8 GPa and lowest stress

of 0.2 GPa. This phenomenal plasticity activity happens when the sample diameters approach the grain size in the objects. This distinct serrated stress-strain curve results from the dislocation nucleation and sudden surface slip via the grain boundaries. The plasticity region for the largest pillar structure is quite flat, indicated by a plateau in the plots.

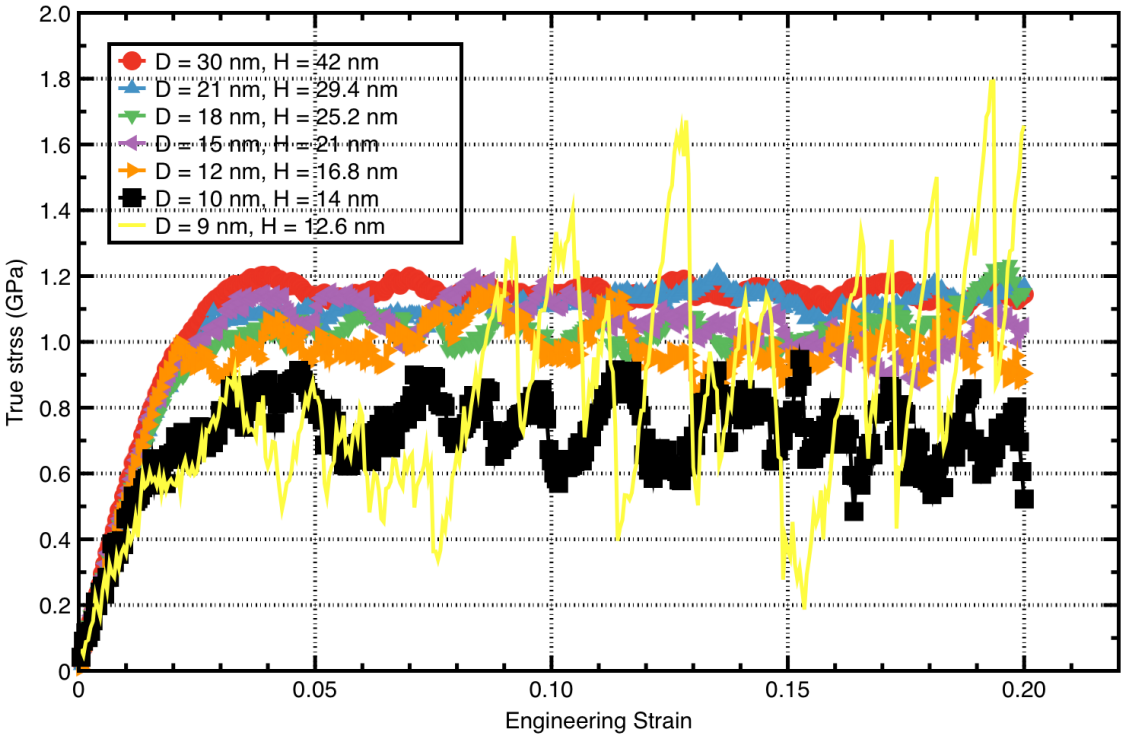

Figure 3.7: Plots of stress-strain curves of solid core shaped pillars with each color representing different dimensions. (carried out under compression)

Furthermore, the diameter difference between the 30 nm diameter pillar and 21 nm one is 43%, while their stress-strain curves are similar, with the average flow stresses of 1.14 +/- 0.02 GPa and 1.12 +/- 0.03 GPa respectively, which is less than 2% difference. In contrast, the average flow stresses between 10 nm and 12 nm diameter pillars are 0.73 +/-0.08 GPa and 0.99 +/- 0.07 GPa respectively, which is 20% difference in the outer diameter and 35% in the flow stresses. These results

show an increasingly significant size effect on the stress when the dimensions are decreasing.

The stress-strain curves of hollow shaped pillars under compression are displayed in Figure 3.8. These pillars maintain the same outer diameter of 30 nm and same height of 42 nm, with the inner diameters varying from 9 nm to 21 nm. The average flow stresses for the hollow pillars with inner diameters of 9 nm, 12 nm, 15 nm, 18 nm, 20 nm and 21 nm are 1.08 +/- 0.03 GPa, 1.06 +/- 0.02 GPa, 1.01 +/- 0.04 GPa, 0.94 +/- 0.05 GPa, 0.86 +/- 0.06 GPa and 0.83 +/- 0.06 GPa respectively. These stress-strain behaviors show a clear trend: the thinner the sidewall, the softer the pillar.

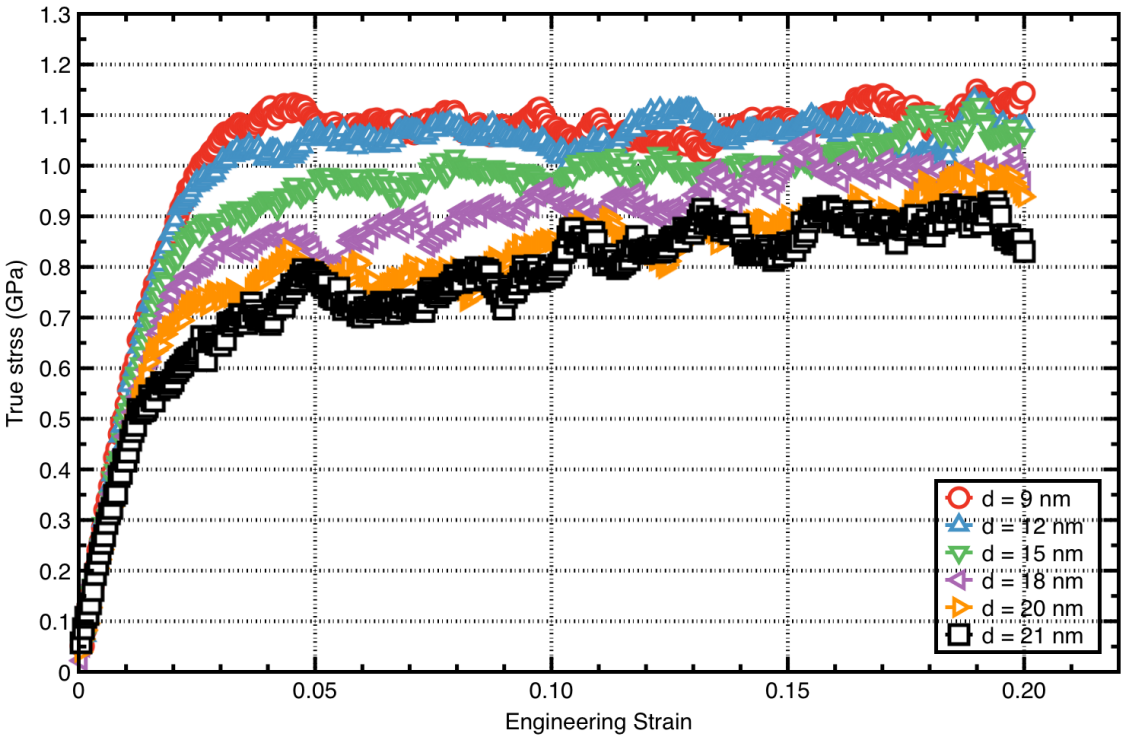

Figure 3.8: Plots of stress-strain curves of hollow pillars with each color representing different inner diameters. (carried out under compression)

In the perspective of the single pillar deformation behavior, the ones with the inner diameters of 21 nm, 20 nm, 18 nm and 15 nm show a gradual increase of the stress in the plasticity deformation regime, which imply a hardening effect. This can be validated by calculating another average flow stress from 5% strain to 10 % strain, showing an increase of 10%, 9%, 6% and 3% of flow stress with the increase of the strain from 10% to 20%. For the pillar with inner diameter of 12 nm and 9 nm, no significant flow stress increase can be observed, and this no-stress-increase trend can also be extended to smaller inner diameter pillars because the solid core pillar with a 30 nm outer diameter can be considered as a hollow pillar in extreme cases with a 0 nm hole size and of course there is no stress increase either.

The difference of stress-strain behavior between the solid core and hollow shaped pillars are also noticeable. Generally, no stress increase is found in solid core pillars. There is no stress-strain curve fluctuating in hollow pillars even when the wall thickness is reduced to 4.5 nm for the largest inner diameter pillar. This difference is worth noticing, since the wall thickness is even smaller than the grain size, which implies the hole inside the pillar structure really plays a role in the deformation mechanism. The elastic regime of both shapes of pillars is very similar.

Detailed explanations of these phenomenal stress-strain behaviors will be addressed in the following sections.

3.3.2.2 Atomistic configuration

The atomistic configuration of the simulated objects is very useful to analyze the microstructural evolution during the deformation process. Figure 3.9 gives selected snapshots of the solid core pillars with a 30 nm outer diameter and 42 nm

in height. With the strain increasing from 2% to 10%, deformation twinning happens by partial dislocations emitting from grain boundaries, as indicated in Figure 3.9 (b). The deformation twining can happen both inside the grain and between two grains. It can be observed on the Figure 3.9 (b) bottom that the deformation twining exists at the grain boundary area, which forms a grain-boundary-twin intersection. The portion of the FCC atoms that indicates lattice atoms is decreasing from 79% to 71% with the strain increasing from 2% to 10%, proving that the formation of the twins and other defects happened during this strain period. With the strain continuing to increase to 20%, both twinning and detwining take place, maintaining the defect density almost unchanged, which can be validated by the unchanged FCC atom percentage at the 10% strain and 20% strain levels.

Grain rotation is also observed during the deformation process, and accommodates the stress buildup induced by the grain boundary sliding. For nano-crystalline metal, the grain boundary sliding is the dominant mechanism and as such the grain boundary sliding can be seen as a precursor of the grain rotation. Grain rotation has been observed in many MD simulations [111][112] of metals with small grain size. Experimental observations of the grain rotation in Ni [113]and Al [111] have also been reported using a transmission electron microscope (TEM). The grain rotation is a multi-element driven process, which is dependent on external stress and crystallographic misorientation in the neighboring grains. Other deformation mechanism, such as grain boundary sliding, partial dislocation and grain diffusion can also accompany the grain rotation [100].

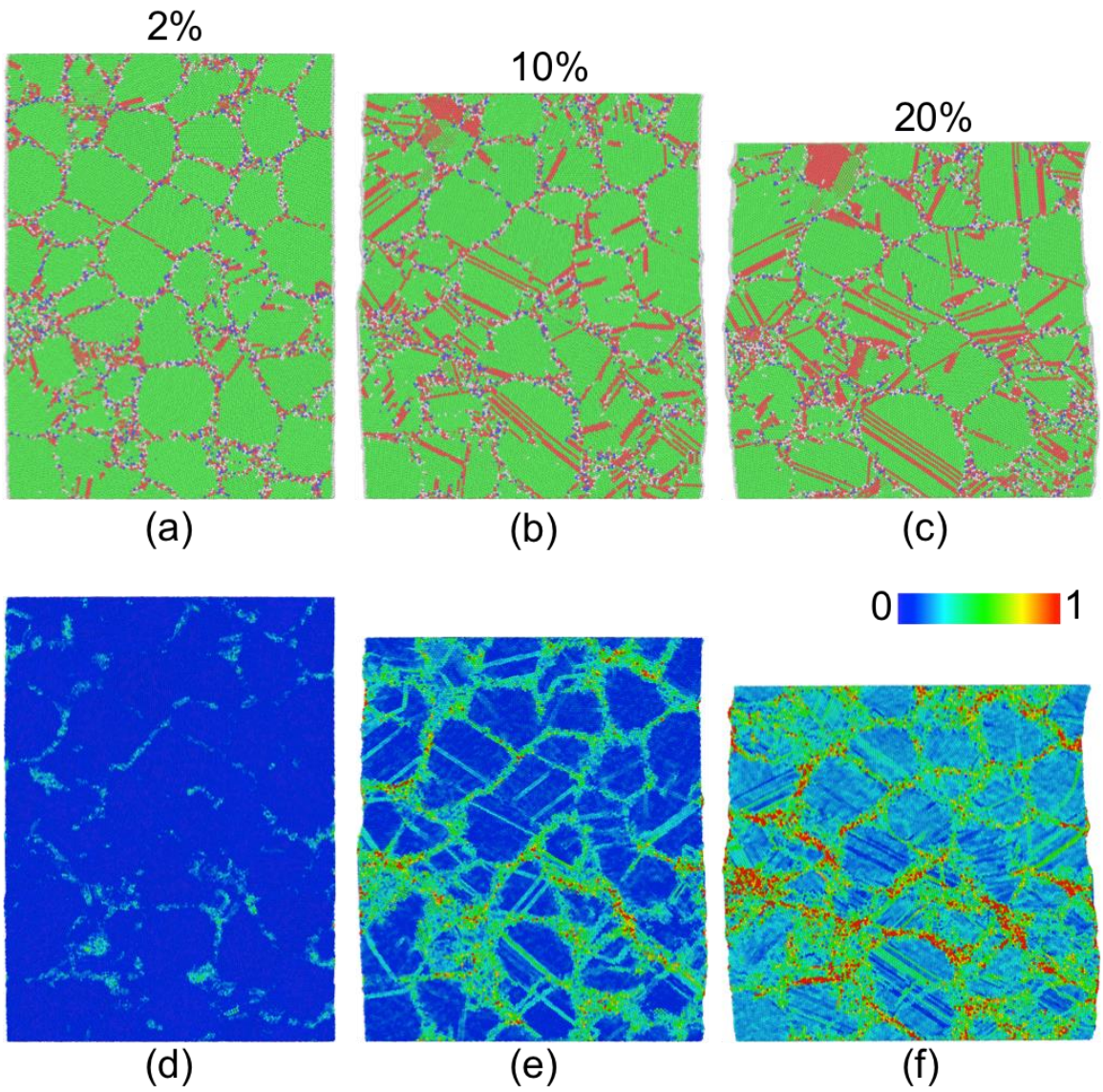

Figure 3.9: Representative snapshots of sliced solid core pillar with a 30 nm outer diameter and 42 nm in height. (a)(b)(c) Atomistic configuration at different strain (color coding based on the Ackland and Jones analysis). (d)(e)(f) Local von Mise strain corresponding to each atomistic configuration with the reference state at the strain of 0 (color scheme based on the magnitude of strain with blue representing no strain and red representing the strain of 1).

Local von Mise strain is displayed in figure 3.9 (d)(e)(f), which is corresponding to each strain. Generally, the atoms around the grain boundary and the twins have much larger strain than the atoms inside the grain, which indicates

most deformation takes place at the grain boundary regions and the grain boundary sliding is the main mechanism during the deformation process. As shown in figure 3.9 (f), some atoms possess a local strain of around 100%, which is much larger than the overall strain of 20%. These atoms are located in the grain boundary regions.

As discussed above, the stress-strain behavior of the 9 nm solid core pillar is different from that of the pillars with larger dimensions, a phenomenon related to the inner structures. The atomistic configurations of the solid core pillar with 9 nm outer diameter are displayed in the Figure 3.10 and each snapshot represents a different strain. Since the grain size is comparable to the diameter, this solid core pillar possesses only about 3 grains, which resemble the lamella structures. Figure 3.10 (a) shows the initial configuration, and the majority is occupied by the grain on the top. The deformation twinning and detwinning are observed during the deformation process. From 16% strain (figure 3.10 (d)) to 20% strain (figure 3.11 (f)), the detwinning overtakes the twinning as the dominant deformation mechanism. After 20% deformation, this solid core pillar is approximate to the single-crystalline structure and as shown in Figure 3.10 (f), very little defect is observed. Compared with the 30 nm solid core pillar, the 9 nm pillar maintains the same grain size and aspect ratio. The difference of the surface-volume ratio between these two different dimension models also plays an important role in their mechanical behavior. With the decreasing of the diameter, the defects like dislocation, twinning and grain boundary become easier to annihilate at the free surface (Compared with the 30 nm pillar, these defects in the 9 nm pillar travel less

distance before annihilating at free surfaces). The surface slip was also aided by the sliding of the grain boundary that intersected with the free surface.

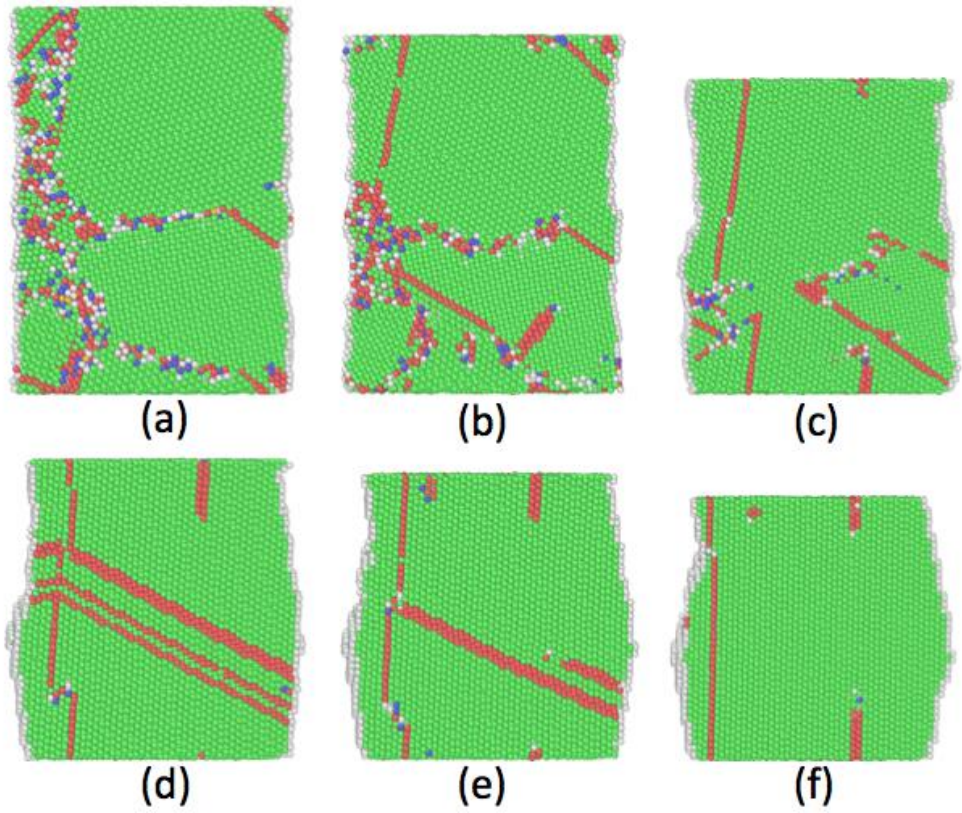

Figure 3.10: Representative snapshots of sliced solid core pillars with 9 nm in outer diameter and 12.6 nm in height. (Color coding based on Ackland and Jones analysis) (a)(b)(c)(d)(e)(f) Snapshots at strain of 0, 4%, 10%, 16%, 18% and 20% respectively.

The atomistic configurations of selected hollow pillars are presented at Figure 3.11, which shows the models of hollow pillars with inner diameter of 9 nm and 18 nm respectively. As mentioned above, all the models are cut from the same original rectangular prism. Theoretically, the only difference between these hollow pillars should be the size of the hole inside the structure. The grain and defect distribution are the same. However, minor differences can be observed in the initial states of the hollow pillars, as shown in the dashed circles of the Figure 3.11 (a) and

Figure 3.11 (e). This minor difference is believed to be caused by the atom motion during the relaxation steps in the MD simulation process.

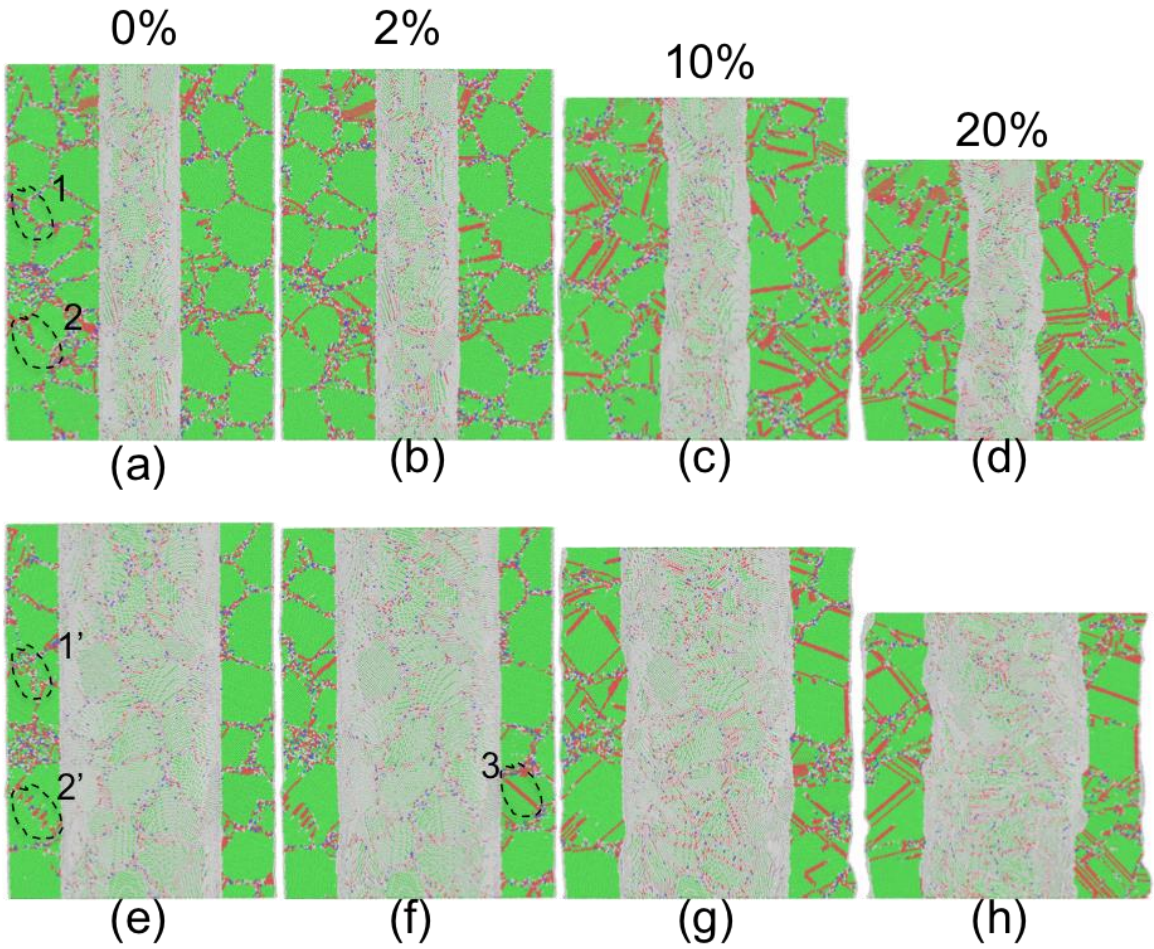

Figure 3.11: Representative snapshots of hollow pillar with a 30 nm outer diameter and 42 nm height at different strain (color coding based on the Ackland and Jones analysis). (a)(b)(c)(d) 9 nm inner diameter. (e)(f)(g)(h) 18 nm inner diameter.

During the early stage of the deformation (0% to 2%), the grain structure does not change much and very few defects were introduced in the pillar structures. As displayed in the Figure 3.11 (e) and Figure 3.11 (f), only one boundary (dashed area 3) can be observed inside the grain between these two snapshots. With the deformation going up to 10%, more defects were introduced to the hollow pillar

structures. The twinning and detwinning process compete with each other from 10% strain to 20% strain, which can be validated by observing no obvious twining density change between Figure 3.11 (c) and Figure 3.11 (d). Since hollow structure provides more free surface compared with the solid core pillars with 30 nm outer diameter, the defects in the hollow pillar become easier to annihilate at the free surface, and grain boundary sliding is enhanced by the presence of more free surface.

The wall thickness of the hollow pillar with 18 nm inner diameter is 6 nm, which equals to the grain size. Very few complete grains can be observed in Figure 3.11 (h), and the grain boundary is more likely to intersect with the free surface. The grain boundary sliding is enhanced by this increasing grain boundary free surface intersection, which contributes to a lower stress compared with the hollow pillars with smaller inner diameter.

3.3.2.3 Dislocation analysis

The dislocation analysis was carried out using the Dislocation Extraction Algorithm [114]. There are three principal steps included in this method. Firstly, all the atoms are classified as two categories: one is the crystalline atoms, referred to as good atom and the other is defects which are disordered atoms. Secondly, the disordered atoms are separated by a closed, two-dimensional manifold from the crystalline atoms. Thirdly, for each dislocation segment, an initial Burgers circuit is generated on this manifold. The closed circuit is moved in both directions to the two opposite ends of the dislocation segment to capture its shape. The one-dimensional line can be constructed as the dislocation segment when the closed circuit is

advanced in each direction. This dislocation construction method performs well in dislocation analysis [115].

The evolution of the dislocation density in the solid core pillar is displayed in the Figure 3.12, and the dislocation density is normalized by their initial dislocation density at 0% strain, which is within the range of 1.7×10^{17} to 2.9×10^{17} m^{-2}. The experimental nano-twinned copper was reported to have an initial dislocation density of around 10^{14} m^{-2} by Lu [116]. This discrepancy can be explained by the different crystalline structures introduced in the samples and the different nature of the MD simulation and experimental method. Li [23] constructed a Cu model that was dislocation-free at the initial state. However, the dislocation density rapidly increased to around 10^{16} m^{-2} during the plasticity deformation and reach around 10^{17} m^{-2} at 10% strain, which is identical to our model. As indicated in the Figure 3.12, all the solid core pillars, except the ones with 10 nm and 9 nm outer diameters, maintain an overall increasing trend of dislocation density when the strain is increased. The dislocation density of the 10 nm outer diameter one almost doubles at the 10% strain and then drops to a lower level. The solid core pillar with 9 nm outer diameter reaches to the highest dislocation density at around 6% and then it decreases dramatically to a much lower level than the initial dislocation density. As discussed in the former section, the stress-strain behavior for the smallest dimensional pillar was different from the others, which fluctuates a lot. This unique dislocation density evolution behavior is partially responsible for it. The smaller the dimension is, the easier the dislocation annihilate at the free surface, which leads to

the dislocation density drop with the increasing of the deformation applied to 9 nm outer diameter pillar.

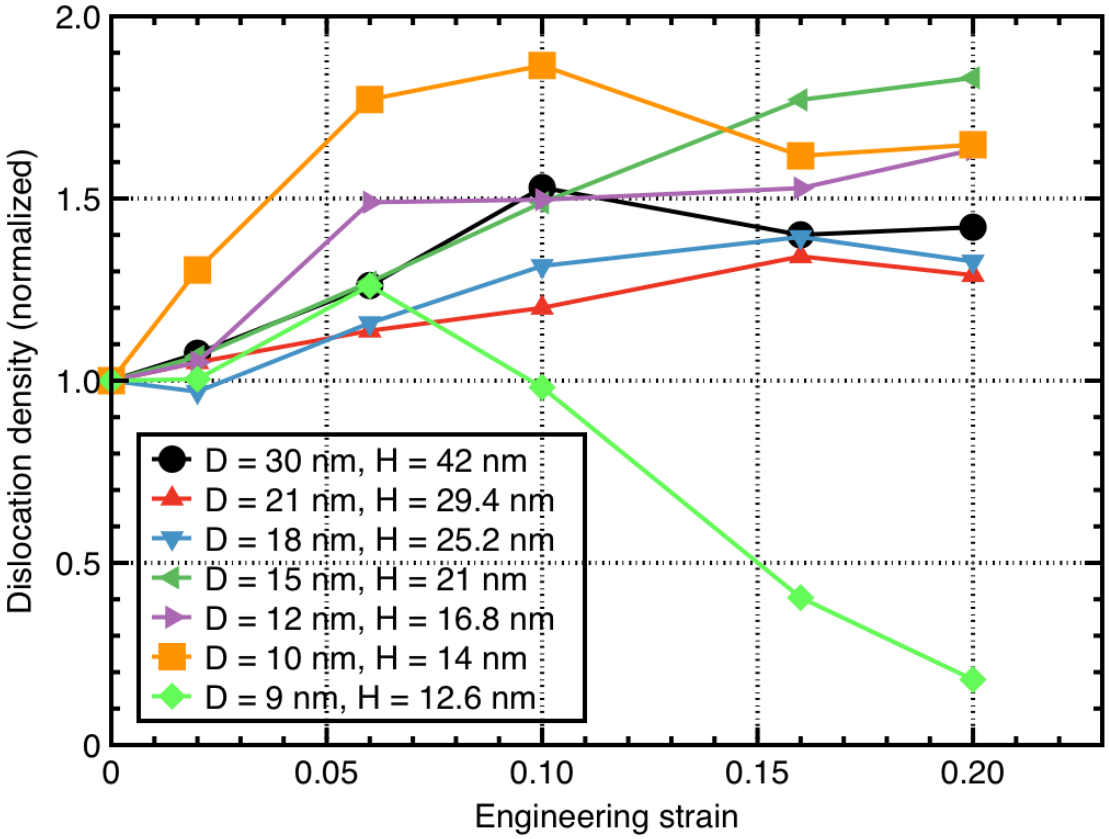

Figure 3.12: Plots of dislocation density with the engineering strain of the solid core pillars (The dislocation density is normalized by its initial state)

In order to take an in-depth look at the solid core pillar with 9 nm in outer diameter, we visualize the dislocation. Representative dislocation configurations at 0%, 2%, 6%, 10%, 16% and 20% strain are displayed in Figure 3.13. At the initial state, most of the dislocations are very short but elongate when the strain is increased, which can be observed from Figure 3.13 (a) to Figure 3.13 (b). Some dislocations annihilate at the free surface, and new dislocations can nucleate from the grain boundary. Because of its limited size of model, less grain boundary and

more free surfaces exist in this 9 nm outer diameter solid core structure. As shown in Figure 3.13 (f), few dislocations remains after 20% strain, which proves the hypothesis that the nucleation rate of the dislocation from the grain boundary and other sources is less than the annihilation rate of the dislocation at the free surface.

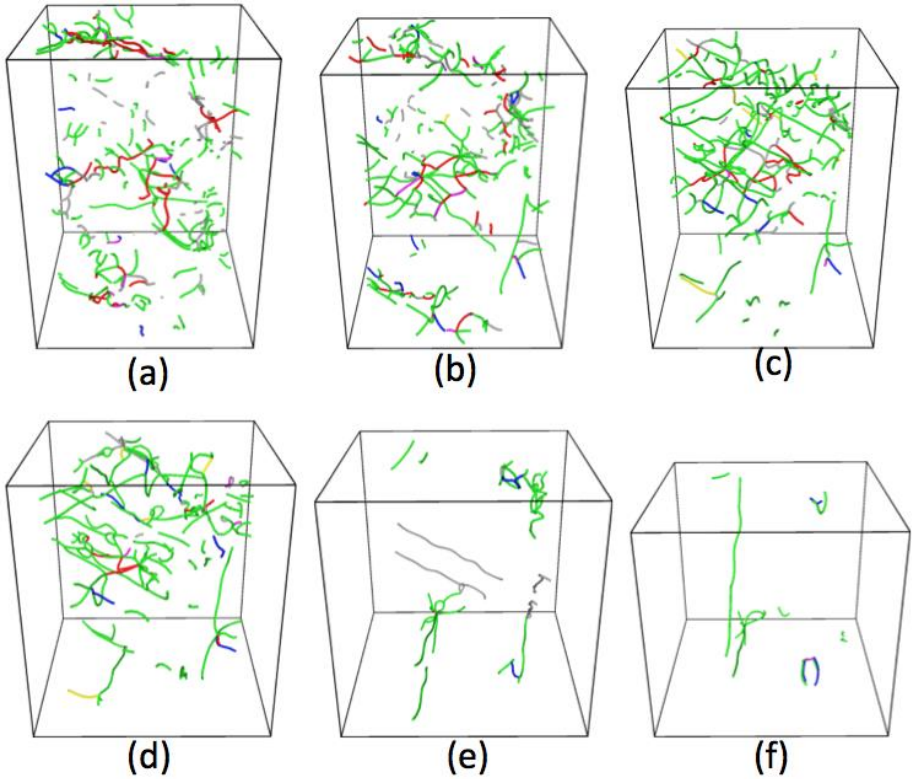

Figure 3.13: Representative dislocation configuration of the solid core pillar with 9 nm in outer diameter (a)(b)(c)(d)(e)(f) represents the state at 0%, 2%, 6%, 10%, 16% and 20% strain.

It is interesting to see more deformation (beyond 20% strain) is placed on this 9 nm solid core pillar. We assume that this dislocation-decreasing trend will be still observed. However it remains to be seen whether a dislocation-free pillar can be achieved with more deformation applied. According to Greer's dislocation starvation theory [80], dislocations in sub-micron crystals can travel only very small distance before annihilating at free surfaces, thereby reducing overall dislocation

multiplication rate. Gliding dislocations leave the crystal more rapidly than multiplication, decreasing the overall dislocation density. This process will lead to a dislocation starved state requiring higher stress to nucleate new dislocations. Discrepancy exists when applying this theory to the solid core pillar with 9 nm outer diameter. The dislocation density follows the overall decreasing trend after a certain amount of strain. However, the stress of the pillar fluctuates a lot, which is not corresponding to a stable enhanced strength of the pillar structure. Furthermore, no significant dislocation starvation effect is observed for the pillars with larger dimensions. Thus, we assume the grain size compared to the structure dimension also matters to this notable effect, which is also observed in other MD simulations [106][64].

The relationship between the dislocation density and strain is shown in Figure 3.14, which is more uniform compared with that of the solid core pillars. Until the strain of 10%, the dislocation density shows a steady increase. The initial dislocation density of the hollow pillars is within the range of 2.7×10^{17} to 3.0×10^{17} m^{-2}, which is comparable with that of the solid core pillars. As discussed above, the stress-strain behavior for hollow pillar with 21 nm, 20 nm, 18 nm, and 15 nm shows a stress increasing effect during the plastic deformation period. However, no significant difference in the dislocation density between these hollow pillars with different inner diameters can be observed from Figure 3.14. As a result, we assume the dislocation is not the driving mechanism for the stress-increasing phenomenon in the hollow pillar with relatively larger diameter. For the hollow pillar with 21 nm inner diameter, the wall thickness is 4.5 nm, which is less than the grain size, and we

assume there is no complete grain in side this hollow pillar. Additionally, the surface-volume ratio of the solid core pillar with 9 nm outer diameter and the hollow pillar with 21 nm inner diameter is equal (Detailed surface area-volume effect will be discussed in the next section). However, the dislocation density of the hollow pillar does not drop below the initial dislocation density after 20% strain.

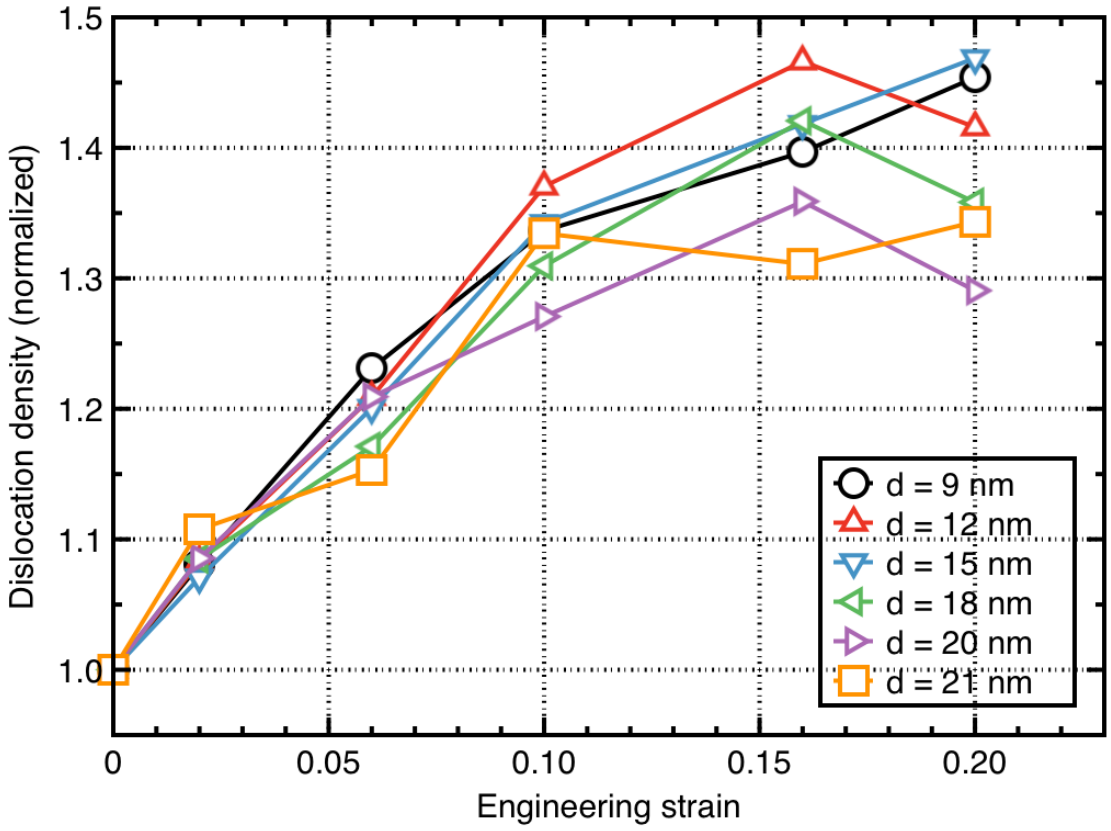

Figure 3.14: Plots of dislocation density with the engineering strain of the hollow pillar (The dislocation density is normalized by its initial state).

3.3.2.4 Free surface effects

The free surface in MD simulation is defined as the surface that does not undergo any constraint during the simulation process. As a result, the boundary condition imposed in each direction is related to the existence of the free surface. As

the periodic boundary condition is only applied to the X axis (height direction), the free surface in the solid core pillar is the outer lateral surface, and for the hollow pillar, the additional inner surface is also considered as the free surface. A rectangular prism model can be built without any free surface by imposing periodic boundary condition at all three directions, which can be treated as a bulk material. Therefore, the area-volume ratio of 0 is corresponding to the bulk model. The area-volume ratio of 0.133, 0.190, 0.222, 0.267, 0.333, 0.400, 0.444 nm^{-1} are corresponding to the solid core pillar with outer diameter of 30, 21, 18, 15, 12, 10, 9 nm respectively. The surface area-volume ratio of 0.190, 0.222, 0.267, 0.333, 0.400, 0.444 nm^{-1} are corresponding to hollow pillars with inner diameter of 9, 12, 15, 18, 20, 21 nm respectively.

Flow stress of the solid core pillar with respect to the surface area-volume ratio was plotted in the Figure 3.15. The flow stress is taken from the average true stress between 5% and 20% strain. The bulk sample was added to the plot as the surface area-volume ration of 0. Generally, the flow stress decreases with the increase of the surface area-volume ratio. The solid core pillar with 9 nm outer diameter that represents an area to volume ration of 0.444 nm^{-1} shows a discrepancy with a large standard deviation. This has already been discussed above due to its fluctuated stress-strain curve that is reversely affected by the free surface area. As shown in Figure 3.12, the decreasing dislocation density with the increasing strain for the solid core pillar with 9 nm also results from this highest area volume ration, since the presence of the free surface enhances grain boundary sliding with a lower fraction of deformation being carried out by the dislocation [106].

Additionally, the flow stress of the solid core pillar with the area to volume ration of 0.4 nm^{-1} is relatively low.

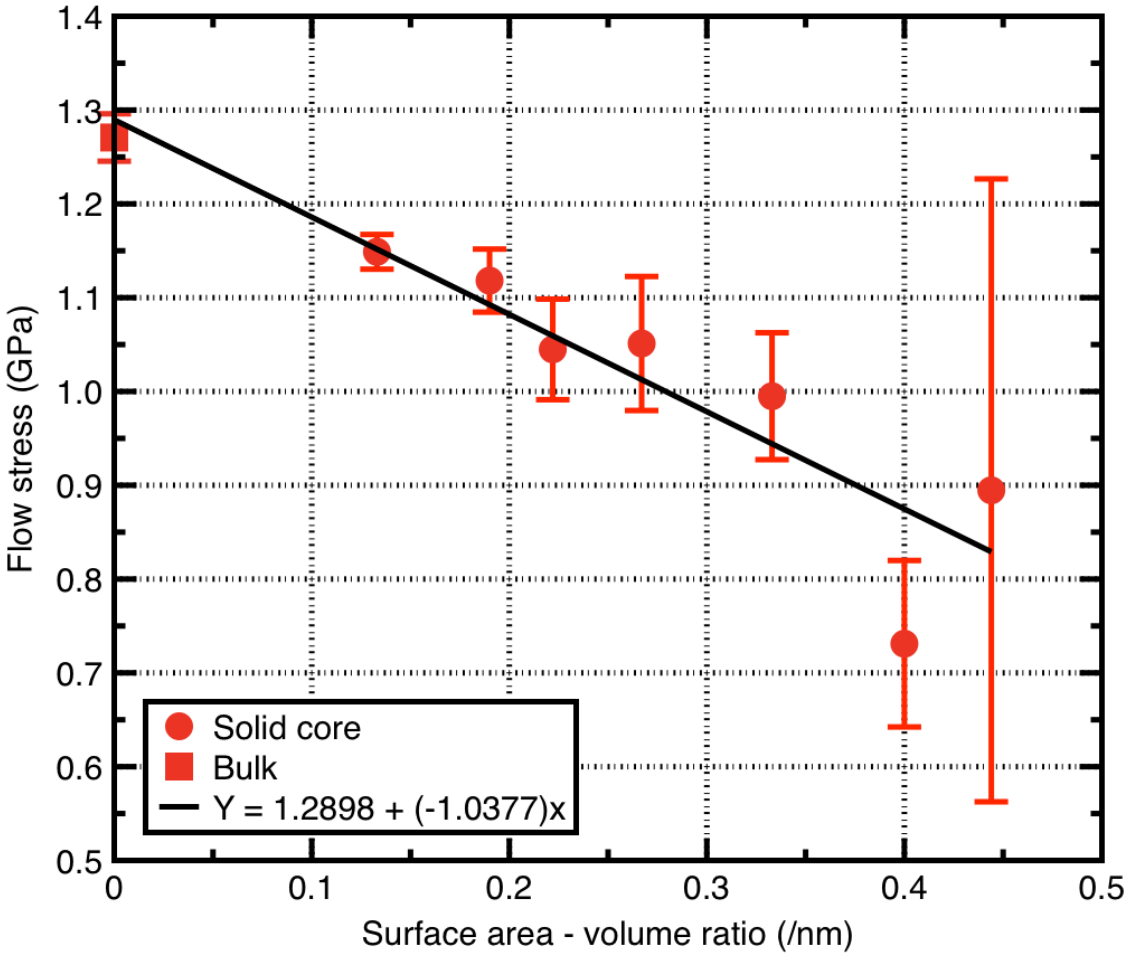

Figure 3.15: Plots of flow stress with respect to the surface volume ration for the solid core pillar under compression (The flow stress is taken from the average true flow stress between 5% and 20% strain and the error bar represents one standard deviation)

For the hollow pillars, the flow stress – area to volume ratio has also been plotted in figure 3.16. Compared with the solid core pillar, the hollow pillar shows a consistent decreasing trend. Similarly, adding the bulk model as the area to surface ration of 0, a fitting line of $Y = 1.2764 - 1.0152X$ can be reached with all the data points aligned well in this line. With the size of the hole inside the hollow pillar

decreasing, the flow stress will increase. Considering the solid core pillar with 30 nm outer diameter as an extreme case of hollow pillar with the hole size of 0 nm, the flow stress of 1.15 GPa with area to volume ratio of 0.133 nm^{-1} also fits in this trend line $Y = 1.2764 - 1.0152X$ of the hollow pillars. This distinguished relationship between the average flow stress and the surface area to volume ration for hollow pillars can lead to a unique construction to get a desired strength of nano-sized structures. Since the top and bottom surface do not account as the free surface, the surface area to volume ration is independent on the height, and the construction of nanotubes can also be guided by this relationship.

Furthermore, it is really interesting to notice the different behavior of the flow stress - area to volume ratio between the solid core and hollow pillars. Particularly, the solid core pillar with outer diameter of 10 nm and the hollow pillar with inner diameter of 20 nm share the same surface area – volume ration of 0.4 nm^{-1}, however, the flow stress of the solid core is 0.73 +/- 0.09 GPa, which is about 15% lower than the flow stress of 0.86 +/- 0.06 GPa of the hollow pillar. Nevertheless, this is not a uniform trend, and other solid core pillars have a higher flow stress than their counterparts. This discrepancy between the solid core and hollow pillars is worth investigating. The free surface of the hollow pillars consists of two parts with inner surface and outer surface, and it is unknown whether these two parts play the equal role in their stress responses. The free surface of the solid core pillars is just the outer surface with out any outer surface inside. The free surface can also act as the annihilation site of the dislocation as mentioned above, which is also the

explanation of the dislocation density difference between the solid core pillar and the hollow pillar.

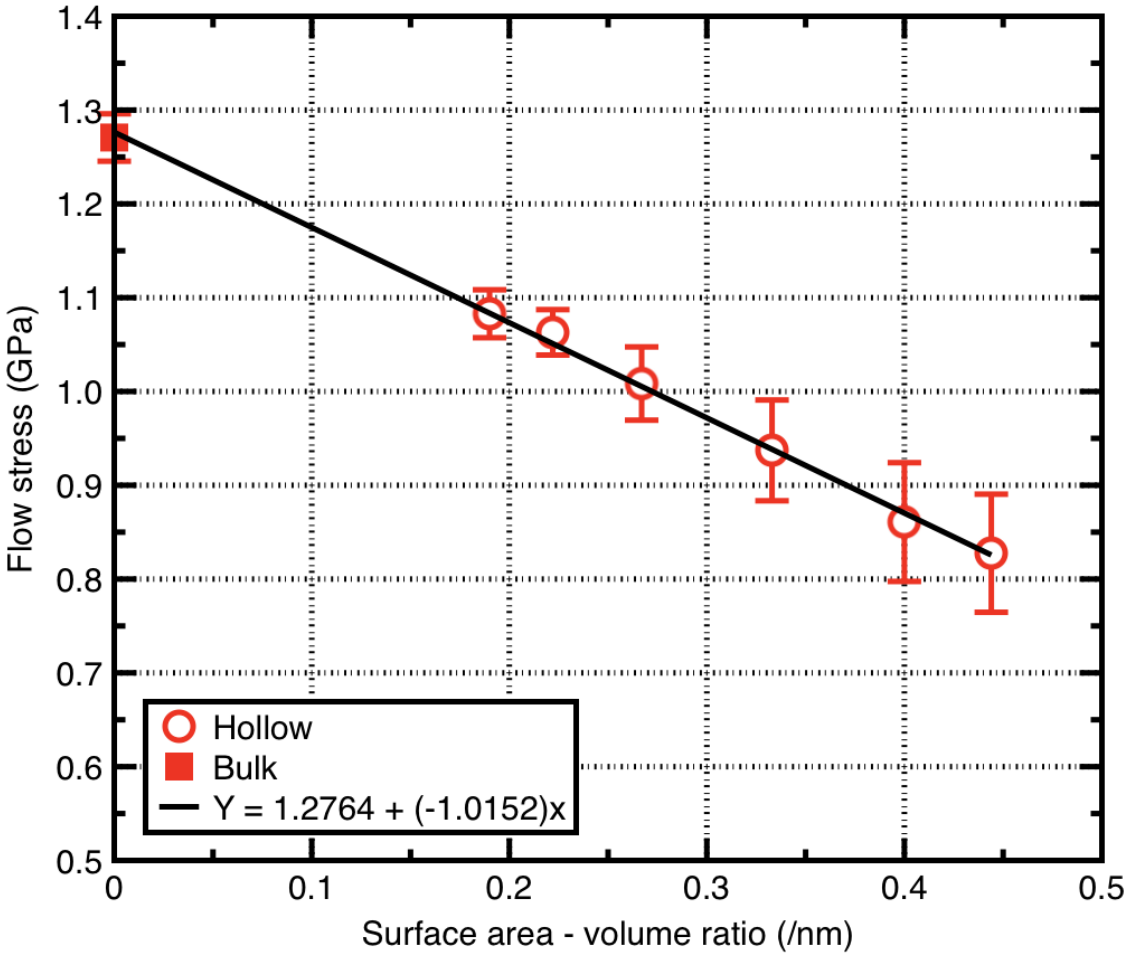

Figure 3.16: Plots of flow stress with respect to the surface area – volume ratio for the hollow pillar under compression (The flow stress is taken from the true stress between 5% strain and 20% strain and the error bar represents one standard deviation)

3.3.3 Results from tension tests

3.3.3.1 Stress-strain behavior

Tension test was carried on the solid core and hollow pillars with the same dimensions. All the conditions were kept same as the compression test, with only

deformation method changing from compression to tension. The stress-strain behavior of solid core pillars is shown in Figure 3.17. The elastic deformation parts for all the runs share the similar stress-strain behavior. However, the plastic deformation behavior varies in solid core pillars with different dimensions. Basically, these stress-strain curves can be divided into two parts. The solid core pillars with outer diameter of 30, 21, 18, 15 nm possess a smoother curve compared with the pillars with outer diameter of 12, 10, 9 nm. In particular, for the solid core pillar with inner diameter of 9 nm, the tensile stress first reaches to the highest point of around 1.7 GPa at 10% strain, and after that the stress decreases with the increase of strain. The average flow stress of the solid core pillar with 9nm outer diameter between 5% and 10% strain is 1.49 +/- 0.22 GPa and that between 5% and 20% strain is 1.31 +/- 0.22 GPa, which is about 18% drop.

Compared with the compression test, the tensile stress is higher. The solid core pillar with 30 nm outer diameter has the highest average flow stress of 1.15 +/- 0.02 GPa under compression, while under tension test, the pillar with the same dimension has the second lowest average flow stress of 1.21 +/- 0.03 GPa. Additionally, the size effect on the flow stress is more significant during compression test than tension test. As displayed in Figure 3.17, the stress-strain curves for the solid core pillar with 30, 21, 18 and 15 nm are similar to one another and the average flow stresses for them are 1.21 +/- 0.03 GPa, 1.24 +/- 0.04 GPa, 1.24 +/- 0.05 GPa and 1.27 +/- 0.06 GPa respectively, which are within 5% difference. The average Young's modulus (up to 0.2% strain) under tension test (57 GPa) is also higher than that under compression test (54 GPa). All these compression-tension

asymmetries for the solid core pillar are of great interest to investigate, which is related to their deformation mechanism.

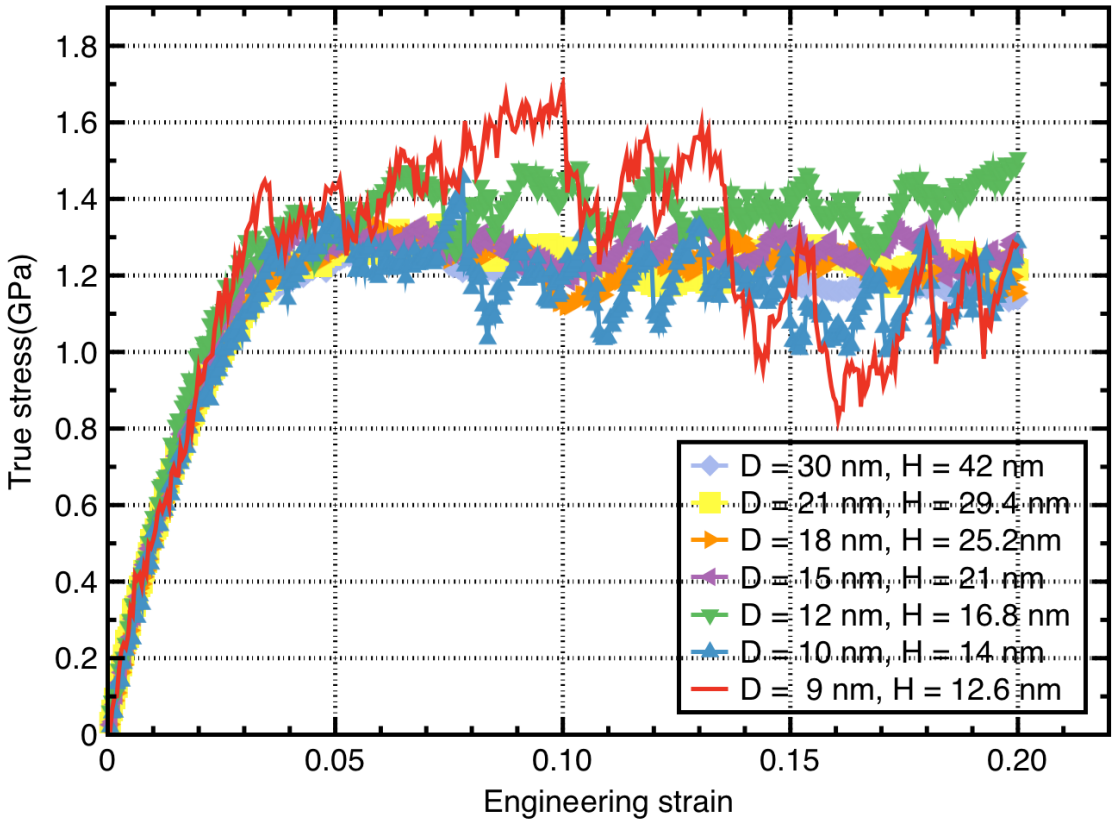

Figure 3.17: Plots of stress-strain curves of solid core shaped pillars with each color representing different dimensions (carried out under tension).

Figure 3.18 shows the stress-strain curves for hollow pillars with inner diameters of 9, 12, 15, 18, 20, and 21 nm under tension. Surprisingly, the stress-curves of these hollow pillars show no significant difference from one another and no size-dependent effect can be observed. The average flow stresses for hollow pillars with inner diameter of 9, 12, 15, 18, 20, and 21 nm are 1.22 +/- 0.02 GPa, 1.20 +/- 0.02 GPa, 1.21 +/- 0.02 GPa, 1.25 +/- 0.03 GPa, 1.26 +/- 0.03 GPa and 1.23 +/-

0.02 GPa respectively. These flow stress values are close to each other and within the range of 5% difference.

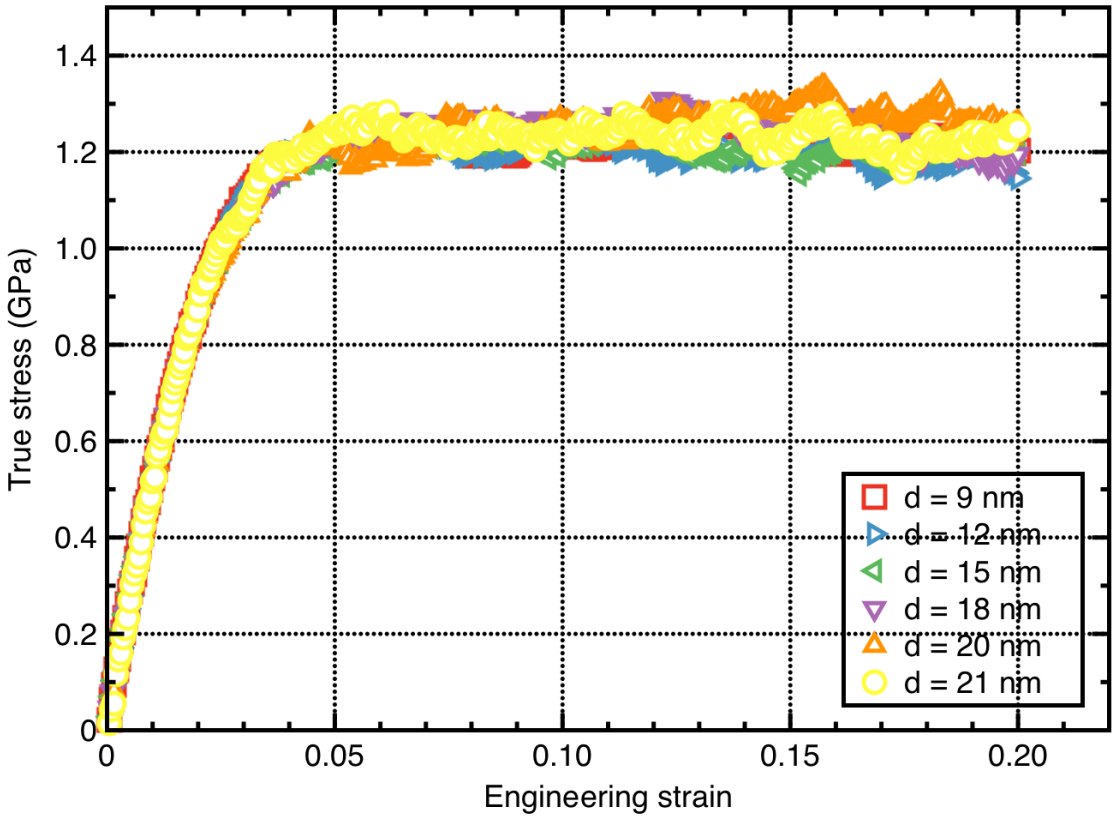

Figure 3.18: Plots of stress – strain curves of hollow pillars with each color representing different dimensions (carried out under tension).

As revealed in the previous section, hollow pillars with inner diameter of 21 nm, 20 nm, 18 nm and 15 nm show a gradual increase of stresses in the plasticity deformation regime, which show a hardening effect. However under tension tests, no hardening or softening effect can be observed for all the hollow pillars. In the compression test, the strength of the hollow pillar decreases with the increase of the size of the hole. This hole-size dependent behavior cannot be observed in the

tension test either. Additionally, hollow pillars are stronger under tension than under compression by comparing their average flow stress.

The compression-tension asymmetry for both the solid core and hollow pillar arises from their different deformation mechanism such defects nucleation and annihilation, grain boundary slipping, grain rotation etc. The free surface also plays a different roles under compression and tension [117]. The detailed explanation of this asymmetry will be discussed in the following sections.

3.3.3.2 Atomistic configuration

In order to explain the extraordinary stress-strain behavior of the structures under tension, the representative atomistic configurations of solid core pillars with outer diameter of 9 nm are displayed in Figure 3.19. As revealed in above, this pillar has a comparable dimension with the grain size, and roughly 3 grains can be observed in the structure. At the early stage of the tension (4% strain), the grain distribution does not change a lot, which can be observed by comparing Figure 3.19 (a) (4% strain under tension) with Figure 3.10 (a) (initial configuration). Twin boundaries emerge with more tensile deformation applied to the object. At 10% strain, no original grain can be observed in Figure 3.19 (b) and more defects are introduced into the structure. The portion of perfect lattice atoms (FCC atoms) is reduced from 77.8% to 71.6%, when the tensile strain increases from 4% to 10%, which implies that the defects are mostly nucleated inside a grain and from perfect lattice atoms. However, the portion of lattice atoms at 20% strain is 72.2%, which is almost unchanged compared with the state at 10% strain. I assume during this plasticity deformation period, no more defects are generated. For example, the rate

of the twinning and detwinning is equal to each other and a dynamic equilibrium can be reached. Additionally, the twin boundaries distance also changes during the plasticity process. As indicated in Figure 3.19 (c) (1) and Figure 3.19 (d) (1'), the distance of two twin boundaries is increased by around 6 atomic layers.

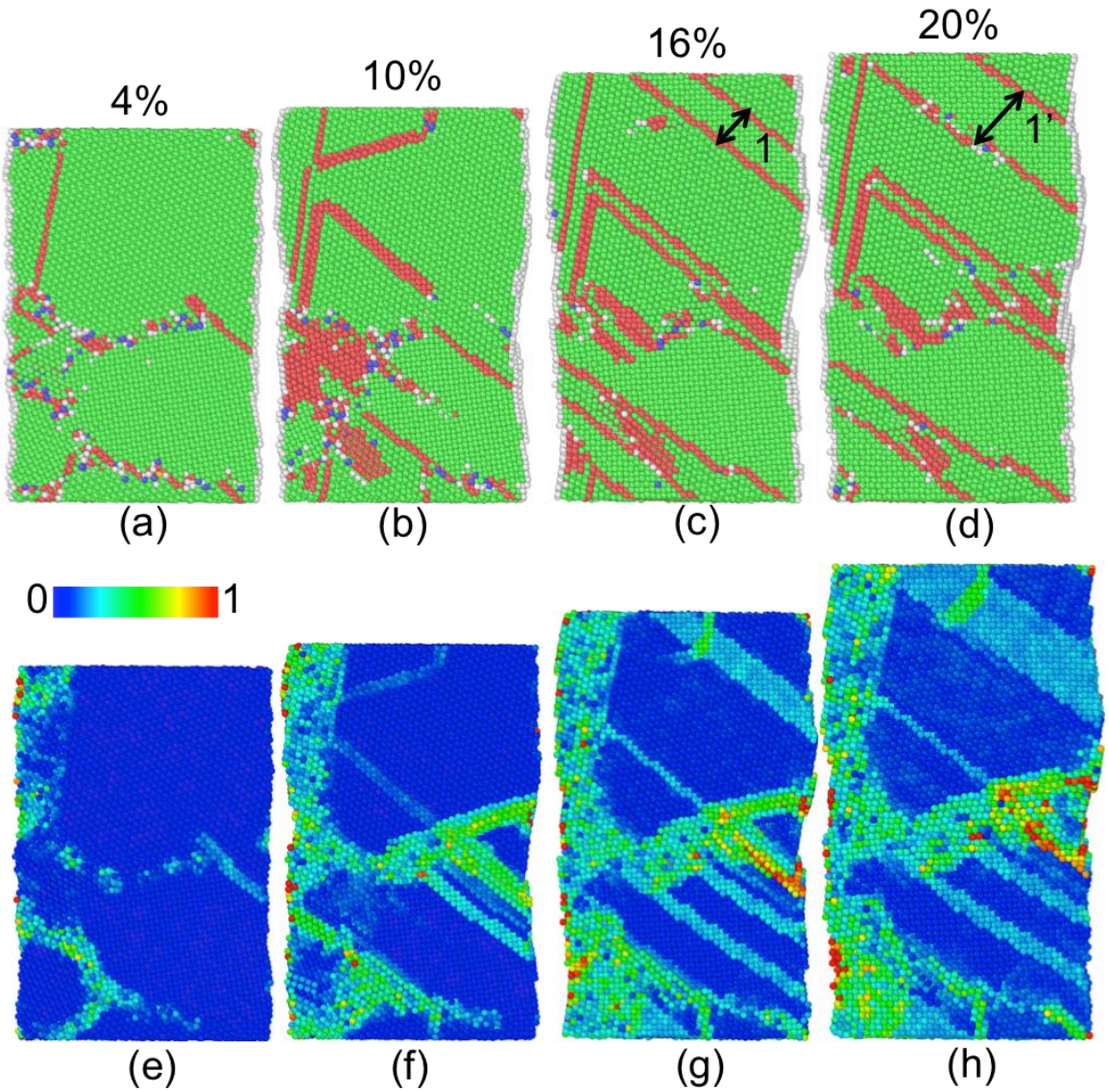

Figure 3.19: Representative snapshots of sliced solid core pillar with 9 nm outer diameter and 12.6 nm height under tension. (a)(b)(c)(d) Atomistic configurations at different strain (color coding based on the Ackland and Jones analysis). (e)(f)(g)(h) Local von Mise strain corresponding to each atomistic configuration with the reference state at the strain of 0 (color scheme based on the magnitude of strain with blue representing no strain and red representing the strain of 1).

It is interesting to notice that the atomistic configuration difference under compression and tension for the same solid core pillar with 9 nm outer diameter. After a compressive strain of 20%, the defects inside the pillar are reduced and approximate to a perfect single grain structure. However, after the 20% tensile strain, twin boundaries still exist inside the structure.

The local von Mise strain corresponding to each snapshot at different strain is also visualized with the reference state at 0% strain. Initially, the local atomistic strain accumulates around the boundary area as shown in Figure 3.19 (e). The grain boundary has a higher energy state and is not so stable at the tension deformation process, which undergoes most strain. With the strain going up, the generation of twin boundaries is also corresponding to a higher local von Mise strain, which accumulates at the twin boundaries. Furthermore, some atoms at the twin boundaries and around the surface have a local von Mise strain of 100%, which is much higher than the maximum overall strain of 20%.

The solid core pillar with outer diameter of 30 nm is carried out under tension test to reach a maximum strain of 100% to study the necking effect under tension. The stress-strain behavior and atomistic configurations are shown in figure 3.20. As displayed in the stress-strain curve (Figure 3.20 (f)), the plasticity can be basically divided into two parts: one is before 50% strain that maintains a relative stable flow stress; the other is before 50% that the stress drops with the increasing of the strain to around 0.6 GPa at 100% strain, which is almost half of the previous stress value. Additionally, the stress-strain curve at the second part is much rougher than that at the first part. This is corresponding to the stress-strain behavior in the

solid core pillar with small outer diameter (figure 3.17), since the diameter of solid core pillar will decrease with the elongation of the pillar for more deformation was applied.

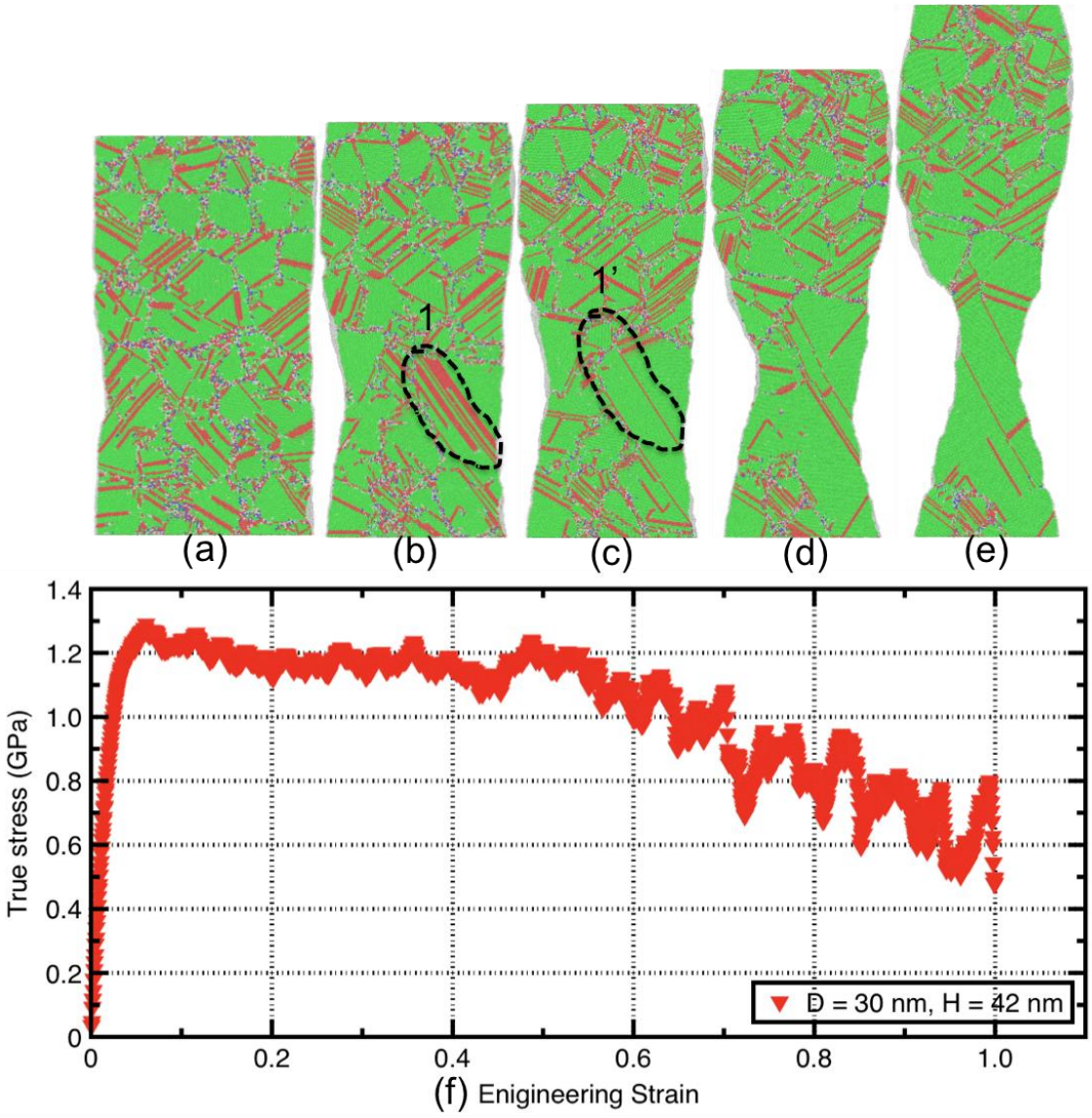

Figure 3.20: (a)(b)(c)(d)(e) Representative snapshots of atomistic configurations of sliced solid core pillar with a 30 nm outer diameter and 42 nm height at tensile strain of 20%, 40%, 50%, 70% and 100% respectively (color coding based on the Ackland and Jones analysis). (f) Plots of stress-strain curve of the solid core pillar under tension.

The necking of the solid core pillar with a 30 nm outer diameter can be observed from their atomistic configurations in Figure 3.20. There is no obvious necking at 20% strain (Figure 3.20 (a)). As shown in figure 3.20 (b), twin boundaries emerged at the necking area (dashed area 1), and with strain increasing to 50%, most of these twin boundaries disappeared (dashed area 1'). These massive twinning process can be regarded as a pre-indication of the necking and the detwinning will happen with more tensile strain carried out. The necking will become more and more severe with the increasing of tensile deformation. As indicated in Figure 3.20 (e), the diameter of the necking part at 100% strain is just around 9 nm, which is much smaller than the other parts. In addition, the defect density is smaller at the necking parts, since it is easier for the defect to annihilate at free surface around the necking area with a reduced diameter.

The atomistic configuration of hollow pillar with inner diameter of 21 nm under tension is shown in Figure 3.21. The wall thickness of this model is 4.5 nm, which is smaller than the grain size. As a result, no complete grain can be observed from Figure 3.21 (a) (the initial state of the tensile deformation process). At the early stage of deformation (0% – 2%), the grain and defect distribution almost stay the same. Twin boundaries were initiated from the boundary – free surface intersection, as revealed in Figure 3.21 (a) and (b) (dashed area 1 and 1'). With the tensile strain increased to 10%, the twin boundary (dashed area 1'' in Figure 3.21(c)) extended to the outer free surface forming twin boundaries across the wall of the hollow pillar. As mentioned above, the massive generation of the twin boundaries can be regarded as a pre-indication of the formation of the necking in solid core

pillars. The hollow pillar also experienced same necking mechanism. As we can see from the Figure 3.21 (c) (dashed area 2), lots of twinning accumulated in the mid part of the sidewall, which later becomes the site of necking process (Figure 3.21 (d)).

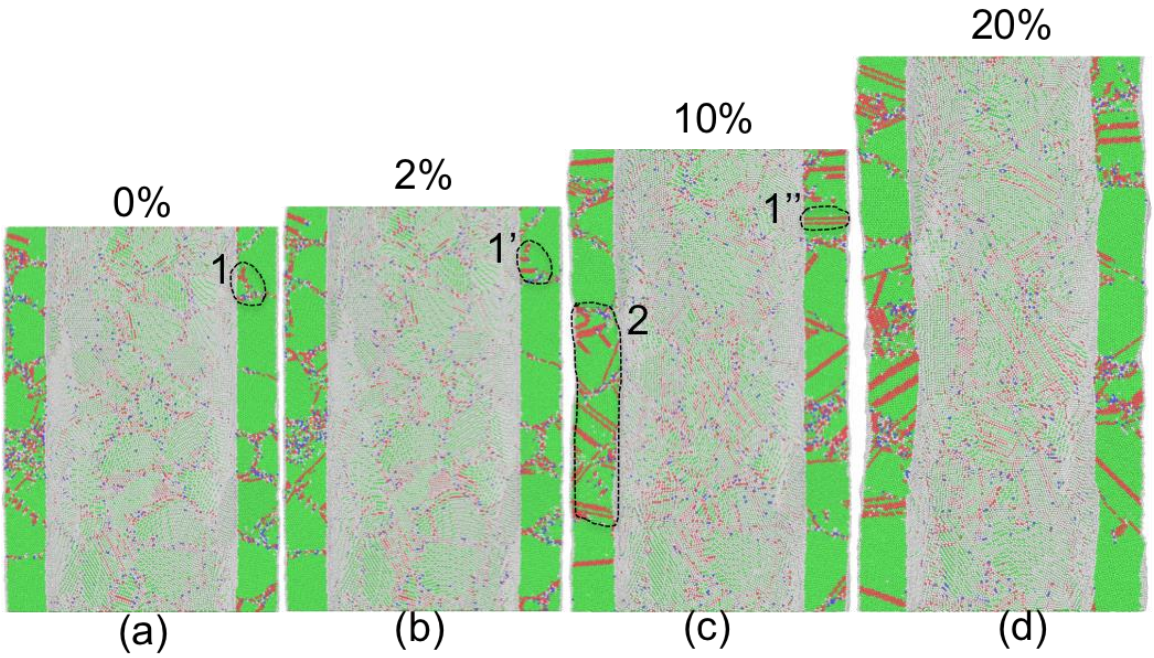

Figure 3.21: Representative snapshots of atomistic configuration of the sliced hollow pillar with outer diameter of 30 nm, inner diameter of 21 nm and height of 42 nm (color coding based on Ackland and Jones analysis)

3.3.3.3 Dislocation analysis

As shown in Figure 3.18, the stress-strain behavior of hollow pillars under tension is pretty similar to one another. As a result, it is interesting to investigate how the dislocation density evolves in these hollow pillars. Figure 3.22 shows the dislocation density evolution of hollow pillars under tensile deformation. The dislocation density is normalized by their initial dislocation density at the zero strain, which shares the same value as the corresponding hollow pillars with same

dimension under compressive deformation. The same dislocation extraction method was used to extract the dislocations and give the total length of the dislocation, which was described above.

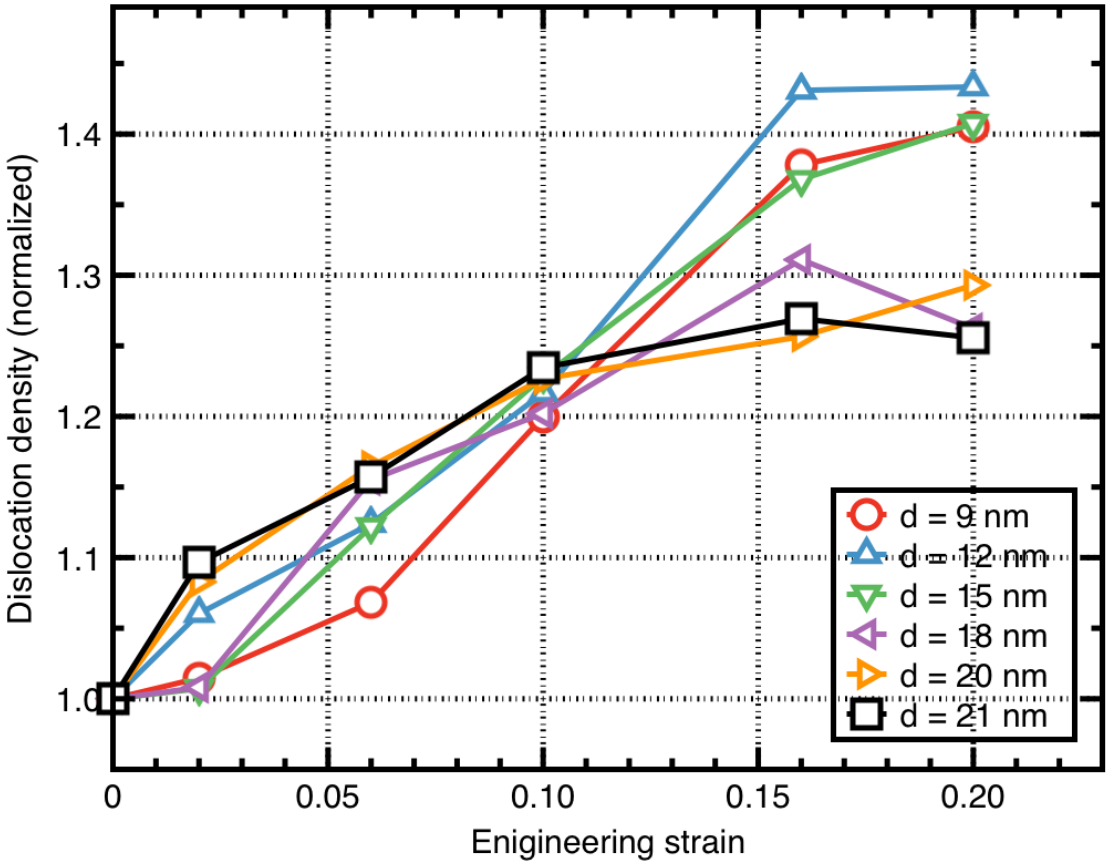

Figure 3.22: Plots of dislocation density with the engineering strain of the hollow pillar under tensile deformation (The dislocation density is normalized by its initial state).

Generally, the dislocation density maintains the increasing trend with the strain going up. No obvious dislocation density drop can be observed. It is interesting to notice that, at the strain of around 10%, the dislocation density of all the models comes to around 1.2 times of their initial value and the difference between them is smaller than 0.03. Between 10% strain and 16% strain, a steady increase of dislocation density can be seen from Figure 3.22. The hollow pillar with

inner diameter of 21 nm and 18 nm experiences a minor dislocation density drop from 16% strain to 20% strain. The final dislocation density (20% strain) of the hollow pillar with inner diameter 21 nm (3.36×10^{17} m^{-2}) is smaller than that with inner diameter of 9 nm (4.28×10^{17} m^{-2}), since more free surface exists in the hollow pillar with larger inner diameter and the dislocation becomes easier to annihilate at the free surface.

3.3.3.4 Free surface effects

Free surface effects under tensile deformation are presented by plotting the flow stress versus free surface area – volume ration. Figure 3.23 shows the relationship between the flow stress and surface area to volume ratio of the solid core pillar under tension. The average flow stress is taken from 5% to 20% strain. Each surface area to volume ration is corresponding to a certain pillar with specific dimensions as mentioned above. The bulk sample resembles the objects with no free surface.

Generally, the average flow stress of the solid core pillars is higher than that of the samples without free surface, which suggests the free surface enhances the strength of solid core pillars. The large standard deviation of solid core pillar with a 9 nm outer diameter is caused by the fluctuated stress-strain curve. In the compressive deformation, the average flow stress of the solid core pillars with all the different dimensions are lower than their bulk counterparts, which implies the free surface plays a totally different role during the compressive and tensile deformation process (compression-tension asymmetry will be discussed in the following session). The average flow stress for solid core pillars with outer diameter

of 10 nm is lower than other solid core pillars, and no numeric relationship between the average stress and the dimension of the solid core pillars can be established.

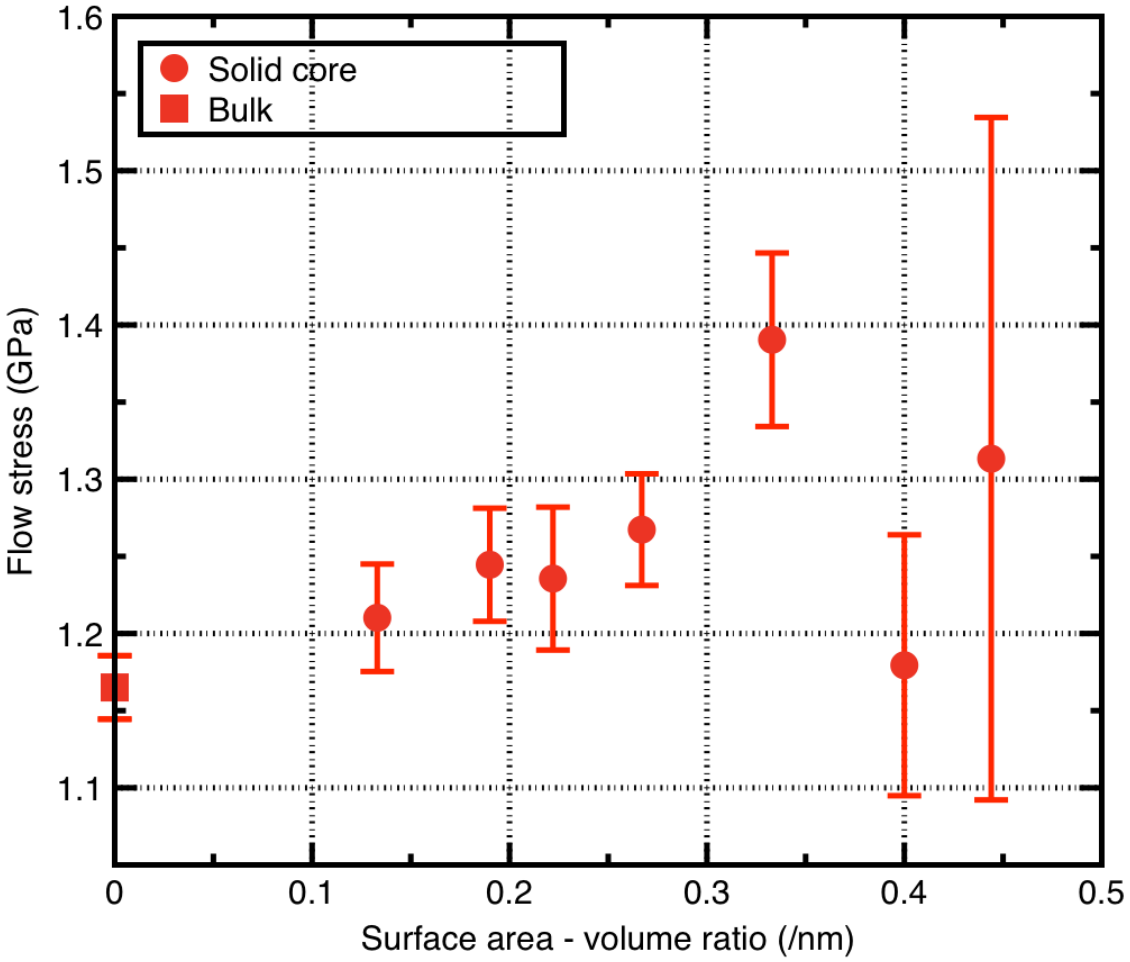

Figure 3.23: Plots of flow stress with respect to the surface volume ration for the solid core pillar under tension (The flow stress is taken from the average true flow stress between 5% and 20% strain and the error bar represents one standard deviation)

Figure 3.24 shows the average flow stress versus surface area – volume ration of the hollow pillars. The average tensile flow stresses of the hollow pillar with inner diameters of 9, 12, 15, 18, 20, 21 nm are 1.22 +/- 0.02, 1.20 +/- 0.02, 1.21 +/- 0.02, 1.25 +/- 0.03, 1.26 +/- 0.03, 1.23 +/- 0.02 GPa respectively. The differences between these flow stress values are smaller than 5%, which is much less than that

of the hollow pillars under compressive deformation. The average flow stress of the bulk sample under tension is 1.17 +/- 0.02 GPa, which is also less than the average flow stress of the hollow pillars.

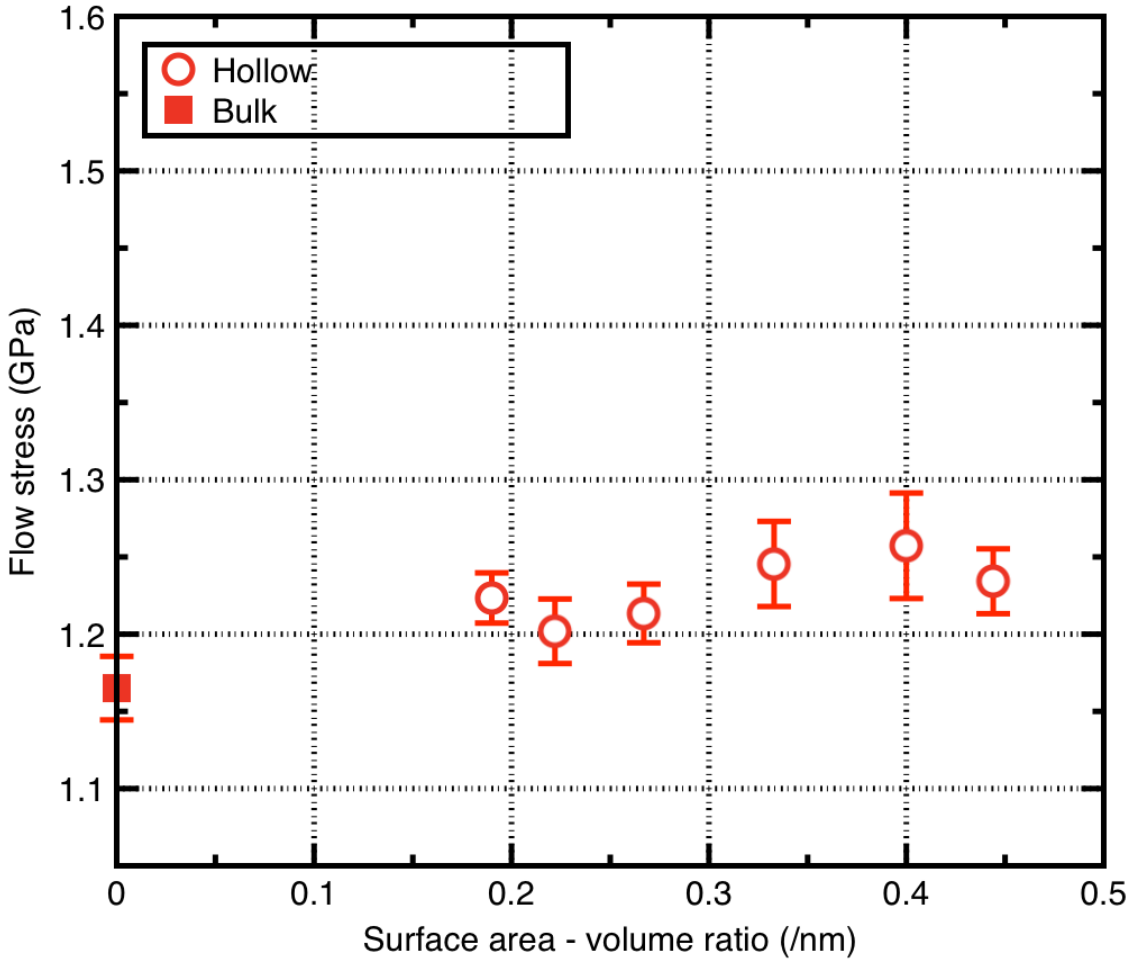

Figure 3.24: Plots of flow stress with respect to the surface volume ration for the solid core pillar under tension (The flow stress is taken from the average true flow stress between 5% and 20% strain and the error bar represents one standard deviation)

The average tensile stresses of the hollow pillar are less than that of the solid core pillars except the one with surface area – volume ratio of 0.4 nm^{-1}, which is corresponding to the hollow pillar with the inner diameter of 10 nm. This even flow stress of hollow pillars under tensile compression is also different from compressive

deformation, under which the flow stress decreases with the increasing of the surface area – volume ratio.

3.3.4 Compression-tension asymmetry

Diao et al. [117] found a yield strength compression-tension asymmetry in the gold nanowires. They carried out MD simulation on the single crystal gold nanowires using the EAM potential. Their results showed that this asymmetry effect also depended on the plane of nanowires. The magnitude of tensile yield stress is much larger than that of the compressive yield stress for small [1 0 0] nanowires. While for small [1 1 1] nanowires, tensile and compressive yield stresses had similar magnitudes. Monk et al. [106] observed a significant compression-tension asymmetry in the nano-crystalline nickel, which also depended on the size of nanowire. This asymmetry effect decreased as the wire radius decreased and was reserved for the smallest wire tested in their MD simulation.

This phenomenal compression-tension asymmetry is also profound in my copper MD simulations. As show in Figure 3.8 and Figure 3.18, the stress-strain behavior of the hollow pillar is different under the compression and tension. For the hollow pillar under compression, the effects of the hole size inside the pillar can be easily observed under compression with larger hole size meaning a softer objects. For the hollow pillar under tension, no hole size effects can be observed, showing similar stress-train curves for the varying hole sizes inside the hollow pillars.

Figure 3.25 shows the Young's modulus with respect to the solid core and hollow pillar with different surface-volume ratio. Theoretically, the Young's modulus should be the same for all modules regardless of the different shapes of the

pillars. My results show the Young's modulus is within the range of 45 GPa to 65 GPa. There is no clear tendency can be observed that the pillars with certain dimensions attain a higher Young's modulus. However, overall the pillar maintain a higher Young's modulus under tension than compression.

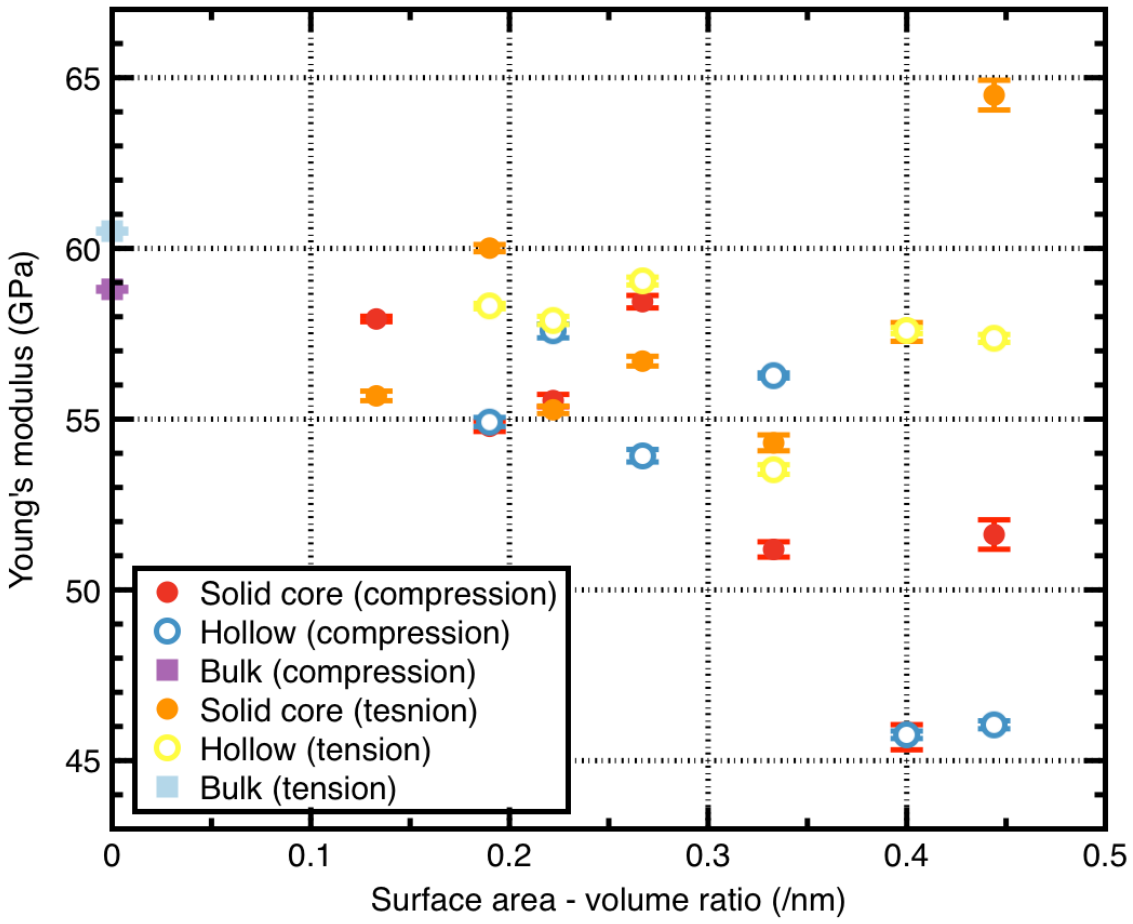

Figure 3.25: Plots of Young's modulus with respect to different surface area – volume ratio under compressive and tensile deformation. (error bar represents one standard deviation)

Figure 3.26 summaries the average flow stress under both compression and tension. For the bulk sample, the flow stress under compression and tension are 1.27 +/- 0.03 and 1.16 +/- 0.02 GPa respectively, which shows a compression-tension flow stress asymmetry ration of 1.09 with compressive flow stress higher

than tensile flow stress. This asymmetry has also been observed experimentally by Schuster et al. [76] in nano-crystalline nickel. Since the bulk sample possesses all periodic boundary condition, no free surface exists at its all three direction. The nano-scale grain size and the corresponding deformation mechanism of grain boundary sliding are the only effects in these bulk samples. As a result, this compression-tension asymmetry can be explained by the fact that grain boundary sliding is more difficult under compression than tension, which implies that more dislocation activity is expected under compression if the same amount of deformation is imposed. This dislocation activity variation can be validated by the higher dislocation density (20% strain) of the bulk sample under compression (5.15×10^{17} m^{-2}) than tension (4.74×10^{17} m^{-2}).

In nano-crystalline pillars, free surface exists along their lateral directions, which also accounts for the compression-tension asymmetry in addition to the grain boundary sliding and dislocation activity. The surface stress exists on the free surface of the pillar structure and the effect of the surface stress can be appreciated by examining the magnitude of the intrinsic compressive stress in the interior of the pillar structures induced by the surface stress [117]. Additionally, the applied external forces and the intrinsic compressive forces behave differently under compression and tension. Under compression, these two contributions have same compressive effects, which means less external force is needed to perform the deformation. The Larger surface area-volume ration means higher surface stress induced intrinsic compressive stress and smaller external force is necessary to carry out the deformation, showing a softening effect. For the plasticity under tension, this

surface stress induced compressive stress is opposite to the external tensile forces. The applied external stress must first overcome this compressive stress and then carry out the tensile deformation. Therefore, the larger the surface area-volume ratio means the higher stress is needed to make deformation. This effect partially explains the compression-tension asymmetry with a tensile stress higher than the compressive stress and also the surface effects under tension and compression.

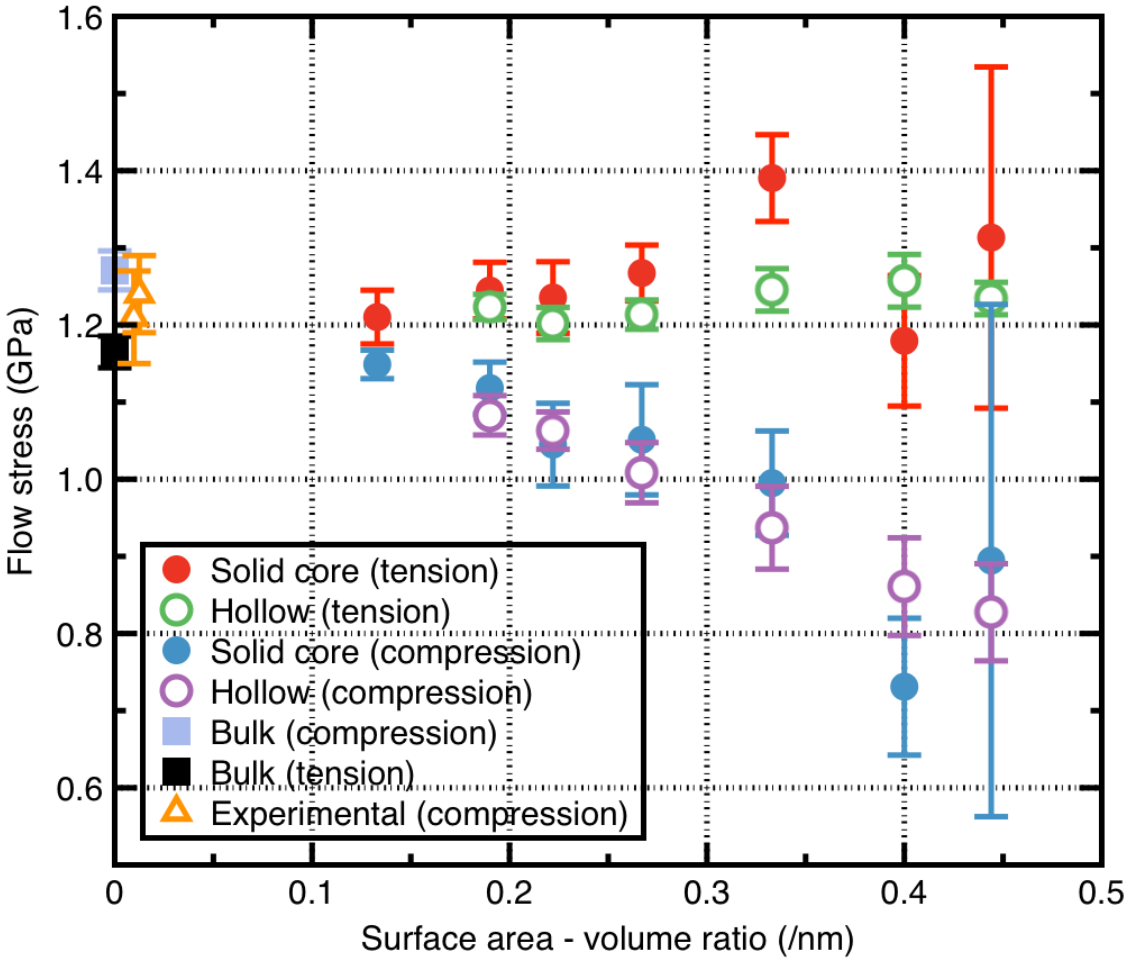

Figure 3.26: Plots of flow stress with respect to the surface-volume ration (The flow stress is taken from the average true flow stress between 5% and 20% strain, the error bar represents one standard deviation, the experimental data is taken from solid core and hollow pillar with small grain size)

As mentioned above, the grain boundary sliding also plays a role in the compression-tension asymmetry. Basically, the deformation behavior of the pillars can be regarded as combination of these two compression-tension asymmetry mechanisms. One is due to the surface stress and the other is due to the nano-scale sizes of the grain and the corresponding deformation mechanism of grain boundary sliding. At the nano-scale dimension objects, the surface area-volume ratio is much higher than bulk scale, and the surface stress effect dominates.

The experimental compression data was also put into figure 3.26. The surface area-volume ration of the solid core and hollow pillar with small grain are around 0.01 /nm, which is much less than the models in the MD simulations. The average flow stress for the experimental shares the similar value as the bulk sample under compression.

3.3.5 Grain size effect

MD simulation was also performed to study the grain size effect on the mechanical properties of the copper pillars. The same technique was applied to build the model with large grain size of 13 nm. This Voronoi tessellation method has largely been applied to build the simulation models and is believe to assign random orientation of grains. Figure 3.26 (a) illustrates the grain distribution inside the solid core sample with grain size of 13 nm. Compared with the solid core pillar with grain size of 6 nm (Figure 3.26 (b)), it is obvious that lattice atoms occupied more percentage of space in the sample with larger grain size. The copper pillar with reduced diameter of 15 nm was constructed by cutting it from the larger-dimensional pillar. Since the grain size is 13 nm, no pillar with outer diameter less

than 15 nm was built. The simulation process was the same as what has been applied to the pillar with grain size of 6 nm. The pillar was deformed at a compressive strain rate of $10^8\ s^{-1}$. The maximum engineering strain of 20% was achieved by deforming the simulation box under canonical ensemble (NPT) for 400,000 steps. The time step was fixed at 5 picoseconds, which is believed to produce reliable results.

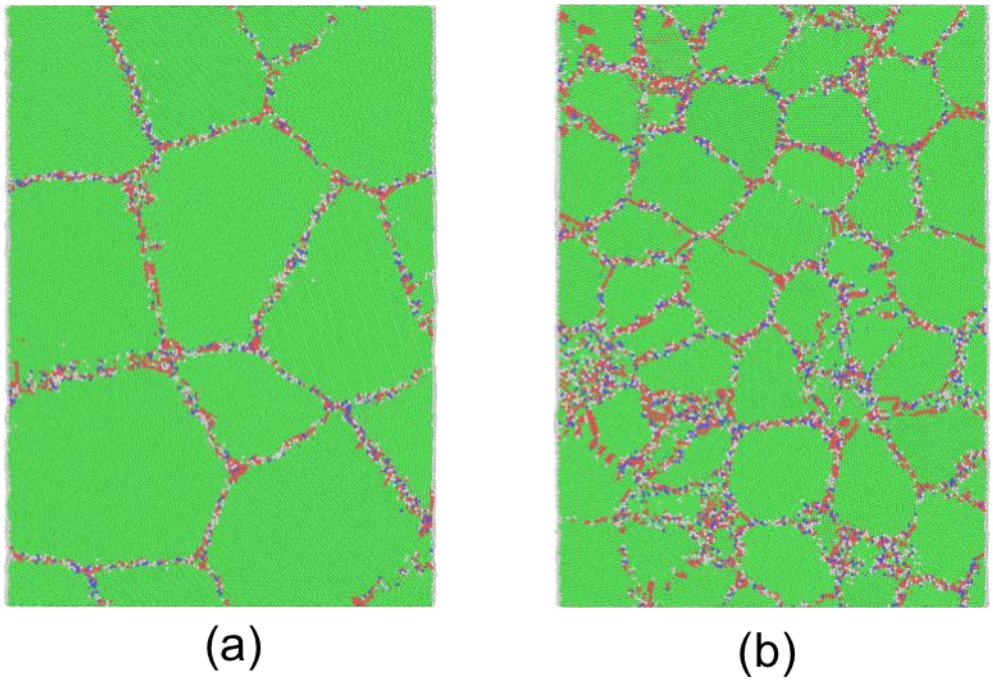

Figure 3.27 Representative atomistic snapshots of sliced solid core pillar with 30 nm in outer diameter and 42 nm in height. (a) Grain size of 13 nm. (b) Grain size of 6 nm. (color coding based on Ackland and Jones analysis)

As displayed in Figure 3.27, the slope of elastic deformation part of large-grain pillars are steeper than that of the small-grain pillar, which implies a higher Young's modulus in the large-grain specimens. To validate this hypothesis, Young's modulus was calculated accurately between the strain regions of 0% to 0.2%. The Young's modulus of solid core pillar with grain size of 13 nm is 71 GPa, which is

about 25% higher than that of solid core pillar with grain size of 6 nm (57GPa). This grain size effect on the Young's modulus has also been observed by Zhou et al. [100], and Nan et al. [118] has proposed a linear relationship between Young's modulus and the reciprocal of mean grain size with the grain size range of 2.6 to 53.1 nm. This effect is rarely reported by the actual experiments, since the broad range of grain distribution can weaken or even eliminate the grain size effects.

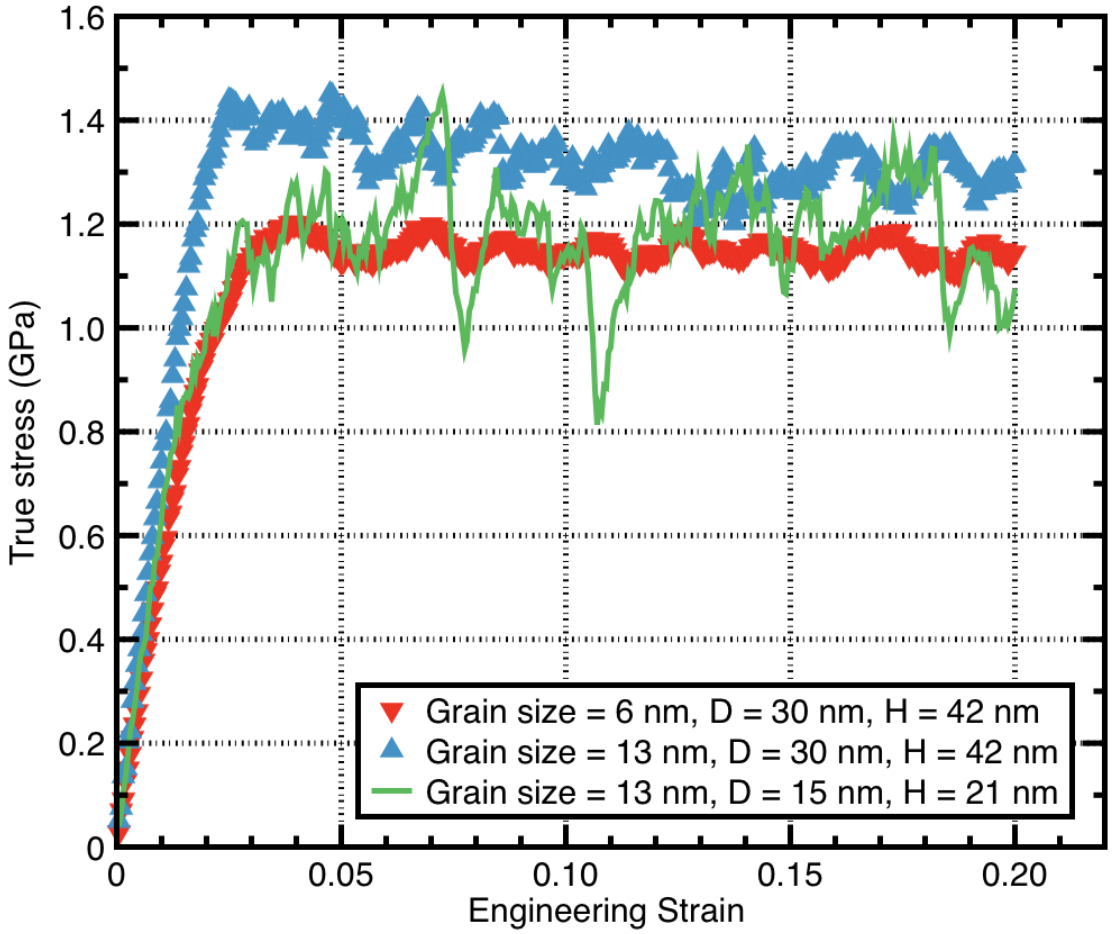

Figure 3.28: Plots of stress-strain curves with each color representing different grain size and dimensions.

From the stress-strain curves in figure 3.27, it is obvious that the solid core pillar with large grain size has a higher strength than the small grain size. The

average flow stresses of the large-grain and small-grain pillars are 1.31 +/- 0.04 and 1.15 +/- 0.02 GPa respectively. This inversed Hall-Petch effect is also corresponding to the experimental data we found. Additionally, for the large-grain pillar, a softening effect can be observed with the strain increasing. The stress-strain curve of the large-grain pillar with a 15 nm outer diameter and 21 nm height is serrated. This phenomenon adds to the evidence that when the grain size approaches the dimension of the objects, the plasticity process will undergo a serrated stress-strain curve.

Chapter 4 : Conclusions

This thesis has dealt with the mechanical properties of copper pillars through both experimental methods and MD simulations. EBL and electroplating were used to fabricate the copper pillars. These as-fabricated novel pillars with four different cross-sectional geometries, solid core, hollow, c-shaped, and x-shaped, were then deformed using micro-compression testing. Three different grain sizes were achieved by changing the compositions of plating solution during the electroplating process. Results show that the strength of the copper pillar with the same grain size was not affected by the cross-sectional geometries. Additionally, classical Hall-Petch like grain boundary strengthening mechanisms were observed between the large-grain specimens to medium-grain specimens. An inversed Hall-Petch relationship emerged as the grain size continues to go down to the small grain size region. Solid core pillars with three different grain sizes were also compressed under cyclic deformation. Results show a slightly reduced strength compared with the designated solid core pillars with the same grain size.

MD simulation was carried out using the LAMMPS codes. The copper columnar structures with the grain size of 6 nm were constructed using Voronoi tessellation method. The deformation was conducted under both compression and tension with a strain rate of 10^8 s^{-1}. A compreesion-tension asymmetry was observed by assessing the average stresses of the copper pillar with different dimensions. Results show that the strength of the nano-crystalline pillars is higher under tension than compression. In addition to the grain boundary sliding and dislocation activity, the free surface also accounts for this compression-tension

asymmetry. The free surface energy existing at the free surface has a positive effect under compression (smaller external force) and a negative effect under tension (larger external force). By extending the grain size of the copper pillar to 13 nm, the grain size effect has also been observed, and exhibited an inversed Hall-Petch relationship from grain sizes of 13 nm to 6 nm.

Some improvements can be made to this research. The dimension of the specimens in the experiments is at the 500 nm outer diameter, while the largest dimension in the MD simulation is only 30 nm outer diameter. There is a large gap of specimen dimension exiting between the experimental and MD simulation. If more computation resources are available, larger models will be constructed and tested to close this gap!

Appendices

Appendix A: Results of copper pillars under experimental compression tests

Batch	Cross-sectional geometries	Outer diameter (nm)	Wall thickness (nm)	Flow stress (GPa)	Flow stress under cyclic deformation (GPa)
Large grain	Solid Core	551+/-7	N/A	0.71+/-0.05	0.68+/-0.06
	Hollow	571+/-9	150+/-11	0.75+/-0.05	N/A
	X-shaped	508+/-11	N/A	0.65+/-0.06	N/A
	C-shaped	551+/-8	187+/-9	0.72+/-0.05	N/A
Medium grain	Solid core	561+/-9	N/A	1.26+/-0.03	1.14+/-0.08
	Hollow	576+/-7	158+/-7	1.23+/-0.04	N/A
	X-shaped	521+/-10	N/A	1.21+/-0.03	N/A
	C-shaped	558+/-6	205+/-9	1.23+/-0.03	N/A
Small grain	Solid core	564+/-7	N/A	1.21+/-0.06	1.15+/-0.05
	Hollow	577+/-9	166+/-10	1.24+/-0.05	N/A
	X-shaped	483+/-14	N/A	1.14+/-0.04	N/A
	C-shaped	553+/-10	198+/-7	1.21+/-0.03	N/A

The flow stress is taken from 5% strain to 20% strain. Error bar stands for one standard deviation.

Appendix B: Results of copper pillar mechanical tests with MD simulation

Shape	Outer diameter (nm)	Inner Diameter (nm)	Height (nm)	Grain size (nm)	Young's Modulus (GPa)	Area-volume ratio (/nm)	Flow stress (GPa)
Compression							
Solid core	30	N/A	42	6	57.93+/-0.08	0.133	1.15+/-0.02
Solid core	21	N/A	29.4	6	54.79+/-0.15	0.19	1.12+/-0.03
Solid core	18	N/A	25.2	6	55.54+/-0.18	0.222	1.04+/-0.05
Solid core	15	N/A	21	6	58.44+/-0.18	0.267	1.05+/-0.07
Solid core	12	N/A	16.8	6	51.18+/-0.22	0.333	0.99+/-0.07
Solid core	10	N/A	14	6	45.68+/-0.37	0.4	0.73+/-0.09
Solid core	9	N/A	12.6	6	51.62+/-0.43	0.444	0.89+/-0.33
Solid core	30	N/A	42	13	70.92+/-0.16	0.133	1.31+/-0.04
Solid Core	15	N/A	21	13	70.09+/-0.15	0.267	1.18+/-0.10
Hollow	30	9	42	6	54.92+/-0.13	0.19	1.08+/-0.03
Hollow	30	12	42	6	57.58+/-0.20	0.222	1.06+/-0.02
Hollow	30	15	42	6	53.93+/-0.18	0.267	1.01+/-0.04
Hollow	30	18	42	6	56.28+/-0.07	0.333	0.94+/-0.05
Hollow	30	20	42	6	45.76+/-0.11	0.4	0.86+/-0.06
Hollow	30	21	42	6	46.05+/-0.12	0.444	0.83+/-0.06
Rectangular	30x30		42	6	58.80+/-0.05	0	1.27+/-0.03
Tension							
Solid core	30	N/A	42	6	55.68+/-0.14	0.133	1.21+/-0.03
Solid core	21	N/A	29.4	6	60.01+/-0.11	0.19	1.24+/-0.04
Solid core	18	N/A	25.2	6	55.27+/-0.11	0.222	1.24+/-0.05
Solid core	15	N/A	21	6	56.70+/-0.14	0.267	1.27+/-0.04
Solid core	12	N/A	16.8	6	54.31+/-0.23	0.333	1.39+/-0.06
Solid core	10	N/A	14	6	57.55+/-0.27	0.4	1.18+/-0.08
Solid core	9	N/A	12.6	6	64.50+/-0.44	0.444	1.31+/-0.22
Hollow	30	9	42	6	58.31+/-0.08	0.19	1.22+/-0.02
Hollow	30	12	42	6	57.90+/-0.12	0.222	1.20+/-0.02
Hollow	30	15	42	6	59.04+/-0.11	0.267	1.21+/-0.02
Hollow	30	18	42	6	53.52+/-0.14	0.333	1.25+/-0.03
Hollow	30	20	42	6	57.59+/-0.09	0.4	1.26+/-0.03
Hollow	30	21	42	6	57.36+/-0.12	0.444	1.23+/-0.02
Rectangular	30x30		42	6	60.51+/-0.06	0	1.17+/-0.02

The flow strain is taken from 5% to 20% strain. Young's modulus is taken from 0% to 0.3% strain. Error stands for one standard deviation.

Appendix C: Raw compressive stress-strain data of solid core pillar with 30 nm outer diameter under compression

strain	stress	0.019	0.924722764	0.038	1.184989678
0.0005	0.028130148	0.0195	0.937778556	0.0385	1.200969967
0.001	0.070374654	0.02	0.959299488	0.039	1.202577437
0.0015	0.091611762	0.0205	0.962947971	0.0395	1.19648377
0.002	0.127127245	0.021	0.977026607	0.04	1.200500125
0.0025	0.150624939	0.0215	0.977116412	0.0405	1.197773467
0.003	0.179115842	0.022	0.997955612	0.041	1.202102116
0.0035	0.209625157	0.0225	1.003138907	0.0415	1.192385327
0.004	0.235700295	0.023	1.014593691	0.042	1.188799579
0.0045	0.261111969	0.0235	1.016741674	0.0425	1.189513789
0.005	0.29513415	0.024	1.035668012	0.043	1.1771528
0.0055	0.324004804	0.0245	1.033166476	0.0435	1.178577885
0.006	0.358528908	0.025	1.053483659	0.044	1.176810824
0.0065	0.379577091	0.0255	1.055392199	0.0445	1.170341397
0.007	0.400767432	0.026	1.076451387	0.045	1.183681666
0.0075	0.428359629	0.0265	1.07818337	0.0455	1.171217699
0.008	0.457601554	0.027	1.099655214	0.046	1.177210996
0.0085	0.487210694	0.0275	1.10261177	0.0465	1.169771522
0.009	0.497649057	0.028	1.116286406	0.047	1.166096341
0.0095	0.530433991	0.0285	1.121086483	0.0475	1.155945122
0.01	0.549041762	0.029	1.13012426	0.048	1.14737969
0.0105	0.580414487	0.0295	1.12790906	0.0485	1.140387535
0.011	0.594855281	0.03	1.140810724	0.049	1.138705056
0.0115	0.632010673	0.0305	1.13971467	0.0495	1.141309584
0.012	0.644067821	0.031	1.154792224	0.05	1.126023168
0.0125	0.670130001	0.0315	1.1615149	0.0505	1.129012676
0.013	0.68346655	0.032	1.164186733	0.051	1.141530234
0.0135	0.716338566	0.0325	1.156531729	0.0515	1.144702393
0.014	0.732448666	0.033	1.174870196	0.052	1.148387113
0.0145	0.761085669	0.0335	1.16644467	0.0525	1.134169135
0.015	0.778431843	0.034	1.169860258	0.053	1.126119922
0.0155	0.800450323	0.0345	1.167657564	0.0535	1.129772724
0.016	0.814818482	0.035	1.179123612	0.054	1.135122987
0.0165	0.840961496	0.0355	1.173652665	0.0545	1.134229662
0.017	0.855103458	0.036	1.189312734	0.055	1.136691368
0.0175	0.876447659	0.0365	1.194700165	0.0555	1.130249366
0.018	0.890181521	0.037	1.193164455	0.056	1.132192778
0.0185	0.917124638	0.0375	1.192328648	0.0565	1.12861949

0.057	1.122710098	0.0785	1.132552389	0.1	1.14873171
0.0575	1.133915658	0.079	1.131978777	0.1005	1.142612154
0.058	1.137815559	0.0795	1.126288516	0.101	1.145965516
0.0585	1.147656525	0.08	1.141472102	0.1015	1.139969338
0.059	1.135837763	0.0805	1.148896645	0.102	1.147732152
0.0595	1.141835053	0.081	1.152359116	0.1025	1.138143642
0.06	1.138527606	0.0815	1.142922811	0.103	1.138650199
0.0605	1.149942602	0.082	1.146220679	0.1035	1.150095228
0.061	1.144201897	0.0825	1.149750151	0.104	1.152419875
0.0615	1.151167912	0.083	1.161368884	0.1045	1.160106638
0.062	1.158280404	0.0835	1.157598375	0.105	1.157778701
0.0625	1.147090898	0.084	1.161046579	0.1055	1.159753546
0.063	1.15176733	0.0845	1.165457021	0.106	1.171153396
0.0635	1.154774465	0.085	1.163608587	0.1065	1.163209495
0.064	1.154844376	0.0855	1.168407042	0.107	1.166589605
0.0645	1.152655478	0.086	1.171944043	0.1075	1.16225635
0.065	1.164166071	0.0865	1.173465836	0.108	1.165069106
0.0655	1.171883401	0.087	1.167471442	0.1085	1.162015565
0.066	1.179199937	0.0875	1.158250779	0.109	1.158530176
0.0665	1.193003048	0.088	1.15099586	0.1095	1.169488463
0.067	1.179542352	0.0885	1.141070234	0.11	1.157494123
0.0675	1.182391429	0.089	1.154480705	0.1105	1.159855749
0.068	1.172413246	0.0895	1.146815821	0.111	1.149141229
0.0685	1.184593593	0.09	1.150413469	0.1115	1.137739346
0.069	1.186894317	0.0905	1.142705035	0.112	1.129201168
0.0695	1.192096542	0.091	1.146715241	0.1125	1.119092221
0.07	1.199399446	0.0915	1.159639428	0.113	1.115182043
0.0705	1.193946121	0.092	1.145367684	0.1135	1.117495127
0.071	1.184548132	0.0925	1.144773371	0.114	1.114989646
0.0715	1.191690635	0.093	1.146434741	0.1145	1.124046883
0.072	1.180657801	0.0935	1.150298575	0.115	1.127732176
0.0725	1.176560987	0.094	1.135455857	0.1155	1.132292627
0.073	1.160652732	0.0945	1.133820949	0.116	1.133180664
0.0735	1.168321474	0.095	1.140247317	0.1165	1.123785537
0.074	1.155468014	0.0955	1.137668047	0.117	1.139858893
0.0745	1.161631649	0.096	1.12244857	0.1175	1.146304475
0.075	1.157527591	0.0965	1.144090519	0.118	1.138496116
0.0755	1.158365053	0.097	1.141731133	0.1185	1.131824962
0.076	1.141925799	0.0975	1.145998569	0.119	1.131001242
0.0765	1.143121605	0.098	1.139655262	0.1195	1.132741594
0.077	1.128239864	0.0985	1.138566691	0.12	1.12928575
0.0775	1.1222133	0.099	1.138496111	0.1205	1.137320348
0.078	1.125867412	0.0995	1.13669417	0.121	1.145555297

0.1215	1.143107321	0.143	1.16775396	0.1645	1.169364095
0.122	1.145699987	0.1435	1.168117277	0.165	1.1626782
0.1225	1.144711093	0.144	1.167429081	0.1655	1.170278248
0.123	1.158173815	0.1445	1.166330278	0.166	1.163343902
0.1235	1.165436732	0.145	1.163178509	0.1665	1.167936978
0.124	1.172149236	0.1455	1.159667502	0.167	1.164584373
0.1245	1.175745922	0.146	1.163898491	0.1675	1.156281631
0.125	1.181292845	0.1465	1.162972915	0.168	1.165360619
0.1255	1.186809196	0.147	1.156427866	0.1685	1.1736163
0.126	1.180828021	0.1475	1.148934356	0.169	1.175901631
0.1265	1.18437719	0.148	1.150181775	0.1695	1.176987504
0.127	1.180723321	0.1485	1.148317091	0.17	1.180596487
0.1275	1.17850011	0.149	1.149013531	0.1705	1.177165741
0.128	1.190476715	0.1495	1.157699759	0.171	1.172743662
0.1285	1.172583392	0.15	1.150929344	0.1715	1.184091412
0.129	1.175531389	0.1505	1.159865641	0.172	1.175268136
0.1295	1.155564137	0.151	1.147167651	0.1725	1.176759316
0.13	1.152946716	0.1515	1.153923906	0.173	1.176267643
0.1305	1.138075284	0.152	1.147778962	0.1735	1.182504822
0.131	1.146838298	0.1525	1.146548168	0.174	1.187062167
0.1315	1.147634967	0.153	1.145419108	0.1745	1.185012378
0.132	1.146334247	0.1535	1.138287155	0.175	1.16208196
0.1325	1.149195256	0.154	1.135501294	0.1755	1.157437779
0.133	1.148783163	0.1545	1.119318065	0.176	1.149621085
0.1335	1.155527255	0.155	1.129972477	0.1765	1.1377653
0.134	1.154259866	0.1555	1.125632421	0.177	1.146452296
0.1345	1.151816985	0.156	1.135223764	0.1775	1.142366567
0.135	1.140960389	0.1565	1.143636383	0.178	1.147864051
0.1355	1.151900252	0.157	1.134357861	0.1785	1.123442028
0.136	1.13867944	0.1575	1.132841521	0.179	1.135988754
0.1365	1.140796092	0.158	1.117826321	0.1795	1.127617815
0.137	1.136289445	0.1585	1.111998566	0.18	1.122802357
0.1375	1.141111561	0.159	1.117745803	0.1805	1.130383237
0.138	1.139134454	0.1595	1.115967632	0.181	1.135508509
0.1385	1.129325934	0.16	1.125155454	0.1815	1.131095227
0.139	1.14359013	0.1605	1.12154215	0.182	1.132825186
0.1395	1.13324566	0.161	1.136255352	0.1825	1.143378007
0.14	1.144511737	0.1615	1.14146223	0.183	1.137488849
0.1405	1.142439964	0.162	1.132995982	0.1835	1.131499813
0.141	1.156373756	0.1625	1.145956147	0.184	1.133306025
0.1415	1.157607878	0.163	1.152972858	0.1845	1.121578992
0.142	1.158071596	0.1635	1.16415401	0.185	1.112313575
0.1425	1.158421638	0.164	1.156044447	0.1855	1.107852738

0.186	1.113660131	0.191	1.153426216	0.196	1.142691267
0.1865	1.104313582	0.1915	1.162436865	0.1965	1.143113978
0.187	1.110800708	0.192	1.145646057	0.197	1.13999048
0.1875	1.101951906	0.1925	1.146837215	0.1975	1.145255612
0.188	1.122734219	0.193	1.158392432	0.198	1.149356145
0.1885	1.12171643	0.1935	1.153999016	0.1985	1.125326603
0.189	1.13197679	0.194	1.166071996	0.199	1.134018922
0.1895	1.136611997	0.1945	1.165080227	0.1995	1.13956437
0.19	1.141323879	0.195	1.153958796	0.2	1.144747037
0.1905	1.155162649	0.1955	1.142661516		

Appendix D: Raw measurement data for experimental compression

File name	Post area (nm^2)	Max load (mN)	Flow Stress (Gpa)	Pre-height (nm)	Post height (nm)	Pastic Strain
Small grain solid core						
Cu_1886_pre_70_g2_s_05x26_f	246079.67	0.320	1.299	748.345	687.433	0.081
Cu_1886_pre_70_g2_s_06x26_f	249017.14	0.319	1.280	765.079	677.392	0.115
Cu_1886_pre_70_g2_s_07x26_f	257317.71	0.320	1.242	760.393	672.707	0.115
Cu_1886_pre_70_g2_s_08x26_f	250426.53	0.320	1.279	765.079	694.126	0.093
Cu_1886_pre_70_g2_s_09x26_f	242018.40	0.295	1.219	753.030	684.755	0.091
Cu_1886_pre_70_g2_s_10x26_f	246758.40	0.320	1.296	746.337	684.755	0.083
Cu_1886_pre_70_g2_s_11x26_f	243539.05	0.310	1.271	738.974	661.328	0.105
Cu_1886_pre_70_g2_s_12x26_f	249250.80	0.311	1.249	736.966	663.336	0.100
Cu_1886_pre_70_g2_s_13x26_f	249836.81	0.251	1.005	746.337	668.021	0.105
Cu_1886_pre_70_g2_s_01x27_f	288101.77	0.348	1.208	741.651	653.965	0.118
Cu_1886_pre_70_g2_s_03x27_f	283309.84	0.344	1.213	722.909	644.594	0.108
Cu_1886_pre_70_g2_s_04x27_f	286473.56	0.339	1.182	698.812	632.545	0.095
Cu_1886_pre_70_g2_s_05x27_f	285572.29	0.324	1.134	727.595	680.070	0.065
Cu_1886_pre_70_g2_s_06x27_f	293242.34	0.313	1.066	738.974	687.433	0.070
Cu_1886_pre_70_g2_s_07x27_f	278046.88	0.320	1.152	727.595	663.336	0.088
Cu_1886_pre_70_g2_s_08x27_f	284263.04	0.337	1.186	738.974	656.642	0.111
Cu_1886_pre_70_g2_s_09x27_f	294918.77	0.342	1.159	765.079	684.755	0.105
Cu_1886_pre_70_g2_s_10x27_f	293943.33	0.346	1.177	741.651	653.965	0.118
Cu_1886_pre_70_g2_s_11x27_f	300422.82	0.350	1.167	757.716	658.650	0.131
Cu_1886_pre_70_g2_s_12x27_f	286269.56	0.339	1.183	727.595	663.336	0.088
Cu_1886_pre_70_g2_s_13x27_f	290712.86	0.345	1.187	755.708	644.594	0.147
Cu_1886_pre_70_g2_s_01x28_f	281470.22	0.348	1.235	774.450	637.900	0.176
Cu_1886_pre_70_g2_s_02x28_f	279734.44	0.311	1.112	812.603	724.917	0.108
Cu_1886_pre_70_g2_s_03x28_f	290594.17	0.353	1.216	736.966	647.271	0.122
Cu_1886_pre_70_g2_s_04x28_f	288094.36	0.317	1.099	769.764	706.175	0.083
Cu_1886_pre_70_g2_s_05x28_f	288669.24	0.344	1.190	736.966	647.271	0.122
Cu_1886_pre_70_g2_s_06x28_f	290460.65	0.344	1.183	706.175	639.908	0.094
Cu_1886_pre_70_g2_s_07x28_f	292786.14	0.346	1.181	741.651	647.271	0.127
Cu_1886_pre_70_g2_s_08x28_f	284337.22	0.350	1.230	738.974	658.650	0.109
Cu_1886_pre_70_g2_s_09x28_f	290709.15	0.353	1.214	729.603	642.586	0.119
Cu_1886_pre_70_g2_s_10x28_f	289136.56	0.343	1.188	741.651	670.699	0.096
Cu_1886_pre_70_g2_s_11x28_f	284489.28	0.331	1.163	736.966	696.804	0.054
Cu_1886_pre_70_g2_s_12x28_f	302985.68	0.353	1.164	741.651	682.747	0.079
Cu_1886_pre_70_g2_s_01x29_f	261783.25	0.341	1.302	746.337	630.537	0.155
Cu_1886_pre_70_g2_s_02x29_f	273277.20	0.347	1.270	724.917	613.803	0.153
Cu_1886_pre_70_g2_s_03x29_f	282130.41	0.351	1.246	692.118	621.166	0.103
Cu_1886_pre_70_g2_s_04x29_f	283714.12	0.349	1.229	703.498	613.803	0.127
Cu_1886_pre_70_g2_s_05x29_f	275543.36	0.343	1.245	743.659	635.223	0.146
Cu_1886_pre_70_g2_s_06x29_f	285312.66	0.341	1.195	724.917	632.545	0.127
Cu_1886_pre_70_g2_s_07x29_f	289707.74	0.353	1.217	765.079	635.223	0.170
Cu_1886_pre_70_g2_s_08x29_f	303749.72	0.365	1.203	767.756	692.118	0.099
Cu_1886_pre_70_g2_s_09x29_f	294707.37	0.350	1.189	724.917	651.957	0.101
Cu_1886_pre_70_g2_s_10x29_f	285817.08	0.343	1.200	781.813	668.021	0.146
Cu_1886_pre_70_g2_s_11x29_f	299139.53	0.356	1.191	769.764	644.594	0.163
Cu_1886_pre_70_g2_s_12x29_f	298891.03	0.348	1.165	757.716	627.860	0.171
Cu_1886_pre_70_g2_s_13x29_f	295656.85	0.357	1.208	753.030	649.279	0.138
Cu_1886_pre_70_g2_s_02x30_f	273510.87	0.343	1.254	701.489	625.852	0.108
Cu_1886_pre_70_g2_s_03x30_f	280101.62	0.339	1.209	746.337	639.908	0.143

Cu_1886_pre_70_g2_s_04x30_f	285038.20	0.352	1.237	753.030	658.650	0.125
Cu_1886_pre_70_g2_s_05x30_f	288850.98	0.341	1.179	748.345	635.223	0.151
Cu_1886_pre_70_g2_s_06x30_f	286206.51	0.350	1.222	724.917	656.642	0.094
Cu_1886_pre_70_g2_s_07x30_f	280810.03	0.357	1.270	769.764	672.707	0.126
Cu_1886_pre_70_g2_s_08x30_f	282994.58	0.358	1.267	720.232	618.489	0.141
Cu_1886_pre_70_g2_s_09x30_f	271548.85	0.357	1.314	736.966	630.537	0.144
Cu_1886_pre_70_g2_s_10x30_f	290501.45	0.353	1.215	767.756	670.699	0.126
Cu_1886_pre_70_g2_s_11x30_f	294584.97	0.361	1.224	755.708	653.965	0.135
Cu_1886_pre_70_g2_s_12x30_f	304135.45	0.366	1.203	762.401	651.957	0.145
Cu_1886_pre_70_g2_s_13x30_f	298212.30	0.361	1.211	743.659	635.223	0.146
Cu_1886_pre_70_g2_s_02x31_f	272034.72	0.334	1.229	795.869	701.489	0.119
Cu_1886_pre_70_g2_s_04x31_f	275814.11	0.331	1.201	727.595	651.957	0.104
Cu_1886_pre_70_g2_s_05x31_f	289084.64	0.348	1.204	741.651	666.013	0.102
Cu_1886_pre_70_g2_s_07x31_f	271252.13	0.349	1.288	779.135	682.747	0.124
Cu_1886_pre_70_g2_s_08x31_f	273429.27	0.347	1.267	708.183	642.586	0.093
Cu_1886_pre_70_g2_s_09x31_f	271370.82	0.347	1.280	727.595	680.070	0.065
Cu_1886_pre_70_g2_s_10x31_f	277212.37	0.344	1.241	743.659	658.650	0.114
Cu_1886_pre_70_g2_s_11x31_f	286673.84	0.345	1.204	774.450	689.441	0.110
Cu_1886_pre_70_g2_s_12x31_f	275335.66	0.352	1.277	751.022	672.707	0.104
Cu_1886_pre_70_g2_s_02x32_f	292322.53	0.332	1.137	710.861	637.900	0.103
Cu_1886_pre_70_g2_s_03x32_f	296372.67	0.335	1.130	762.401	661.328	0.133
Cu_1886_pre_70_g2_s_05x32_f	306130.85	0.348	1.136	772.442	670.699	0.132
Cu_1886_pre_70_g2_s_08x32_f	292196.42	0.323	1.107	757.716	666.013	0.121
Cu_1886_pre_70_g2_s_10x32_f	297774.65	0.329	1.104	743.659	682.747	0.082
Cu_1886_pre_70_g2_s_11x32_f	313645.13	0.345	1.100	757.716	677.392	0.106
Cu_1886_pre_70_g2_s_12x32_f	286354.87	0.327	1.143	734.288	689.441	0.061
Cu_1886_pre_70_g2_s_02x33_f	269054.00	0.365	1.355	712.869	635.223	0.109
Cu_1886_pre_70_g2_s_03x33_f	271654.03	0.360	1.327	751.022	647.271	0.138
Cu_1886_pre_70_g2_s_05x33_f	279123.42	0.350	1.255	715.546	656.642	0.082
Cu_1886_pre_70_g2_s_06x33_f	286055.06	0.359	1.256	736.966	651.957	0.115
Cu_1886_pre_70_g2_s_07x33_f	281473.40	0.351	1.248	717.554	635.223	0.115
Cu_1886_pre_70_g2_s_08x33_f	270067.66	0.349	1.291	710.861	599.747	0.156
Cu_1886_pre_70_g2_s_09x33_f	274937.01	0.348	1.267	696.804	632.545	0.092
Cu_1886_pre_70_g2_s_10x33_f	283904.05	0.359	1.266	743.659	658.650	0.114
Cu_1886_pre_70_g2_s_11x33_f	280040.29	0.351	1.255	748.345	637.900	0.148
Cu_1886_pre_70_g2_s_12x33_f	276735.80	0.354	1.281	743.659	639.908	0.140
Cu_1886_pre_70_g2_s_13x33_f	278677.09	0.356	1.277	734.288	658.650	0.103
Small grain hollow						
Cu_1886_pre_70_g2_h_25x49_f	272535.95	0.332	1.220	692.118	656.642	0.051
Cu_1886_pre_70_g2_h_24x49_f	268806.63	0.335	1.245	661.328	590.376	0.107
Cu_1886_pre_70_g2_h_23x49_f	262703.13	0.331	1.259	684.755	616.481	0.100
Cu_1886_pre_70_g2_h_22x49_f	249982.58	0.320	1.279	684.755	597.739	0.127
Cu_1886_pre_70_g2_h_21x49_f	244190.98	0.311	1.272	722.909	642.586	0.111
Cu_1886_pre_70_g2_h_20x49_f	243559.12	0.305	1.251	734.288	602.424	0.180
Cu_1886_pre_70_g2_h_19x49_f	242279.27	0.312	1.286	712.869	599.747	0.159
Cu_1886_pre_70_g2_h_18x49_f	243838.75	0.304	1.246	687.433	597.739	0.130
Cu_1886_pre_70_g2_h_17x49_f	241432.31	0.301	1.245	682.747	627.860	0.080
Cu_1886_pre_70_g2_h_16x49_f	247089.47	0.309	1.249	689.441	613.803	0.110
Cu_1886_pre_70_g2_h_15x49_f	248017.10	0.307	1.239	692.118	611.795	0.116
Cu_1886_pre_70_g2_h_14x49_f	249001.18	0.322	1.292	668.021	576.319	0.137
Cu_1886_pre_70_g2_h_25x48_f	265050.42	0.327	1.233	694.126	583.013	0.160
Cu_1886_pre_70_g2_h_24x48_f	257852.60	0.327	1.267	680.070	583.013	0.143
Cu_1886_pre_70_g2_h_23x48_f	258387.66	0.324	1.253	684.755	607.110	0.113
Cu_1886_pre_70_g2_h_22x48_f	249202.84	0.323	1.296	720.232	578.327	0.197

Cu_1886_pre_70_g2_h_21x48_f	248810.28	0.325	1.306	706.175	602.424	0.147
Cu_1886_pre_70_g2_h_20x48_f	246097.32	0.316	1.284	698.812	595.061	0.148
Cu_1886_pre_70_g2_h_19x48_f	240397.13	0.310	1.289	689.441	607.110	0.119
Cu_1886_pre_70_g2_h_18x48_f	237538.98	0.303	1.274	708.183	597.739	0.156
Cu_1886_pre_70_g2_h_17x48_f	242279.27	0.317	1.307	703.498	576.319	0.181
Cu_1886_pre_70_g2_h_16x48_f	242994.48	0.310	1.277	682.747	621.166	0.090
Cu_1886_pre_70_g2_h_15x48_f	241695.81	0.304	1.258	727.595	613.803	0.156
Cu_1886_pre_70_g2_h_14x48_f	244172.16	0.302	1.237	613.803	550.214	0.104
Cu_1886_pre_70_g2_h_24x50_f	279809.06	0.318	1.135	698.812	603.763	0.136
Cu_1886_pre_70_g2_h_23x50_f	269532.60	0.315	1.170	672.707	568.956	0.154
Cu_1886_pre_70_g2_h_22x50_f	248853.30	0.300	1.206	703.498	590.376	0.161
Cu_1886_pre_70_g2_h_21x50_f	256470.57	0.293	1.144	684.755	578.327	0.155
Cu_1886_pre_70_g2_h_20x50_f	233427.85	0.286	1.225	675.384	573.642	0.151
Cu_1886_pre_70_g2_h_18x50_f	245739.71	0.283	1.151	670.699	542.851	0.191
Cu_1886_pre_70_g2_h_17x50_f	243618.28	0.290	1.192	680.070	571.634	0.159
Cu_1886_pre_70_g2_h_16x50_f	246046.23	0.271	1.103	694.126	583.013	0.160
Cu_1886_pre_70_g2_h_15x50_f	235533.16	0.271	1.151	689.441	587.698	0.148
Cu_1886_pre_70_g2_h_14x50_f	226130.55	0.289	1.280	694.126	604.432	0.129
Cu_1886_pre_70_g2_h_25x47_f	245634.85	0.314	1.280	738.974	637.900	0.137
Cu_1886_pre_70_g2_h_24x47_f	241779.16	0.313	1.296	727.595	627.860	0.137
Cu_1886_pre_70_g2_h_23x47_f	250563.36	0.304	1.212	710.861	623.174	0.123
Cu_1886_pre_70_g2_h_22x47_f	250367.08	0.307	1.226	698.812	637.900	0.087
Cu_1886_pre_70_g2_h_21x47_f	232250.18	0.301	1.297	720.232	625.852	0.131
Cu_1886_pre_70_g2_h_20x47_f	236821.08	0.304	1.284	710.861	607.110	0.146
Cu_1886_pre_70_g2_h_19x47_f	237756.77	0.295	1.243	736.966	635.223	0.138
Cu_1886_pre_70_g2_h_18x47_f	227714.23	0.290	1.273	753.030	627.860	0.166
Cu_1886_pre_70_g2_h_17x47_f	232451.83	0.306	1.318	703.498	623.174	0.114
Cu_1886_pre_70_g2_h_16x47_f	245855.33	0.321	1.304	682.747	571.634	0.163
Cu_1886_pre_70_g2_h_15x47_f	237439.49	0.312	1.313	708.183	611.795	0.136
Cu_1886_pre_70_g2_h_14x47_f	236283.32	0.308	1.303	729.603	623.174	0.146
Cu_1886_pre_70_g2_h_13x47_f	243715.07	0.303	1.245	675.384	611.795	0.094
Cu_1886_pre_70_g2_h_25x46_f	237579.31	0.315	1.324	722.909	642.586	0.111
Cu_1886_pre_70_g2_h_24x46_f	244717.98	0.308	1.260	689.441	621.166	0.099
Cu_1886_pre_70_g2_h_23x46_f	235944.54	0.296	1.255	689.441	599.747	0.130
Cu_1886_pre_70_g2_h_22x46_f	239582.44	0.295	1.232	687.433	607.110	0.117
Cu_1886_pre_70_g2_h_21x46_f	239714.19	0.308	1.286	712.869	625.852	0.122
Cu_1886_pre_70_g2_h_20x46_f	241988.88	0.306	1.265	736.966	630.537	0.144
Cu_1886_pre_70_g2_h_19x46_f	230822.44	0.293	1.270	720.232	623.174	0.135
Cu_1886_pre_70_g2_h_18x46_f	229467.30	0.302	1.317	702.828	625.852	0.110
Cu_1886_pre_70_g2_h_17x46_f	227415.78	0.300	1.318	698.812	623.174	0.108
Cu_1886_pre_70_g2_h_16x46_f	239657.72	0.290	1.208	692.118	635.223	0.082
Cu_1886_pre_70_g2_h_15x46_f	242169.03	0.305	1.259	717.554	616.481	0.141
Cu_1886_pre_70_g2_h_14x46_f	243422.00	0.296	1.215	717.554	632.545	0.118
Cu_1886_pre_70_g2_h_24x45_f	254577.68	0.307	1.205	736.966	621.166	0.157
Cu_1886_pre_70_g2_h_23x45_f	255397.76	0.306	1.197	724.917	618.489	0.147
Cu_1886_pre_70_g2_h_22x45_f	282081.06	0.324	1.148	682.747	581.005	0.149
Cu_1886_pre_70_g2_h_21x45_f	261727.11	0.297	1.134	712.869	621.836	0.128
Cu_1886_pre_70_g2_h_20x45_f	258065.01	0.302	1.171	727.595	607.110	0.166
Cu_1886_pre_70_g2_h_19x45_f	259648.69	0.308	1.188	696.804	609.118	0.126
Cu_1886_pre_70_g2_h_18x45_f	259597.61	0.306	1.178	706.175	611.795	0.134
Cu_1886_pre_70_g2_h_17x45_f	256701.81	0.302	1.175	708.183	602.424	0.149
Cu_1886_pre_70_g2_h_16x45_f	252566.49	0.312	1.236	724.917	592.384	0.183
Cu_1886_pre_70_g2_h_15x45_f	246729.18	0.302	1.225	751.022	613.803	0.183
Cu_1886_pre_70_g2_h_14x45_f	251082.29	0.309	1.230	753.030	618.489	0.179

Cu_1886_pre_70_g2_h_13x45_f	246592.05	0.312	1.264	743.659	637.900	0.142
Cu_1886_pre_70_g2_h_25x43_f	262856.39	0.311	1.183	706.175	616.481	0.127
Cu_1886_pre_70_g2_h_24x43_f	250200.37	0.302	1.208	687.433	630.537	0.083
Cu_1886_pre_70_g2_h_23x43_f	258976.50	0.301	1.161	663.336	578.327	0.128
Cu_1886_pre_70_g2_h_22x43_f	253184.90	0.317	1.251	684.755	602.424	0.120
Cu_1886_pre_70_g2_h_21x43_f	252351.39	0.308	1.220	694.126	609.118	0.122
Cu_1886_pre_70_g2_h_20x43_f	243897.91	0.311	1.275	717.554	604.432	0.158
Cu_1886_pre_70_g2_h_19x43_f	255685.45	0.301	1.177	699.481	581.005	0.169
Cu_1886_pre_70_g2_h_18x43_f	251396.87	0.312	1.242	694.126	609.118	0.122
Cu_1886_pre_70_g2_h_17x43_f	247554.63	0.300	1.210	706.175	599.747	0.151
Cu_1886_pre_70_g2_h_16x43_f	256779.78	0.304	1.183	680.070	602.424	0.114
Cu_1886_pre_70_g2_h_15x43_f	255798.38	0.309	1.206	729.603	602.424	0.174
Cu_1886_pre_70_g2_h_14x43_f	260616.65	0.304	1.166	701.489	597.739	0.148
Small grain c-shaped						
Cu_1886_pre_70_g2_c_22x52_f	234315.15	0.284	1.212	729.603	616.481	0.155
Cu_1886_pre_70_g2_c_21x52_f	235845.05	0.271	1.149	734.288	651.957	0.112
Cu_1886_pre_70_g2_c_20x52_f	219924.88	0.277	1.258	701.489	625.852	0.108
Cu_1886_pre_70_g2_c_19x52_f	223267.01	0.276	1.236	717.554	630.537	0.121
Cu_1886_pre_70_g2_c_18x52_f	221971.03	0.266	1.200	712.869	663.336	0.069
Cu_1886_pre_70_g2_c_17x52_f	226240.78	0.264	1.169	720.232	630.537	0.125
Cu_1886_pre_70_g2_c_25x53_f	240434.78	0.283	1.179	734.288	644.594	0.122
Cu_1886_pre_70_g2_c_24x53_f	237883.14	0.287	1.208	727.595	633.215	0.130
Cu_1886_pre_70_g2_c_23x53_f	237210.95	0.291	1.227	751.022	642.586	0.144
Cu_1886_pre_70_g2_c_22x53_f	232008.19	0.287	1.237	727.595	604.432	0.169
Cu_1886_pre_70_g2_c_21x53_f	236557.58	0.282	1.191	703.498	613.803	0.127
Cu_1886_pre_70_g2_c_20x53_f	235191.68	0.274	1.164	701.489	623.174	0.112
Cu_1886_pre_70_g2_c_19x53_f	225834.78	0.272	1.203	727.595	616.481	0.153
Cu_1886_pre_70_g2_c_16x53_f	234605.53	0.280	1.193	706.175	597.739	0.154
Cu_1886_pre_70_g2_c_15x53_f	228999.46	0.275	1.201	694.126	616.481	0.112
Cu_1886_pre_70_g2_c_25x54_f	226598.39	0.290	1.279	701.489	630.537	0.101
Cu_1886_pre_70_g2_c_24x54_f	241736.14	0.292	1.210	706.175	609.118	0.137
Cu_1886_pre_70_g2_c_23x54_f	236541.45	0.289	1.221	741.651	607.110	0.181
Cu_1886_pre_70_g2_c_22x54_f	231405.90	0.277	1.197	736.966	595.061	0.193
Cu_1886_pre_70_g2_c_21x54_f	222444.25	0.271	1.220	767.756	637.900	0.169
Cu_1886_pre_70_g2_c_18x54_f	220029.74	0.272	1.235	727.595	632.545	0.131
Cu_1886_pre_70_g2_c_17x54_f	224294.12	0.283	1.263	722.909	604.432	0.164
Cu_1886_pre_70_g2_c_15x54_f	221153.64	0.269	1.214	729.603	618.489	0.152
Cu_1886_pre_70_g2_c_25x55_f	223710.66	0.283	1.267	741.651	621.166	0.162
Cu_1886_pre_70_g2_c_24x55_f	228555.81	0.289	1.264	729.603	623.174	0.146
Cu_1886_pre_70_g2_c_23x55_f	231661.34	0.292	1.262	727.595	602.424	0.172
Cu_1886_pre_70_g2_c_20x55_f	222852.94	0.280	1.257	684.755	607.110	0.113
Cu_1886_pre_70_g2_c_17x55_f	224525.35	0.280	1.249	736.966	621.166	0.157
Cu_1886_pre_70_g2_c_16x55_f	224560.31	0.278	1.239	724.917	621.166	0.143
Cu_1886_pre_70_g2_c_15x55_f	226364.47	0.284	1.255	738.974	602.424	0.185
Cu_1886_pre_70_g2_c_25x56_f	234670.06	0.282	1.201	786.498	668.021	0.151
Cu_1886_pre_70_g2_c_24x56_f	229128.52	0.281	1.225	753.030	613.803	0.185
Cu_1886_pre_70_g2_c_23x56_f	228241.23	0.282	1.235	777.127	630.537	0.189
Cu_1886_pre_70_g2_c_22x56_f	220207.20	0.279	1.267	781.813	666.013	0.148
Cu_1886_pre_70_g2_c_21x56_f	230405.68	0.268	1.164	772.442	684.755	0.114
Cu_1886_pre_70_g2_c_20x56_f	223675.70	0.268	1.197	727.595	621.166	0.146
Cu_1886_pre_70_g2_c_19x56_f	228752.09	0.273	1.191	786.498	649.279	0.174
Cu_1886_pre_70_g2_c_18x56_f	224958.24	0.278	1.236	720.232	635.223	0.118
Cu_1886_pre_70_g2_c_17x56_f	221949.52	0.276	1.242	729.603	611.795	0.161
Cu_1886_pre_70_g2_c_16x56_f	227144.21	0.273	1.202	724.917	602.424	0.169

Cu_1886_pre_70_g2_c_15x56_f	227864.80	0.276	1.212	722.909	602.424	0.167
Cu_1886_pre_70_g2_c_25x57_f	227362.00	0.275	1.210	847.410	666.013	0.214
Cu_1886_pre_70_g2_c_24x57_f	220395.41	0.274	1.244	769.764	682.747	0.113
Cu_1886_pre_70_g2_c_23x57_f	229026.35	0.273	1.192	743.659	647.271	0.130
Cu_1886_pre_70_g2_c_22x57_f	232941.19	0.280	1.203	741.651	632.545	0.147
Cu_1886_pre_70_g2_c_21x57_f	225415.33	0.275	1.218	781.813	651.957	0.166
Cu_1886_pre_70_g2_c_20x57_f	228787.05	0.269	1.177	714.877	649.279	0.092
Cu_1886_pre_70_g2_c_19x57_f	231018.72	0.268	1.161	732.280	630.537	0.139
Cu_1886_pre_70_g2_c_18x57_f	226278.43	0.279	1.233	777.127	649.279	0.165
Cu_1886_pre_70_g2_c_17x57_f	222597.51	0.275	1.235	760.393	661.328	0.130
Cu_1886_pre_70_g2_c_16x57_f	230083.03	0.270	1.174	738.974	658.650	0.109
Cu_1886_pre_70_g2_c_15x57_f	227652.39	0.279	1.224	755.708	658.650	0.128
Small grain x-shaped						
Cu_1886_pre_70_g2_x_02x74_f	152278.23	0.175	1.147	743.659	644.594	0.133
Cu_1886_pre_70_g2_x_03x74_f	148081.06	0.172	1.161	701.489	573.642	0.182
Cu_1886_pre_70_g2_x_04x74_f	155012.70	0.171	1.101	748.345	616.481	0.176
Cu_1886_pre_70_g2_x_05x74_f	143262.80	0.171	1.193	765.079	621.166	0.188
Cu_1886_pre_70_g2_x_06x74_f	135809.54	0.167	1.231	732.280	581.005	0.207
Cu_1886_pre_70_g2_x_07x74_f	141646.85	0.173	1.224	720.232	613.803	0.148
Cu_1886_pre_70_g2_x_08x74_f	155055.72	0.166	1.072	710.861	625.852	0.120
Cu_1886_pre_70_g2_x_10x74_f	148761.32	0.172	1.157	741.651	623.174	0.160
Cu_1886_pre_70_g2_x_11x74_f	149331.34	0.174	1.166	639.908	550.214	0.140
Cu_1886_pre_70_g2_x_02x49_f	144599.11	0.174	1.207	616.981	530.189	0.141
Cu_1886_pre_70_g2_x_09x49_f	143502.10	0.172	1.199	610.063	523.899	0.141
Cu_1886_pre_70_g2_x_11x49_f	147217.97	0.168	1.140	694.340	594.340	0.144
Cu_1886_pre_70_g2_x_03x48_f	147664.31	0.176	1.194	608.176	501.258	0.176
Cu_1886_pre_70_g2_x_04x48_f	157443.35	0.173	1.100	627.673	541.509	0.137
Cu_1886_pre_70_g2_x_07x48_f	152716.50	0.174	1.138	674.214	570.440	0.154
Cu_1886_pre_70_g2_x_08x48_f	153144.01	0.178	1.165	663.522	556.604	0.161
Cu_1886_pre_70_g2_x_02x46_f	145564.38	0.162	1.110	654.717	543.396	0.170
Cu_1886_pre_70_g2_x_03x46_f	149325.96	0.166	1.114	623.270	563.522	0.096
Cu_1886_pre_70_g2_x_08x46_f	147572.89	0.163	1.104	667.925	567.925	0.150
Cu_1886_pre_70_g2_x_09x46_f	144948.65	0.156	1.073	643.396	559.119	0.131
Cu_1886_pre_70_g2_x_10x46_f	150525.15	0.175	1.164	701.258	552.201	0.213
Cu_1886_pre_70_g2_x_11x46_f	143292.37	0.154	1.075	654.717	543.396	0.170
Cu_1886_pre_70_g2_x_12x46_f	151775.43	0.170	1.122	663.522	550.314	0.171
Cu_1886_pre_70_g2_x_02x22_f	146518.89	0.173	1.183	696.855	585.535	0.160
Cu_1886_pre_70_g2_x_07x22_f	171228.65	0.189	1.106	688.050	554.717	0.194
Cu_1886_pre_70_g2_x_08x22_f	169510.52	0.184	1.085	685.535	547.799	0.201
Cu_1886_pre_70_g2_x_09x22_f	165926.40	0.187	1.127	689.937	572.327	0.170
Cu_1886_pre_70_g2_x_10x22_f	160250.42	0.185	1.153	723.270	621.384	0.141
Cu_1886_pre_70_g2_x_11x22_f	168867.91	0.196	1.159	638.994	550.314	0.139
Cu_1886_pre_70_g2_x_12x22_f	162086.84	0.199	1.225	663.522	574.843	0.134
Cu_1886_pre_70_g2_x_03x23_f	157572.41	0.184	1.168	659.119	574.843	0.128
Cu_1886_pre_70_g2_x_04x23_f	161172.66	0.183	1.137	654.717	588.050	0.102
Cu_1886_pre_70_g2_x_06x23_f	158766.22	0.184	1.158	688.050	603.774	0.122
Cu_1886_pre_70_g2_x_07x23_f	159812.15	0.184	1.153	650.314	572.327	0.120
Cu_1886_pre_70_g2_x_08x23_f	168975.46	0.189	1.121	659.119	603.774	0.084
Cu_1886_pre_70_g2_x_09x23_f	165017.60	0.188	1.136	669.811	588.050	0.122
Cu_1886_pre_70_g2_x_10x23_f	165036.42	0.191	1.155	669.811	583.648	0.129
Cu_1886_pre_70_g2_x_11x23_f	169835.86	0.187	1.099	663.522	589.937	0.111
Cu_1886_pre_70_g2_x_12x23_f	175648.98	0.192	1.096	645.912	574.843	0.110
Medium grain solid core						
Cu_1878_pre_70_g2_s_02x03_f	343739.83	0.408	1.187	797.877	649.279	0.186

Cu_1878_pre_70_g2_s_03x03_f	322743.26	0.398	1.232	812.603	677.392	0.166
Cu_1878_pre_70_g2_s_04x03_f	316083.19	0.390	1.233	788.506	694.126	0.120
Cu_1878_pre_70_g2_s_05x03_f	313485.84	0.395	1.260	777.127	677.392	0.128
Cu_1878_pre_70_g2_s_06x03_f	317271.63	0.402	1.268	781.813	637.900	0.184
Cu_1878_pre_70_g2_s_07x03_f	323014.83	0.404	1.250	788.506	658.650	0.165
Cu_1878_pre_70_g2_s_08x03_f	338461.79	0.405	1.197	748.345	639.908	0.145
Cu_1878_pre_70_g2_s_09x03_f	320482.01	0.416	1.299	767.756	642.586	0.163
Cu_1878_pre_70_g2_s_01x04_f	316134.28	0.403	1.275	751.022	656.642	0.126
Cu_1878_pre_70_g2_s_02x04_f	312595.86	0.402	1.286	777.127	651.957	0.161
Cu_1878_pre_70_g2_s_03x04_f	315779.36	0.400	1.268	786.498	656.642	0.165
Cu_1878_pre_70_g2_s_04x04_f	308159.40	0.376	1.221	779.135	698.812	0.103
Cu_1878_pre_70_g2_s_05x04_f	309044.00	0.394	1.274	791.184	663.336	0.162
Cu_1878_pre_70_g2_s_06x04_f	309323.64	0.402	1.300	765.079	649.279	0.151
Cu_1878_pre_70_g2_s_07x04_f	302182.27	0.388	1.283	788.506	677.392	0.141
Cu_1878_pre_70_g2_s_08x04_f	302857.15	0.369	1.218	783.821	701.489	0.105
Cu_1878_pre_70_g2_s_09x04_f	313082.53	0.384	1.226	757.716	668.021	0.118
Cu_1878_pre_70_g2_s_10x04_f	310912.70	0.391	1.258	743.659	666.013	0.104
Cu_1878_pre_70_g2_s_11x04_f	310044.22	0.390	1.257	755.708	647.271	0.143
Cu_1878_pre_70_g2_s_12x04_f	320605.69	0.401	1.250	779.135	637.900	0.181
Cu_1878_pre_70_g2_s_13x04_f	322482.45	0.395	1.224	797.877	684.755	0.142
Cu_1878_pre_70_g2_s_01x05_f	295151.15	0.390	1.321	786.498	632.545	0.196
Cu_1878_pre_70_g2_s_02x05_f	298560.51	0.389	1.304	772.442	661.328	0.144
Cu_1878_pre_70_g2_s_03x05_f	301063.75	0.394	1.310	762.401	653.965	0.142
Cu_1878_pre_70_g2_s_04x05_f	303771.33	0.392	1.290	748.345	647.271	0.135
Cu_1878_pre_70_g2_s_05x05_f	305287.80	0.383	1.255	760.393	689.441	0.093
Cu_1878_pre_70_g2_s_06x05_f	308586.91	0.397	1.287	781.813	658.650	0.158
Cu_1878_pre_70_g2_s_13x05_f	306080.98	0.385	1.258	741.651	684.755	0.077
Cu_1878_pre_70_g2_s_13x05_f	297858.74	0.363	1.220	807.918	724.917	0.103
Cu_1878_pre_70_g2_s_13x05_f	304142.38	0.392	1.289	743.659	658.650	0.114
Cu_1878_pre_70_g2_s_13x05_f	307933.54	0.390	1.267	779.135	663.336	0.149
Cu_1878_pre_70_g2_s_13x05_f	307578.63	0.405	1.316	760.393	656.642	0.136
Cu_1878_pre_70_g2_s_13x05_f	294876.90	0.376	1.274	741.651	656.642	0.115
Cu_1878_pre_70_g2_s_13x05_f	311584.89	0.394	1.264	767.756	661.328	0.139
Cu_1878_pre_70_g2_s_01x06_f	304502.68	0.390	1.281	716.352	623.270	0.130
Cu_1878_pre_70_g2_s_02x06_f	303558.92	0.389	1.282	703.145	618.868	0.120
Cu_1878_pre_70_g2_s_03x06_f	305976.12	0.394	1.289	725.786	616.981	0.150
Cu_1878_pre_70_g2_s_04x06_f	313692.88	0.392	1.249	703.145	616.981	0.123
Cu_1878_pre_70_g2_s_05x06_f	305774.46	0.383	1.253	743.396	625.786	0.158
Cu_1878_pre_70_g2_s_06x06_f	305024.30	0.397	1.302	734.591	632.075	0.140
Cu_1878_pre_70_g2_s_07x06_f	301991.37	0.385	1.275	705.660	605.660	0.142
Cu_1878_pre_70_g2_s_08x06_f	302373.18	0.363	1.202	701.258	630.189	0.101
Cu_1878_pre_70_g2_s_09x06_f	300071.59	0.392	1.307	683.648	632.075	0.075
Cu_1878_pre_70_g2_s_10x06_f	305688.42	0.390	1.276	727.673	634.591	0.128
Cu_1878_pre_70_g2_s_11x06_f	308449.79	0.405	1.313	716.352	634.591	0.114
Cu_1878_pre_70_g2_s_01x07_f	305857.82	0.374	1.224	721.384	650.314	0.099
Cu_1878_pre_70_g2_s_02x07_f	325442.78	0.399	1.226	694.340	627.673	0.096
Cu_1878_pre_70_g2_s_03x07_f	309966.25	0.389	1.255	710.063	652.201	0.081
Cu_1878_pre_70_g2_s_04x07_f	302693.14	0.395	1.304	696.855	627.673	0.099
Cu_1878_pre_70_g2_s_05x07_f	301951.04	0.384	1.271	710.063	636.478	0.104
Cu_1878_pre_70_g2_s_06x07_f	309307.50	0.393	1.270	692.453	605.660	0.125
Cu_1878_pre_70_g2_s_07x07_f	305263.60	0.384	1.257	711.950	636.478	0.106
Cu_1878_pre_70_g2_s_08x07_f	305123.78	0.394	1.292	727.673	634.591	0.128
Cu_1878_pre_70_g2_s_09x07_f	310942.27	0.386	1.241	703.145	625.786	0.110
Cu_1878_pre_70_g2_s_10x07_f	294884.96	0.394	1.335	730.189	612.579	0.161

Cu_1878_pre_70_g2_s_11x07_f	299646.77	0.392	1.309	703.145	647.799	0.079
Cu_1878_pre_70_g2_s_12x07_f	306320.28	0.391	1.277	705.660	633.333	0.102
Cu_1878_pre_70_g2_s_13x07_f	295172.66	0.372	1.260	763.522	685.535	0.102
Cu_1878_pre_70_g2_s_01x08_f	318987.06	0.404	1.265	734.591	632.075	0.140
Cu_1878_pre_70_g2_s_02x08_f	315924.55	0.381	1.206	765.409	610.063	0.203
Cu_1878_pre_70_g2_s_03x08_f	325031.40	0.398	1.224	725.786	618.868	0.147
Cu_1878_pre_70_g2_s_04x08_f	320213.13	0.405	1.264	727.673	583.648	0.198
Cu_1878_pre_70_g2_s_05x08_f	326902.78	0.400	1.223	710.063	599.371	0.156
Cu_1878_pre_70_g2_s_06x08_f	323488.05	0.394	1.217	711.950	612.579	0.140
Cu_1878_pre_70_g2_s_07x08_f	324189.82	0.392	1.211	730.189	618.868	0.152
Cu_1878_pre_70_g2_s_08x08_f	323133.13	0.402	1.245	714.465	592.453	0.171
Cu_1878_pre_70_g2_s_09x08_f	333901.64	0.407	1.220	703.145	603.774	0.141
Cu_1878_pre_70_g2_s_10x08_f	313588.02	0.397	1.267	721.384	601.258	0.167
Cu_1878_pre_70_g2_s_11x08_f	320974.06	0.400	1.246	718.868	608.176	0.154
Cu_1878_pre_70_g2_s_12x08_f	320237.33	0.398	1.244	714.465	645.912	0.096
Cu_1878_pre_70_g2_s_13x08_f	317903.49	0.399	1.257	698.742	616.981	0.117
Medium grain x-shaped						
Cu_1878_pre_70_g2_x_01x20_f	173694.24	0.212	1.222	656.604	599.371	0.087
Cu_1878_pre_70_g2_x_02x20_f	175175.75	0.213	1.214	647.799	554.717	0.144
Cu_1878_pre_70_g2_x_03x20_f	175264.48	0.214	1.220	667.925	570.440	0.146
Cu_1878_pre_70_g2_x_04x20_f	182577.92	0.203	1.112	663.522	588.050	0.114
Cu_1878_pre_70_g2_x_05x20_f	175234.91	0.213	1.218	669.811	576.730	0.139
Cu_1878_pre_70_g2_x_06x20_f	176630.38	0.214	1.214	672.327	554.717	0.175
Cu_1878_pre_70_g2_x_07x20_f	169050.75	0.217	1.284	674.214	566.038	0.160
Cu_1878_pre_70_g2_x_08x20_f	176877.74	0.216	1.224	656.604	566.038	0.138
Cu_1878_pre_70_g2_x_09x20_f	175022.49	0.220	1.259	654.717	559.119	0.146
Cu_1878_pre_70_g2_x_10x20_f	180518.33	0.212	1.172	654.717	576.730	0.119
Cu_1878_pre_70_g2_x_11x20_f	174412.14	0.215	1.232	659.119	574.843	0.128
Cu_1878_pre_70_g2_x_12x20_f	182378.96	0.214	1.175	656.604	572.327	0.128
Cu_1878_pre_70_g2_x_01x21_f	183562.01	0.219	1.194	661.006	540.881	0.182
Cu_1878_pre_70_g2_x_02x21_f	181311.52	0.221	1.218	654.717	540.881	0.174
Cu_1878_pre_70_g2_x_03x21_f	176643.82	0.208	1.177	669.811	578.616	0.136
Cu_1878_pre_70_g2_x_04x21_f	174027.65	0.215	1.234	647.799	534.591	0.175
Cu_1878_pre_70_g2_x_05x21_f	178574.35	0.221	1.235	669.811	540.881	0.192
Cu_1878_pre_70_g2_x_06x21_f	172648.31	0.221	1.280	669.811	547.170	0.183
Cu_1878_pre_70_g2_x_07x21_f	179246.54	0.214	1.192	672.327	578.616	0.139
Cu_1878_pre_70_g2_x_08x21_f	177837.63	0.218	1.227	656.604	553.459	0.157
Cu_1878_pre_70_g2_x_09x21_f	174409.45	0.208	1.190	667.925	578.616	0.134
Cu_1878_pre_70_g2_x_10x21_f	178665.77	0.206	1.154	661.006	597.484	0.096
Cu_1878_pre_70_g2_x_11x21_f	185099.99	0.211	1.142	679.245	547.170	0.194
Cu_1878_pre_70_g2_x_12x21_f	172911.81	0.217	1.257	665.409	566.038	0.149
Cu_1878_pre_70_g2_x_01x22_f	179251.92	0.224	1.248	656.604	572.327	0.128
Cu_1878_pre_70_g2_x_02x22_f	181620.72	0.219	1.208	643.396	550.314	0.145
Cu_1878_pre_70_g2_x_03x22_f	180561.35	0.223	1.235	659.119	547.799	0.169
Cu_1878_pre_70_g2_x_04x22_f	184341.75	0.220	1.192	661.006	547.799	0.171
Cu_1878_pre_70_g2_x_05x22_f	177738.15	0.212	1.193	659.119	561.635	0.148
Cu_1878_pre_70_g2_x_06x22_f	184780.02	0.215	1.162	659.119	559.119	0.152
Cu_1878_pre_70_g2_x_07x22_f	180437.67	0.212	1.177	679.245	547.799	0.194
Cu_1878_pre_70_g2_x_08x22_f	176081.87	0.215	1.219	667.925	554.717	0.169
Cu_1878_pre_70_g2_x_09x22_f	171640.03	0.214	1.244	674.214	566.038	0.160
Cu_1878_pre_70_g2_x_10x22_f	183008.13	0.212	1.160	665.409	567.925	0.147
Cu_1878_pre_70_g2_x_11x22_f	167440.17	0.212	1.266	669.811	563.522	0.159
Cu_1878_pre_70_g2_x_12x22_f	182102.01	0.213	1.169	647.799	581.132	0.103
Cu_1878_pre_70_g2_x_01x23_f	171763.71	0.214	1.246	633.333	614.465	0.030

Cu_1878_pre_70_g2_x_02x23_f	185546.32	0.224	1.209	681.132	581.132	0.147
Cu_1878_pre_70_g2_x_03x23_f	174756.31	0.214	1.222	669.811	594.340	0.113
Cu_1878_pre_70_g2_x_04x23_f	184669.78	0.218	1.181	659.119	567.925	0.138
Cu_1878_pre_70_g2_x_05x23_f	184696.67	0.218	1.181	647.799	585.535	0.096
Cu_1878_pre_70_g2_x_06x23_f	177103.60	0.215	1.216	663.522	579.245	0.127
Cu_1878_pre_70_g2_x_07x23_f	177692.44	0.217	1.220	698.742	550.314	0.212
Cu_1878_pre_70_g2_x_08x23_f	179504.67	0.211	1.177	647.799	547.799	0.154
Cu_1878_pre_70_g2_x_09x23_f	175011.74	0.204	1.163	674.214	570.440	0.154
Cu_1878_pre_70_g2_x_10x23_f	174710.60	0.209	1.197	674.214	583.648	0.134
Cu_1878_pre_70_g2_x_11x23_f	179082.53	0.217	1.210	681.132	567.925	0.166
Cu_1878_pre_70_g2_x_12x23_f	180166.10	0.215	1.191	650.314	552.201	0.151
Cu_1878_pre_70_g2_x_01x24_f	176791.70	0.217	1.226	688.050	601.258	0.126
Cu_1878_pre_70_g2_x_02x24_f	178587.80	0.222	1.242	676.730	574.843	0.151
Cu_1878_pre_70_g2_x_03x24_f	185460.28	0.221	1.190	676.730	566.038	0.164
Cu_1878_pre_70_g2_x_04x24_f	181790.12	0.216	1.186	665.409	574.843	0.136
Cu_1878_pre_70_g2_x_05x24_f	179862.27	0.216	1.199	681.132	574.843	0.156
Cu_1878_pre_70_g2_x_06x24_f	178684.59	0.214	1.198	679.245	592.453	0.128
Cu_1878_pre_70_g2_x_07x24_f	174205.11	0.213	1.223	679.245	556.604	0.181
Cu_1878_pre_70_g2_x_08x24_f	175697.37	0.210	1.196	652.201	576.730	0.116
Cu_1878_pre_70_g2_x_09x24_f	169513.21	0.212	1.251	656.604	567.925	0.135
Cu_1878_pre_70_g2_x_10x24_f	174344.92	0.208	1.191	643.396	599.371	0.068
Cu_1878_pre_70_g2_x_11x24_f	178205.99	0.217	1.217	659.119	583.648	0.115
Cu_1878_pre_70_g2_x_12x24_f	169959.55	0.211	1.240	656.604	601.258	0.084
Cu_1878_pre_70_g2_x_02x25_f	189837.59	0.227	1.194	621.384	583.648	0.061
Cu_1878_pre_70_g2_x_03x25_f	183986.84	0.222	1.206	616.981	585.535	0.051
Cu_1878_pre_70_g2_x_04x25_f	187993.10	0.210	1.115	634.591	610.063	0.039
Cu_1878_pre_70_g2_x_05x25_f	177084.78	0.219	1.236	625.786	567.925	0.092
Cu_1878_pre_70_g2_x_06x25_f	171750.27	0.217	1.261	654.717	579.245	0.115
Cu_1878_pre_70_g2_x_07x25_f	179464.33	0.215	1.198	643.396	581.132	0.097
Cu_1878_pre_70_g2_x_08x25_f	181185.14	0.216	1.194	627.673	570.440	0.091
Cu_1878_pre_70_g2_x_09x25_f	179875.71	0.209	1.164	641.509	566.038	0.118
Cu_1878_pre_70_g2_x_10x25_f	179461.64	0.207	1.156	645.912	594.340	0.080
Cu_1878_pre_70_g2_x_11x25_f	178004.33	0.215	1.205	643.396	566.038	0.120
Medium grain c-shaped						
Cu_1878_pre_70_g2_c_25x02_f	279978.45	0.334	1.195	656.604	556.604	0.152
Cu_1878_pre_70_g2_c_24x02_f	269836.43	0.331	1.227	674.214	566.038	0.160
Cu_1878_pre_70_g2_c_23x02_f	274471.86	0.331	1.206	681.132	566.667	0.168
Cu_1878_pre_70_g2_c_22x02_f	261006.52	0.326	1.250	650.314	563.522	0.133
Cu_1878_pre_70_g2_c_21x02_f	264749.28	0.317	1.199	679.245	594.340	0.125
Cu_1878_pre_70_g2_c_20x02_f	253034.33	0.311	1.228	685.535	583.648	0.149
Cu_1878_pre_70_g2_c_19x02_f	248804.90	0.304	1.222	674.214	625.786	0.072
Cu_1878_pre_70_g2_c_18x02_f	249912.68	0.314	1.255	698.742	589.937	0.156
Cu_1878_pre_70_g2_c_17x02_f	246817.91	0.304	1.233	654.717	610.063	0.068
Cu_1878_pre_70_g2_c_16x02_f	242486.31	0.301	1.243	701.258	612.579	0.126
Cu_1878_pre_70_g2_c_15x02_f	264496.54	0.318	1.201	674.214	581.132	0.138
Cu_1878_pre_70_g2_c_14x02_f	265733.37	0.325	1.223	714.465	616.981	0.136
Cu_1878_pre_70_g2_c_25x03_f	283748.10	0.340	1.199	674.214	592.453	0.121
Cu_1878_pre_70_g2_c_24x03_f	269890.20	0.322	1.195	676.730	567.925	0.161
Cu_1878_pre_70_g2_c_23x03_f	269236.83	0.330	1.226	689.937	605.660	0.122
Cu_1878_pre_70_g2_c_22x03_f	281879.41	0.329	1.169	701.258	616.981	0.120
Cu_1878_pre_70_g2_c_14x03_f	269895.58	0.319	1.180	685.535	616.981	0.100
Cu_1878_pre_70_g2_c_25x04_f	276528.76	0.339	1.227	694.340	559.119	0.195
Cu_1878_pre_70_g2_c_24x04_f	270989.91	0.336	1.240	689.937	579.245	0.160
Cu_1878_pre_70_g2_c_23x04_f	265709.17	0.327	1.231	689.937	610.063	0.116

Cu_1878_pre_70_g2_c_22x04_f	260823.69	0.321	1.232	696.855	576.730	0.172
Cu_1878_pre_70_g2_c_21x04_f	260818.31	0.332	1.273	683.648	552.201	0.192
Cu_1878_pre_70_g2_c_20x04_f	263598.49	0.327	1.239	689.937	583.648	0.154
Cu_1878_pre_70_g2_c_19x04_f	247498.16	0.323	1.304	707.547	581.132	0.179
Cu_1878_pre_70_g2_c_18x04_f	259167.41	0.322	1.241	694.340	605.660	0.128
Cu_1878_pre_70_g2_c_17x04_f	261095.25	0.320	1.227	711.950	589.937	0.171
Cu_1878_pre_70_g2_c_16x04_f	260665.05	0.327	1.255	679.245	570.440	0.160
Cu_1878_pre_70_g2_c_15x04_f	263246.26	0.328	1.247	701.258	567.925	0.190
Cu_1878_pre_70_g2_c_14x04_f	266819.63	0.327	1.227	703.145	581.132	0.174
Cu_1878_pre_70_g2_c_25x05_f	265534.40	0.331	1.246	732.075	579.245	0.209
Cu_1878_pre_70_g2_c_24x05_f	261700.22	0.329	1.259	731.447	588.050	0.196
Cu_1878_pre_70_g2_c_23x05_f	267749.94	0.324	1.211	705.660	579.245	0.179
Cu_1878_pre_70_g2_c_22x05_f	260302.06	0.327	1.258	681.132	570.440	0.163
Cu_1878_pre_70_g2_c_21x05_f	253582.84	0.314	1.239	633.333	599.371	0.054
Cu_1878_pre_70_g2_c_20x05_f	257745.05	0.324	1.257	710.063	585.535	0.175
Cu_1878_pre_70_g2_c_19x05_f	262590.20	0.331	1.260	701.258	579.245	0.174
Cu_1878_pre_70_g2_c_18x05_f	255198.79	0.322	1.260	701.258	585.535	0.165
Cu_1878_pre_70_g2_c_17x05_f	266392.12	0.327	1.227	698.742	588.050	0.158
Cu_1878_pre_70_g2_c_16x05_f	273641.03	0.329	1.202	692.453	566.038	0.183
Cu_1878_pre_70_g2_c_15x05_f	266007.62	0.326	1.227	692.453	567.925	0.180
Cu_1878_pre_70_g2_c_14x05_f	252160.48	0.300	1.189	765.409	683.648	0.107
Cu_1878_pre_70_g3_c_02x01_f	244634.63	0.313	1.279	703.145	623.270	0.114
Cu_1878_pre_70_g3_c_03x01_f	248952.79	0.289	1.162	677.987	603.774	0.109
Cu_1878_pre_70_g3_c_04x01_f	236993.16	0.299	1.260	676.730	594.340	0.122
Cu_1878_pre_70_g3_c_05x01_f	223474.05	0.282	1.261	679.245	643.396	0.053
Cu_1878_pre_70_g3_c_06x01_f	233949.48	0.293	1.254	674.214	612.579	0.091
Cu_1878_pre_70_g3_c_07x01_f	225366.94	0.287	1.274	685.535	608.176	0.113
Cu_1878_pre_70_g3_c_08x01_f	234409.25	0.304	1.296	672.327	579.245	0.138
Cu_1878_pre_70_g3_c_09x01_f	236181.15	0.308	1.303	676.730	579.245	0.144
Cu_1878_pre_70_g3_c_10x01_f	240262.70	0.303	1.260	681.132	592.453	0.130
Cu_1878_pre_70_g3_c_11x01_f	234226.42	0.304	1.299	667.925	572.327	0.143
Cu_1878_pre_70_g3_c_12x01_f	241098.90	0.306	1.269	672.327	589.937	0.123
Cu_1878_pre_70_g3_c_01x02_f	261842.73	0.320	1.224	674.214	579.245	0.141
Cu_1878_pre_70_g3_c_02x02_f	259775.07	0.322	1.238	679.245	563.522	0.170
Cu_1878_pre_70_g3_c_03x02_f	253512.93	0.314	1.237	705.660	574.843	0.185
Cu_1878_pre_70_g3_c_04x02_f	260033.19	0.318	1.224	672.327	538.994	0.198
Cu_1878_pre_70_g3_c_05x02_f	257425.09	0.320	1.243	652.201	541.509	0.170
Cu_1878_pre_70_g3_c_06x02_f	255013.26	0.322	1.262	652.201	505.660	0.225
Cu_1878_pre_70_g3_c_07x02_f	247207.78	0.318	1.287	667.925	567.925	0.150
Cu_1878_pre_70_g3_c_08x02_f	250025.60	0.317	1.267	670.440	545.912	0.186
Cu_1878_pre_70_g3_c_09x02_f	257898.31	0.315	1.222	694.340	550.314	0.207
Cu_1878_pre_70_g3_c_10x02_f	258403.80	0.318	1.230	694.340	570.440	0.178
Medium grain hollow						
Cu_1878_pre_70_g2_h_25x24_f	310866.99	0.359	1.153	676.730	582.390	0.139
Cu_1878_pre_70_g2_h_24x24_f	279429.94	0.334	1.195	685.535	630.189	0.081
Cu_1878_pre_70_g2_h_23x24_f	285856.09	0.343	1.199	665.409	581.132	0.127
Cu_1878_pre_70_g2_h_22x24_f	264340.59	0.315	1.193	679.245	636.478	0.063
Cu_1878_pre_70_g2_h_21x24_f	284455.24	0.336	1.180	667.925	559.119	0.163
Cu_1878_pre_70_g2_h_20x24_f	279147.62	0.337	1.207	674.214	554.717	0.177
Cu_1878_pre_70_g2_h_19x24_f	285124.75	0.339	1.190	707.547	570.440	0.194
Cu_1878_pre_70_g2_h_18x24_f	270215.54	0.323	1.195	692.453	614.465	0.113
Cu_1878_pre_70_g2_h_17x24_f	278867.99	0.324	1.161	705.660	623.270	0.117
Cu_1878_pre_70_g2_h_16x24_f	277426.81	0.337	1.216	698.742	599.371	0.142
Cu_1878_pre_70_g2_h_15x24_f	265300.48	0.328	1.237	703.145	612.579	0.129

Cu_1878_pre_70_g2_h_14x24_f	275006.92	0.330	1.201	685.535	603.774	0.119
Cu_1878_pre_70_g2_h_13x24_f	286248.65	0.339	1.185	721.384	594.340	0.176
Cu_1878_pre_70_g2_h_25x23_f	286052.37	0.354	1.239	689.937	583.648	0.154
Cu_1878_pre_70_g2_h_23x23_f	285361.36	0.349	1.224	694.340	581.132	0.163
Cu_1878_pre_70_g2_h_21x23_f	278120.51	0.340	1.223	694.340	589.937	0.150
Cu_1878_pre_70_g2_h_20x23_f	280473.18	0.334	1.189	705.660	572.327	0.189
Cu_1878_pre_70_g2_h_19x23_f	268973.33	0.336	1.251	703.145	570.440	0.189
Cu_1878_pre_70_g2_h_25x22_f	311770.41	0.358	1.148	705.660	556.604	0.211
Cu_1878_pre_70_g2_h_24x22_f	291618.12	0.349	1.198	699.371	559.119	0.201
Cu_1878_pre_70_g2_h_23x22_f	289980.66	0.348	1.200	721.384	567.925	0.213
Cu_1878_pre_70_g2_h_22x22_f	305376.53	0.342	1.121	672.327	559.119	0.168
Cu_1878_pre_70_g2_h_21x22_f	295116.20	0.343	1.164	672.327	550.314	0.181
Cu_1878_pre_70_g2_h_20x22_f	281634.73	0.338	1.202	676.730	543.396	0.197
Cu_1878_pre_70_g2_h_19x22_f	278475.43	0.322	1.158	703.145	625.786	0.110
Cu_1878_pre_70_g2_h_18x22_f	287439.77	0.343	1.194	679.245	567.925	0.164
Cu_1878_pre_70_g2_h_17x22_f	278289.91	0.342	1.228	685.535	583.648	0.149
Cu_1878_pre_70_g2_h_16x22_f	280451.67	0.338	1.204	674.214	576.730	0.145
Cu_1878_pre_70_g2_h_15x22_f	290722.76	0.346	1.191	692.453	574.843	0.170
Cu_1878_pre_70_g2_h_13x22_f	290991.63	0.343	1.180	716.352	594.340	0.170
Cu_1878_pre_70_g2_h_25x21_f	282247.77	0.348	1.231	679.245	574.843	0.154
Cu_1878_pre_70_g2_h_24x21_f	282669.90	0.350	1.238	688.050	566.038	0.177
Cu_1878_pre_70_g2_h_23x21_f	275770.53	0.342	1.239	698.742	561.635	0.196
Cu_1878_pre_70_g2_h_22x21_f	265486.00	0.334	1.258	676.730	570.440	0.157
Cu_1878_pre_70_g2_h_21x21_f	265031.60	0.330	1.246	685.535	545.912	0.204
Cu_1878_pre_70_g2_h_20x21_f	278026.41	0.331	1.191	683.648	561.635	0.178
Cu_1878_pre_70_g2_h_19x21_f	270075.73	0.333	1.234	710.063	556.604	0.216
Cu_1878_pre_70_g2_h_18x21_f	268336.10	0.327	1.219	710.063	583.648	0.178
Cu_1878_pre_70_g2_h_17x21_f	270785.56	0.336	1.242	689.937	567.925	0.177
Cu_1878_pre_70_g2_h_16x21_f	276604.05	0.339	1.227	674.214	556.604	0.174
Cu_1878_pre_70_g2_h_15x21_f	277211.71	0.340	1.226	692.453	559.119	0.193
Cu_1878_pre_70_g2_h_14x21_f	269699.30	0.331	1.228	693.082	603.774	0.129
Cu_1878_pre_70_g2_h_13x21_f	295194.17	0.335	1.135	694.340	561.635	0.191
Cu_1878_pre_70_g2_h_25x19_f	273138.23	0.339	1.241	688.050	572.327	0.168
Cu_1878_pre_70_g2_h_24x19_f	266948.69	0.336	1.258	696.855	562.893	0.192
Cu_1878_pre_70_g2_h_23x19_f	271288.36	0.342	1.259	689.937	547.799	0.206
Cu_1878_pre_70_g2_h_22x19_f	275595.76	0.345	1.252	703.145	566.038	0.195
Cu_1878_pre_70_g2_h_21x19_f	274009.39	0.341	1.244	701.258	588.050	0.161
Cu_1878_pre_70_g2_h_20x19_f	268782.43	0.340	1.264	748.428	588.050	0.214
Cu_1878_pre_70_g2_h_19x19_f	278472.74	0.343	1.232	696.855	513.836	0.263
Cu_1878_pre_70_g2_h_18x19_f	271769.65	0.340	1.253	665.409	591.824	0.111
Cu_1878_pre_70_g2_h_17x19_f	279682.69	0.343	1.226	689.937	579.245	0.160
Cu_1878_pre_70_g2_h_16x19_f	281008.25	0.339	1.207	685.535	561.635	0.181
Cu_1878_pre_70_g2_h_15x19_f	279462.21	0.343	1.226	732.075	579.245	0.209
Cu_1878_pre_70_g2_h_14x19_f	262178.82	0.344	1.312	631.447	588.050	0.069
Cu_1878_pre_70_g2_h_25x18_f	271293.74	0.336	1.238	674.214	605.660	0.102
Cu_1878_pre_70_g2_h_24x18_f	260027.81	0.334	1.285	688.050	618.868	0.101
Cu_1878_pre_70_g2_h_22x18_f	266849.21	0.342	1.283	679.245	601.258	0.115
Cu_1878_pre_70_g2_h_21x18_f	266168.95	0.337	1.267	676.730	612.579	0.095
Cu_1878_pre_70_g2_h_20x18_f	261350.68	0.335	1.280	694.340	599.371	0.137
Cu_1878_pre_70_g2_h_19x18_f	262907.48	0.332	1.262	694.340	621.384	0.105
Cu_1878_pre_70_g2_h_18x18_f	260968.88	0.337	1.291	707.547	610.063	0.138
Cu_1878_pre_70_g2_h_17x18_f	262544.50	0.328	1.248	696.855	603.774	0.134
Cu_1878_pre_70_g2_h_15x18_f	275122.54	0.344	1.251	681.132	566.038	0.169
Cu_1878_pre_70_g2_h_14x18_f	269072.82	0.326	1.212	701.258	625.786	0.108

Cu_1878_pre_70_g2_h_13x18_f	278026.41	0.336	1.209	696.855	594.340	0.147
Cu_1878_pre_70_g2_h_25x17_f	275708.69	0.334	1.213	689.937	576.730	0.164
Cu_1878_pre_70_g2_h_24x17_f	271772.34	0.334	1.229	698.742	603.774	0.136
Cu_1878_pre_70_g2_h_23x17_f	266534.62	0.339	1.273	688.050	599.371	0.129
Cu_1878_pre_70_g2_h_22x17_f	263243.57	0.325	1.236	674.214	585.535	0.132
Cu_1878_pre_70_g2_h_21x17_f	262856.39	0.338	1.286	665.409	561.635	0.156
Cu_1878_pre_70_g2_h_20x17_f	254370.65	0.322	1.266	665.409	652.201	0.020
Cu_1878_pre_70_g2_h_19x17_f	256548.55	0.338	1.319	718.868	603.774	0.160
Cu_1878_pre_70_g2_h_18x17_f	261264.64	0.334	1.279	683.648	579.245	0.153
Cu_1878_pre_70_g2_h_17x17_f	255309.03	0.333	1.306	688.050	592.453	0.139
Cu_1878_pre_70_g2_h_16x17_f	267255.21	0.339	1.268	707.547	592.453	0.163
Cu_1878_pre_70_g2_h_15x17_f	263724.86	0.329	1.249	707.547	583.648	0.175
Cu_1878_pre_70_g2_h_14x17_f	271301.80	0.341	1.255	725.786	612.579	0.156
Cu_1878_pre_70_g2_h_13x17_f	272070.79	0.344	1.263	679.245	588.050	0.134
Large grain solid core						
Cu_1870_g3_s_25x02_f	309151.55	0.219	0.709	889.937	778.616	0.125
Cu_1870_g3_s_24x02_f	307941.61	0.218	0.708	854.088	794.340	0.070
Cu_1870_g3_s_23x02_f	287829.64	0.226	0.785	883.019	761.006	0.138
Cu_1870_g3_s_22x02_f	306774.69	0.200	0.653	862.893	785.535	0.090
Cu_1870_g3_s_21x02_f	303338.44	0.191	0.630	883.019	811.950	0.080
Cu_1870_g3_s_20x02_f	281632.04	0.195	0.691	849.686	767.925	0.096
Cu_1870_g3_s_19x02_f	301596.12	0.214	0.710	905.031	798.742	0.117
Cu_1870_g3_s_18x02_f	302443.08	0.211	0.699	862.893	710.063	0.177
Cu_1870_g3_s_17x02_f	302779.18	0.221	0.729	869.811	738.994	0.150
Cu_1870_g3_s_16x02_f	297764.63	0.226	0.760	907.547	774.214	0.147
Cu_1870_g3_s_15x02_f	287676.39	0.221	0.768	918.868	774.214	0.157
Cu_1870_g3_s_14x02_f	272103.06	0.197	0.723	867.296	836.478	0.036
Cu_1870_g3_s_13x02_f	298103.42	0.216	0.724	867.296	781.132	0.099
Cu_1870_g3_s_25x03_f	324525.91	0.199	0.612	829.560	732.075	0.118
Cu_1870_g3_s_24x03_f	320245.40	0.212	0.661	854.088	747.799	0.124
Cu_1870_g3_s_23x03_f	299757.01	0.218	0.726	865.409	793.711	0.083
Cu_1870_g3_s_22x03_f	296404.12	0.221	0.747	878.616	785.535	0.106
Cu_1870_g3_s_21x03_f	292465.08	0.219	0.750	856.604	734.591	0.142
Cu_1870_g3_s_20x03_f	299402.09	0.212	0.710	838.994	785.535	0.064
Cu_1870_g3_s_19x03_f	295393.14	0.220	0.745	843.396	783.648	0.071
Cu_1870_g3_s_18x03_f	310649.20	0.211	0.679	843.396	774.214	0.082
Cu_1870_g3_s_17x03_f	295148.46	0.219	0.742	852.830	791.824	0.072
Cu_1870_g3_s_16x03_f	302717.34	0.225	0.744	832.075	772.327	0.072
Cu_1870_g3_s_15x03_f	305459.88	0.199	0.650	836.478	774.214	0.074
Cu_1870_g3_s_14x03_f	308683.71	0.216	0.700	852.201	747.799	0.123
Cu_1870_g3_s_13x03_f	304422.02	0.228	0.748	865.409	769.811	0.110
Cu_1870_g3_s_24x04_f	303550.86	0.210	0.692	861.006	752.201	0.126
Cu_1870_g3_s_23x04_f	296750.97	0.192	0.648	847.799	759.119	0.105
Cu_1870_g3_s_22x04_f	317010.82	0.216	0.681	827.673	743.396	0.102
Cu_1870_g3_s_21x04_f	314128.46	0.192	0.611	881.132	754.088	0.144
Cu_1870_g3_s_20x04_f	293086.18	0.224	0.765	834.591	725.786	0.130
Cu_1870_g3_s_19x04_f	308092.18	0.225	0.729	859.119	785.535	0.086
Cu_1870_g3_s_18x04_f	302572.15	0.214	0.708	869.811	794.340	0.087
Cu_1870_g3_s_17x04_f	317411.44	0.202	0.635	861.006	739.623	0.141
Cu_1870_g3_s_16x04_f	290972.81	0.219	0.751	862.893	761.006	0.118
Cu_1870_g3_s_15x04_f	303731.00	0.224	0.737	843.396	756.604	0.103
Cu_1870_g3_s_14x04_f	304013.32	0.216	0.711	865.409	754.088	0.129
Cu_1870_g3_s_13x04_f	314096.19	0.201	0.641	869.811	805.660	0.074
Cu_1870_g3_s_25x06_f	297417.78	0.198	0.666	840.881	756.604	0.100

Cu_1870_g3_s_24x06_f	279784.86	0.195	0.695	869.811	781.132	0.102
Cu_1870_g3_s_13x06_f	369990.25	0.212	0.572	852.201	647.799	0.240
Cu_1870_g3_s_25x07_f	293088.87	0.215	0.733	852.201	810.063	0.049
Cu_1870_g3_s_24x07_f	282675.28	0.186	0.659	794.340	787.421	0.009
Cu_1870_g3_s_23x07_f	291489.05	0.206	0.706	845.283	778.616	0.079
Cu_1870_g3_s_22x07_f	304228.42	0.215	0.707	889.937	789.937	0.112
Cu_1870_g3_s_21x07_f	303083.01	0.225	0.741	874.214	807.547	0.076
Cu_1870_g3_s_20x07_f	299627.95	0.221	0.739	845.283	789.937	0.065
Cu_1870_g3_s_19x07_f	292112.85	0.192	0.656	869.811	805.660	0.074
Cu_1870_g3_s_18x07_f	285595.28	0.222	0.778	871.698	772.327	0.114
Cu_1870_g3_s_17x07_f	303206.69	0.220	0.725	849.686	843.396	0.007
Cu_1870_g3_s_16x07_f	292774.28	0.220	0.750	825.157	796.226	0.035
Large grain c-shaped						
Cu_1870_g3_c_01x02_f	273616.83	0.174	0.636	732.075	647.799	0.115
Cu_1870_g3_c_02x02_f	244255.51	0.170	0.697	721.384	638.994	0.114
Cu_1870_g3_c_03x02_f	254198.57	0.185	0.726	732.075	625.786	0.145
Cu_1870_g3_c_04x02_f	258169.87	0.166	0.642	716.352	632.075	0.118
Cu_1870_g3_c_05x02_f	258169.87	0.174	0.676	716.352	652.201	0.090
Cu_1870_g3_c_06x02_f	256508.22	0.161	0.629	723.270	681.132	0.058
Cu_1870_g3_c_07x02_f	252948.29	0.159	0.629	736.478	685.535	0.069
Cu_1870_g3_c_08x02_f	245629.47	0.171	0.698	721.384	650.314	0.099
Cu_1870_g3_c_09x02_f	253303.21	0.163	0.643	740.881	661.006	0.108
Cu_1870_g3_c_10x02_f	256933.04	0.188	0.731	736.478	654.717	0.111
Cu_1870_g3_c_11x02_f	263144.09	0.169	0.641	740.881	656.604	0.114
Cu_1870_g3_c_12x02_f	250673.60	0.183	0.731	754.088	674.214	0.106
Cu_1870_g3_c_01x03_f	236183.84	0.179	0.756	733.962	630.189	0.141
Cu_1870_g3_c_02x03_f	233970.99	0.188	0.805	759.119	625.786	0.176
Cu_1870_g3_c_04x03_f	236159.64	0.159	0.672	732.075	647.799	0.115
Cu_1870_g3_c_05x03_f	254053.37	0.183	0.720	734.591	618.868	0.158
Cu_1870_g3_c_06x03_f	223388.00	0.188	0.844	715.723	625.786	0.126
Cu_1870_g3_c_08x03_f	244545.90	0.171	0.699	736.478	641.509	0.129
Cu_1870_g3_c_09x03_f	245046.01	0.157	0.642	736.478	679.245	0.078
Cu_1870_g3_c_10x03_f	238049.84	0.174	0.731	725.157	676.730	0.067
Cu_1870_g3_c_12x03_f	248143.47	0.170	0.687	740.881	676.730	0.087
Cu_1870_g3_c_01x04_f	245734.33	0.168	0.685	740.881	701.258	0.053
Cu_1870_g3_c_02x04_f	241184.94	0.155	0.644	725.786	661.006	0.089
Cu_1870_g3_c_03x04_f	239891.65	0.176	0.734	707.547	623.270	0.119
Cu_1870_g3_c_04x04_f	254623.39	0.193	0.758	730.189	638.994	0.125
Cu_1870_g3_c_05x04_f	249302.33	0.156	0.626	721.384	672.327	0.068
Cu_1870_g3_c_06x04_f	233677.91	0.188	0.805	730.189	641.509	0.121
Cu_1870_g3_c_07x04_f	238625.24	0.182	0.762	727.673	670.440	0.079
Cu_1870_g3_c_08x04_f	243050.95	0.191	0.788	725.786	618.868	0.147
Cu_1870_g3_c_09x04_f	250678.97	0.183	0.731	740.881	664.151	0.104
Cu_1870_g3_c_10x04_f	248823.73	0.182	0.730	752.201	652.201	0.133
Cu_1870_g3_c_11x04_f	257110.50	0.179	0.698	725.786	650.314	0.104
Cu_1870_g3_c_12x04_f	255927.44	0.179	0.700	772.327	674.214	0.127
Cu_1870_g3_c_01x05_f	230177.14	0.173	0.750	707.547	636.478	0.100
Cu_1870_g3_c_02x05_f	227063.55	0.164	0.723	721.384	689.937	0.044
Cu_1870_g3_c_03x05_f	236310.21	0.174	0.738	747.799	674.214	0.098
Cu_1870_g3_c_04x05_f	238883.36	0.191	0.798	714.465	647.799	0.093
Cu_1870_g3_c_05x05_f	247022.25	0.187	0.758	696.855	632.075	0.093
Cu_1870_g3_c_06x05_f	227886.31	0.156	0.683	679.245	667.925	0.017
Cu_1870_g3_c_07x05_f	241042.44	0.183	0.760	714.465	634.591	0.112
Cu_1870_g3_c_08x05_f	229241.45	0.180	0.784	723.270	614.465	0.150

Cu_1870_g3_c_09x05_f	230688.00	0.177	0.769	696.855	634.591	0.089
Cu_1870_g3_c_10x05_f	224412.42	0.155	0.691	701.258	663.522	0.054
Cu_1870_g3_c_11x05_f	218991.87	0.162	0.739	721.384	623.270	0.136
Cu_1870_g3_c_12x05_f	231588.74	0.186	0.802	721.384	638.994	0.114
Cu_1870_g3_c_01x06_f	234137.69	0.186	0.795	711.950	618.868	0.131
Cu_1870_g3_c_02x06_f	235820.86	0.183	0.776	683.648	614.465	0.101
Cu_1870_g3_c_03x06_f	242265.83	0.178	0.735	727.673	614.465	0.156
Cu_1870_g3_c_04x06_f	251380.74	0.170	0.675	710.063	636.478	0.104
Cu_1870_g3_c_05x06_f	246785.64	0.180	0.731	689.937	608.176	0.119
Cu_1870_g3_c_06x06_f	227219.50	0.180	0.791	679.245	625.786	0.079
Cu_1870_g3_c_08x06_f	247689.07	0.175	0.705	692.453	614.465	0.113
Cu_1870_g3_c_09x06_f	231779.64	0.181	0.779	698.742	610.063	0.127
Cu_1870_g3_c_01x07_f	241695.81	0.175	0.722	705.660	663.522	0.060
Cu_1870_g3_c_02x07_f	245075.59	0.174	0.711	692.453	656.604	0.052
Cu_1870_g3_c_03x07_f	219190.84	0.179	0.818	685.535	643.396	0.061
Cu_1870_g3_c_04x07_f	246237.13	0.160	0.649	694.340	656.604	0.054
Cu_1870_g3_c_05x07_f	255403.13	0.156	0.609	696.855	665.409	0.045
Cu_1870_g3_c_06x07_f	223116.44	0.166	0.744	696.855	656.604	0.058
Cu_1870_g3_c_07x07_f	221226.24	0.168	0.758	692.453	634.591	0.084
Cu_1870_g3_c_08x07_f	237606.20	0.179	0.753	694.340	681.132	0.019
Cu_1870_g3_c_09x07_f	222742.70	0.154	0.692	710.692	685.535	0.035
Cu_1870_g3_c_10x07_f	230327.71	0.173	0.751	701.258	663.522	0.054
Cu_1870_g3_c_11x07_f	229219.94	0.176	0.767	704.403	679.245	0.036
Cu_1870_g3_c_12x07_f	215171.14	0.168	0.782	703.145	652.201	0.072
Large grain hollow						
Cu_1870_g3_h_01x24_f	281505.67	0.208	0.739	672.327	561.635	0.165
Cu_1870_g3_h_02x24_f	277792.48	0.199	0.716	669.811	567.925	0.152
Cu_1870_g3_h_03x24_f	267144.97	0.218	0.816	688.050	566.038	0.177
Cu_1870_g3_h_04x24_f	288655.10	0.212	0.735	665.409	583.648	0.123
Cu_1870_g3_h_05x24_f	268016.13	0.212	0.790	641.509	552.201	0.139
Cu_1870_g3_h_06x24_f	280591.49	0.186	0.664	667.925	561.635	0.159
Cu_1870_g3_h_07x24_f	290047.88	0.192	0.663	671.069	543.396	0.190
Cu_1870_g3_h_08x24_f	264265.30	0.221	0.835	641.509	556.604	0.132
Cu_1870_g3_h_09x24_f	268682.95	0.197	0.734	647.170	561.635	0.132
Cu_1870_g3_h_10x24_f	261132.89	0.202	0.775	667.925	567.925	0.150
Cu_1870_g3_h_11x24_f	282438.67	0.205	0.727	663.522	574.843	0.134
Cu_1870_g3_h_12x24_f	266131.31	0.204	0.768	664.780	581.132	0.126
Cu_1870_g3_h_13x24_f	273498.53	0.183	0.668	661.006	572.327	0.134
Cu_1870_g3_h_01x23_f	273834.62	0.212	0.775	614.465	541.509	0.119
Cu_1870_g3_h_02x23_f	278072.12	0.199	0.714	650.314	566.038	0.130
Cu_1870_g3_h_03x23_f	276749.24	0.208	0.752	661.006	530.189	0.198
Cu_1870_g3_h_04x23_f	267731.12	0.209	0.782	603.774	552.201	0.085
Cu_1870_g3_h_05x23_f	279739.15	0.196	0.702	614.465	545.912	0.112
Cu_1870_g3_h_06x23_f	266706.70	0.199	0.748	612.579	545.912	0.109
Cu_1870_g3_h_07x23_f	261468.99	0.210	0.805	623.270	574.843	0.078
Cu_1870_g3_h_09x23_f	268779.74	0.177	0.658	638.994	579.245	0.094
Cu_1870_g3_h_10x23_f	257944.02	0.215	0.833	647.799	538.994	0.168
Cu_1870_g3_h_11x23_f	267231.01	0.200	0.748	616.981	547.799	0.112
Cu_1870_g3_h_12x23_f	257290.65	0.199	0.775	636.478	563.522	0.115
Cu_1870_g3_h_13x23_f	265085.38	0.197	0.741	679.245	650.314	0.043
Cu_1870_g3_h_01x21_f	261194.73	0.194	0.741	652.201	556.604	0.147
Cu_1870_g3_h_02x21_f	276523.39	0.203	0.735	632.075	561.635	0.111
Cu_1870_g3_h_07x21_f	269605.19	0.194	0.719	627.673	542.138	0.136
Cu_1870_g3_h_08x21_f	287910.31	0.203	0.705	650.314	545.912	0.161

Cu_1870_g3_h_09x21_f	281075.47	0.199	0.710	645.912	572.327	0.114
Cu_1870_g3_h_10x21_f	270169.83	0.213	0.787	645.912	576.730	0.107
Cu_1870_g3_h_12x21_f	264915.99	0.218	0.824	645.912	576.730	0.107
Cu_1870_g3_h_13x21_f	270634.99	0.203	0.750	676.730	563.522	0.167
Cu_1870_g3_h_01x20_f	247791.24	0.195	0.785	627.673	541.509	0.137
Cu_1870_g3_h_02x20_f	270911.93	0.216	0.798	652.201	570.440	0.125
Cu_1870_g3_h_03x20_f	264838.01	0.216	0.815	647.799	528.302	0.184
Cu_1870_g3_h_05x20_f	278997.05	0.193	0.691	661.006	543.396	0.178
Cu_1870_g3_h_06x20_f	274138.45	0.210	0.767	621.384	534.591	0.140
Cu_1870_g3_h_07x20_f	285097.86	0.219	0.768	645.912	541.509	0.162
Cu_1870_g3_h_08x20_f	283645.93	0.203	0.715	632.075	534.591	0.154
Cu_1870_g3_h_10x20_f	274654.69	0.218	0.793	661.006	512.579	0.225
Cu_1870_g3_h_11x20_f	283425.45	0.197	0.696	643.396	521.384	0.190
Cu_1870_g3_h_12x20_f	271116.28	0.225	0.831	618.868	534.591	0.136
Cu_1870_g3_h_01x19_f	274617.05	0.208	0.756	627.673	550.314	0.123
Cu_1870_g3_h_02x19_f	271024.86	0.189	0.696	638.994	516.981	0.191
Cu_1870_g3_h_03x19_f	274676.20	0.214	0.779	663.522	505.660	0.238
Cu_1870_g3_h_04x19_f	275810.86	0.208	0.755	641.509	543.396	0.153
Cu_1870_g3_h_06x19_f	271360.96	0.195	0.719	665.409	537.107	0.193
Cu_1870_g3_h_08x19_f	276773.44	0.189	0.683	603.774	567.925	0.059
Cu_1870_g3_h_09x19_f	289803.20	0.198	0.682	650.314	567.925	0.127
Cu_1870_g3_h_10x19_f	285622.17	0.218	0.762	643.396	552.201	0.142
Cu_1870_g3_h_11x19_f	290948.61	0.198	0.679	667.925	559.119	0.163
Cu_1870_g3_h_13x19_f	265233.26	0.225	0.849	656.604	519.497	0.209
Large grain x-shaped						
Cu_1870_g3_x_25x24_f	177251.48	0.116	0.657	765.409	645.912	0.156
Cu_1870_g3_x_24x24_f	163743.12	0.123	0.751	734.591	669.811	0.088
Cu_1870_g3_x_23x24_f	162753.66	0.118	0.727	756.604	679.245	0.102
Cu_1870_g3_x_22x24_f	164603.53	0.104	0.630	769.811	661.006	0.141
Cu_1870_g3_x_21x24_f	163374.76	0.119	0.728	723.270	652.201	0.098
Cu_1870_g3_x_20x24_f	165740.88	0.123	0.740	747.799	669.811	0.104
Cu_1870_g3_x_19x24_f	170381.68	0.109	0.638	740.881	674.214	0.090
Cu_1870_g3_x_18x24_f	167563.86	0.110	0.654	710.063	696.855	0.019
Cu_1870_g3_x_17x24_f	159032.41	0.112	0.704	781.132	694.340	0.111
Cu_1870_g3_x_16x24_f	168943.19	0.102	0.602	723.270	679.245	0.061
Cu_1870_g3_x_15x24_f	167389.09	0.093	0.556	749.686	689.937	0.080
Cu_1870_g3_x_24x22_f	165754.32	0.100	0.603	707.547	645.912	0.087
Cu_1870_g3_x_22x22_f	183416.82	0.115	0.630	748.428	689.937	0.078
Cu_1870_g3_x_21x22_f	160296.13	0.086	0.536	752.201	652.201	0.133
Cu_1870_g3_x_19x22_f	164098.04	0.114	0.697	740.881	669.811	0.096
Cu_1870_g3_x_17x22_f	176146.40	0.104	0.588	759.119	698.742	0.080
Cu_1870_g3_x_16x22_f	163826.47	0.117	0.717	772.327	696.855	0.098
Cu_1870_g3_x_15x22_f	180824.85	0.100	0.554	738.994	685.535	0.072
Cu_1870_g3_x_14x22_f	165221.94	0.113	0.681	739.623	685.535	0.073
Cu_1870_g3_x_25x21_f	167641.83	0.118	0.706	723.270	594.340	0.178
Cu_1870_g3_x_24x21_f	170680.14	0.123	0.720	723.270	638.994	0.117
Cu_1870_g3_x_23x21_f	170053.65	0.116	0.683	725.786	618.868	0.147
Cu_1870_g3_x_22x21_f	174920.32	0.101	0.580	756.604	671.698	0.112
Cu_1870_g3_x_21x21_f	178759.88	0.092	0.516	763.522	688.050	0.099
Cu_1870_g3_x_19x21_f	170690.89	0.102	0.596	747.799	683.648	0.086
Cu_1870_g3_x_17x21_f	155079.92	0.111	0.716	718.868	661.006	0.080
Cu_1870_g3_x_16x21_f	156171.56	0.116	0.744	740.881	654.717	0.116
Cu_1870_g3_x_25x20_f	174925.70	0.099	0.566	738.994	683.648	0.075
Cu_1870_g3_x_24x20_f	181255.05	0.113	0.622	749.686	685.535	0.086

Cu_1870_g3_x_23x20_f	159731.48	0.106	0.666	740.881	645.912	0.128
Cu_1870_g3_x_22x20_f	171661.54	0.104	0.606	754.088	676.730	0.103
Cu_1870_g3_x_21x20_f	174186.29	0.116	0.668	740.881	630.189	0.149
Cu_1870_g3_x_18x20_f	177157.37	0.111	0.628	732.075	703.145	0.040
Cu_1870_g3_x_17x20_f	175310.19	0.113	0.643	730.818	672.327	0.080
Cu_1870_g3_x_16x20_f	173159.18	0.104	0.601	732.075	663.522	0.094
Cu_1870_g3_x_15x20_f	172605.29	0.115	0.668	723.270	634.591	0.123
Cu_1870_g3_x_25x19_f	176928.83	0.112	0.635	725.786	659.119	0.092
Cu_1870_g3_x_24x19_f	178716.86	0.117	0.652	732.075	618.868	0.155
Cu_1870_g3_x_23x19_f	170166.58	0.117	0.685	754.088	672.327	0.108
Cu_1870_g3_x_22x19_f	164337.34	0.112	0.683	745.283	669.811	0.101
Cu_1870_g3_x_21x19_f	184441.24	0.120	0.651	721.384	634.591	0.120
Cu_1870_g3_x_20x19_f	185215.60	0.109	0.588	732.075	685.535	0.064
Cu_1870_g3_x_18x19_f	166076.97	0.104	0.627	749.686	647.799	0.136
Cu_1870_g3_x_17x19_f	160164.38	0.111	0.693	774.214	638.994	0.175
Cu_1870_g3_x_16x19_f	173293.62	0.107	0.620	754.088	623.270	0.173
Cu_1870_g3_x_15x19_f	168408.13	0.099	0.588	747.799	679.245	0.092

Bibliography

[1] E. O. Hall, "The Deformation and Ageing of Mild Steel: III Discussion of Results," *Proc. Phys. Soc. Sect. B*, vol. 64, pp. 747–753, 2002.

[2] N. J. Petch, "The cleavage strength of polycrystals," *J. Iron Steel Inst.*, vol. 174, pp. 25–28, 1953.

[3] J. R. Weertman, "Hall-Petch strengthening in nanocrystalline metals," *Mater. Sci. Eng. A*, vol. 166, no. 1–2, pp. 161–167, Jul. 1993.

[4] a. H. Chokshi, a. Rosen, J. Karch, and H. Gleiter, "On the validity of the hall-petch relationship in nanocrystalline materials," *Scr. Metall.*, vol. 23, no. c, pp. 1679–1683, 1989.

[5] G. W. Nieman, J. R. Weertman, and R. W. Siegel, "Microhardness of nanocrystalline palladium and copper produced by inert-gas condensation," *Scr. Metall.*, vol. 23, no. 13, pp. 2013–2018, 1989.

[6] T. G. Nieh and J. Wadsworth, "Hall-petch relation in nanocrystalline solids," *Scr. Metall. Mater.*, vol. 25, no. 4, pp. 955–958, 1991.

[7] R. O. Scattergood, "Modified Model for Hall Petch relationship in nanocrystaline material," *Scr. Metall. Mater.*, vol. 27, no. c, 1992.

[8] V. Yamakov, D. Wolf, S. R. Phillpot, A. K. Mukherjee, and H. Gleiter, "Dislocation processes in the deformation of nanocrystalline aluminium by molecular-dynamics simulation.," *Nat. Mater.*, vol. 1, no. 1, pp. 45–48, 2002.

[9] R. a. Masumura, P. M. Hazzledine, and C. S. Pande, "Yield stress of fine grained materials," *Acta Mater.*, vol. 46, no. 13, pp. 4527–4534, 1998.

[10] H. Van Swygenhoven, M. Spaczer, and a. Caro, "Microscopic description of plasticity in computer generated metallic nanophase samples: A comparison between Cu and Ni," *Acta Mater.*, vol. 47, no. 10, pp. 3117–3126, 1999.

[11] V. Yamakov, D. Wolf, S. R. Phillpot, a K. Mukherjee, and H. Gleiter, "Deformation-mechanism map for nanocrystalline metals by molecular-dynamics simulation.," *Nat. Mater.*, vol. 3, no. 1, pp. 43–47, 2004.

[12] G. Fan, H. Choo, P. Liaw, and E. Lavernia, "A model for the inverse Hall–Petch relation of nanocrystalline materials," *Mater Sci Eng A*, vol. 409, no. 1–2, pp. 243–248, 2005.

[13] H. W. Song, S. R. Guo, and Z. Q. Hu, “Coherent polycrystal model for the inverse Hall-Petch relation in nanocrystalline materials,” *Nanostructured Mater.*, vol. 11, no. 2, pp. 203–210, 1999.

[14] G. I. Taylor, “The mechanism of plastic deformation of crystals. Part I. Theoretical,” in *Proceedings of the Royal Society of London. Series A, Containing Papers of a Mathematical and Physical Character*, 1934, pp. 362–387.

[15] H. Van Swygenhoven, “Grain boundaries and dislocations.,” *Science (80-.).*, no. March, pp. 66–67, 2002.

[16] C. Brandl, P. M. Derlet, and H. Van Swygenhoven, “Dislocation mediated plasticity in nanocrystalline Al: the strongest size,” *Model. Simul. Mater. Sci. Eng.*, vol. 19, no. 7, p. 074005, 2011.

[17] X. Li, Y. Wei, W. Yang, and H. Gao, “Competing grain-boundary- and dislocation-mediated mechanisms in plastic strain recovery in nanocrystalline aluminum.,” *Proc. Natl. Acad. Sci. U. S. A.*, vol. 106, no. 38, pp. 16108–16113, 2009.

[18] Y. T. Zhu, X. Z. Liao, and X. L. Wu, “Deformation twinning in nanocrystalline materials,” *Prog. Mater. Sci.*, vol. 57, no. 1, pp. 1–62, 2012.

[19] J. W. Christian and S. Mahajan, “Deformation twinning,” *Prog. Mater. Sci.*, vol. 39, no. 1–2, pp. 1–157, 1995.

[20] X. L. Wu and Y. T. Zhu, “Partial-dislocation-mediated processes in nanocrystalline Ni with nonequilibarium grain boundaries,” *Appl. Phys. Lett.*, vol. 89, no. 3, pp. 2004–2007, 2006.

[21] S. a. Dregia and J. P. Hirth, “A rebound mechanism for Lomer dislocation formation in strained layer structures,” *J. Appl. Phys.*, vol. 69, no. 4, pp. 2169–2175, 1991.

[22] L. Lu, “Ultrahigh Strength and High Electrical Conductivity in Copper,” *Science (80-.).*, vol. 304, no. 5669, pp. 422–426, 2004.

[23] X. Li, Y. Wei, L. Lu, K. Lu, and H. Gao, “Dislocation nucleation governed softening and maximum strength in nano-twinned metals.,” *Nature*, vol. 464, no. April, pp. 877–880, 2010.

[24] D. Tabor, “Indentation hardness: Fifty years on a personal view,” *Philos. Mag. A*, vol. 74, no. 5, pp. 1207–1212, 1996.

[25] A. P. Bulychev, S. I., Alekhin, V. P., Shorshorov, M. H., Ternovskii, "Determining Young's modulus from the indentor penetration diagram," *Ind. Lab.*, vol. 41, no. 9, pp. 1409–1412, 1975.

[26] W. C. Oliver and G. M. Pharr, "An improved technique for determining hardness and elastic modulus using load and displacement sensing indentation experiments," *J. Mater. Res.*, 1992.

[27] I. N. Sneddon, "The relation between load and penetration in the axisymmetric boussinesq problem for a punch of arbitrary profile," *Int. J. Eng. Sci.*, vol. 3, no. 1, pp. 47–57, 1965.

[28] R. a. Mirshams and P. Parakala, "Nanoindentation of nanocrystalline Ni with geometrically different indenters," *Mater. Sci. Eng. A*, vol. 372, no. 1–2, pp. 252–260, 2004.

[29] R. Saha and W. D. Nix, "Effects of the substrate on the determination of thin film mechanical properties by nanoindentation," *Acta Mater.*, vol. 50, no. 1, pp. 23–38, 2002.

[30] M. D. Uchic, D. M. Dimiduk, J. N. Florando, and W. D. Nix, "Sample dimensions influence strength and crystal plasticity.," *Science*, vol. 305, no. August, pp. 986–989, 2004.

[31] M. D. Uchic and D. M. Dimiduk, "A methodology to investigate size scale effects in crystalline plasticity using uniaxial compression testing," *Mater. Sci. Eng. A*, vol. 400–401, no. 1–2 SUPPL., pp. 268–278, 2005.

[32] S. Reyntjens and R. Puers, "A review of focused ion beam applications in microsystem technology," *J. Micromechanics Microengineering*, vol. 11, no. 4, pp. 287–300, 2001.

[33] J. R. Greer, W. C. Oliver, and W. D. Nix, "Size dependence of mechanical properties of gold at the micron scale in the absence of strain gradients," *Acta Mater.*, vol. 53, no. 6, pp. 1821–1830, 2005.

[34] G. Lee, J.-Y. Kim, A. S. Budiman, N. Tamura, M. Kunz, K. Chen, M. J. Burek, J. R. Greer, and T. Y. Tsui, "Fabrication, structure and mechanical properties of indium nanopillars," *Acta Mater.*, vol. 58, no. 4, pp. 1361–1368, 2010.

[35] M. J. Burek, S. Jin, M. C. Leung, Z. Jahed, J. Wu, A. S. Budiman, N. Tamura, M. Kunz, and T. Y. Tsui, "Grain boundary effects on the mechanical properties of bismuth nanostructures," *Acta Mater.*, vol. 59, no. 11, pp. 4709–4718, 2011.

[36] Z. Jahed, R. D. Evans, M. J. Burek, and T. Y. Tsui, "Mechanical properties of columnar submicron cobalt structures with various cross-sectional geometries," *Scr. Mater.*, 2012.

[37] B. B. Seo, Z. Jahed, M. J. Burek, and T. Y. Tsui, "Influence of grain size on the strength size dependence exhibited by sub-micron scale nickel structures with complex cross-sectional geometries," *Mater. Sci. Eng. A*, vol. 596, pp. 275–284, 2014.

[38] S. Jin, S. Xie, M. J. Burek, Z. Jahed, and T. Y. Tsui, "Microstructure and mechanical properties of sub-micron zinc structures," *J. Mater. Res.*, vol. 27, no. 16, pp. 2140–2147, 2012.

[39] S. Jin, M. J. Burek, R. D. Evans, Z. Jahed, M. C. Leung, N. D. Evans, and T. Y. Tsui, "Fabrication, microstructure, and mechanical properties of high strength cobalt sub-micron structures," *Mater. Sci. Eng. A*, vol. 552, pp. 104–111, 2012.

[40] F. D. Di Tolla and K. W. Jacobsen, "Softening of nanocrystalline metals at very small grain sizes," vol. 391, no. February, pp. 561–563, 1998.

[41] M. Karplus and G. a Petsko, "Molecular dynamics simulations in biology.," *Nature*, vol. 347, no. 6294, pp. 631–639, 1990.

[42] A. Warshel, "Computer simulations of enzyme catalysis: methods, progress, and insights.," *Annu. Rev. Biophys. Biomol. Struct.*, vol. 32, pp. 425–443, 2003.

[43] R. P. Feynman, "Simulating physics with computers," *Int. J. Theor. Phys.*, vol. 21, no. 6–7, pp. 467–488, 1982.

[44] S. Yip, *Handbook of Material Modeling*. Springer, 2005.

[45] M. S. Daw, S. M. Foiles, and M. I. Baskes, "The embedded-atom method: a review of theory and applications," *Mater. Sci. Reports*, vol. 9, no. 7–8, pp. 251–310, 1993.

[46] M. S. Daw, I. Baskes, S. N. Laboratories, and I. Introduction, "and Other Defects in Metals," *Phys. Rev. B*, vol. 29, no. 12, 1984.

[47] M. S. Daw and M. I. Baskes, "Semiempirical, quantum mechanical calculation of hydrogen embrittlement in metals," *Phys. Rev. Lett.*, vol. 50, no. 17, pp. 1285–1288, 1983.

[48] S. M. Foiles, "Calculation of the atomic structure of the $\sum = 13$ ($\theta = 22.6°$) [001] twist boundary in gold," *Acta Metall.*, vol. 37, no. 10, pp. 2815–2821, 1989.

[49] I. Majid, P. D. Bristowe, and R. W. Balluffi, "Structures of [001] twist boundaries in gold. II. Results obtained by x-ray diffraction and computer simulation," *Phys. Rev. B*, vol. 40, no. 5, pp. 2779–2792, 1989.

[50] S. J. Zhou, "Large-Scale Molecular Dynamics Simulations of Dislocation Intersection in Copper," *Science (80-.).*, vol. 279, no. 5356, pp. 1525–1527, 1998.

[51] C. L. Kelchner, S. J. Plimpton, and J. C. Hamilton, "Dislocation nucleation and defect structure during surface indentation," *Phys. Rev. B - Condens. Matter Mater. Phys.*, vol. 58, no. 17, pp. 11085–11088, 1998.

[52] J. a Zimmerman, H. Gao, and F. F. Abraham, "Generalized stacking fault energies for embedded atom FCC metals," *Model. Simul. Mater. Sci. Eng.*, vol. 8, no. 2, pp. 103–115, 2000.

[53] R. Cao, Y. Deng, and C. Deng, "ScienceDirect Ultrahigh plastic flow in Au nanotubes enabled by surface stress facilitated reconstruction," *ACTA Mater.*, vol. 86, pp. 15–22, 2015.

[54] C. Deng and F. Sansoz, "Near-Ideal Strength in Gold Nanowires Design," vol. 3, no. 10, pp. 3001–3008, 2009.

[55] S. Nosé, "A molecular dynamics method for simulations in the canonical ensemble," *Mol. Phys.*, vol. 52, no. 2, pp. 255–268, 1984.

[56] S. Nose, S. Nosé, and S. Nosé, "A unified formulation of the constant temperature molecular dynamics methods," *J. Chem. Phys.*, vol. 81, no. 1, pp. 511–519, 1984.

[57] W. G. Hoover, "Constant-pressure equations of motion," *Phys. Rev. A*, vol. 34, no. 3, pp. 2499–2500, 1986.

[58] W. G. Hoover, "Canonical dynamics: Equilibrium phase-space distributions," *Phys. Rev. A*, vol. 31, no. 3, pp. 1695–1697, 1985.

[59] H. C. Andersen, "Molecular dynamics simulations at constant pressure and/or temperature," *J. Chem. Phys.*, vol. 72, no. 4, pp. 2384–2393, 1980.

[60] T. Q. Yu and M. E. Tuckerman, "Constrained molecular dynamics in the isothermal-isobaric ensemble and its adaptation for adiabatic free energy dynamics," *Eur. Phys. J. Spec. Top.*, vol. 200, no. 1, pp. 183–209, 2011.

[61] R. Clausius, "On a mechanical theory applicable to heat," vol. xxiv, pp. 122–127, 1870.

[62] J. Diao, K. Gall, and M. L. Dunn, "Atomistic simulation of the structure and elastic properties of gold nanowires," *J. Mech. Phys. Solids*, vol. 52, no. 9, pp. 1935–1962, Sep. 2004.

[63] M. Zhou, "A new look at the atomic level virial stress: on continuum-molecular system equivalence," *Proc. R. Soc. A Math. Phys. Eng. Sci.*, vol. 459, no. 2037, pp. 2347–2392, 2003.

[64] R. Cao and C. Deng, "The ultra-small strongest grain size in nanocrystalline Ni nanowires," *Scr. Mater.*, vol. 94, pp. 9–12, Jan. 2015.

[65] S. Traiviratana, E. M. Bringa, D. J. Benson, and M. a. Meyers, "Void growth in metals: Atomistic calculations," *Acta Mater.*, vol. 56, no. 15, pp. 3874–3886, Sep. 2008.

[66] B. Boots, "Spatial Tessellations," *Geogr. Inf. Syst.*, no. 1, pp. 503–526, 2000.

[67] C. B. Barber, D. P. Dobkin, and H. Huhdanpaa, "The quickhull algorithm for convex hulls," *ACM Trans. Math. Softw.*, vol. 22, no. 4, pp. 469–483, 1996.

[68] J. D. Honeycutt and H. C. Andemen, "Molecular Dynamics Study of Melting and Freezing of Small Lennard- Jones Clusters," *J. Phys. Chem.*, vol. 91, no. 24, pp. 4950–4963, 1987.

[69] G. J. Ackland and a. P. Jones, "Applications of local crystal structure measures in experiment and simulation," *Phys. Rev. B - Condens. Matter Mater. Phys.*, vol. 73, no. 5, pp. 1–7, 2006.

[70] A. Stukowski, "Structure identification methods for atomistic simulations of crystalline materials," *Model. Simul. Mater. Sci. Eng.*, vol. 20, p. 045021, 2012.

[71] F. Shimizu, S. Ogata, and J. Li, "Theory of Shear Banding in Metallic Glasses and Molecular Dynamics Calculations," *Mater. Trans.*, vol. 48, no. 11, pp. 2923–2927, 2007.

[72] M. L. Falk and J. S. Langer, "Dynamics of Viscoplastic Deformation in Amorphous Solids," vol. 57, no. 6, p. 16, 1997.

[73] D. Jang, C. Cai, and J. R. Greer, "Influence of homogeneous interfaces on the strength of 500 nm diameter Cu nanopillars.," *Nano Lett.*, vol. 11, no. 4, pp. 1743–6, Apr. 2011.

[74] X. W. Gu, C. N. Loynachan, Z. Wu, Y.-W. Zhang, D. J. Srolovitz, and J. R. Greer, "Size-dependent deformation of nanocrystalline Pt nanopillars.," *Nano Lett.*, vol. 12, no. 12, pp. 6385–92, Dec. 2012.

[75] A. T. Jennings, M. J. Burek, and J. R. Greer, "Microstructure versus Size: Mechanical Properties of Electroplated Single Crystalline Cu Nanopillars," *Phys. Rev. Lett.*, vol. 104, no. 13, p. 135503, Apr. 2010.

[76] B. E. Schuster, Q. Wei, H. Zhang, and K. T. Ramesh, "Microcompression of nanocrystalline nickel," *Appl. Phys. Lett.*, vol. 88, no. 10, pp. 1–4, 2006.

[77] J. Y. Kim and J. R. Greer, "Tensile and compressive behavior of gold and molybdenum single crystals at the nano-scale," *Acta Mater.*, vol. 57, no. 17, pp. 5245–5253, 2009.

[78] S. Jin, B. B. Seo, Z. Jahed, and T. Y. Tsui, "Fabrication and mechanical properties of sub-micron nanocrystalline rhenium–nickel alloy pillars," *Mater. Lett.*, vol. 149, pp. 113–115, 2015.

[79] T. Y. Tsui, Z. Jahed, R. D. Evans, and M. J. Burek, "Geometric effects on the mechanical strengths of strong nanocrystalline rhodium sub-micron structures," *Philos. Mag.*, no. April, pp. 1–15, 2014.

[80] J. R. Greer and W. D. Nix, "Nanoscale gold pillars strengthened through dislocation starvation," *Phys. Rev. B - Condens. Matter Mater. Phys.*, vol. 73, no. April, pp. 1–6, 2006.

[81] H. Zhang, B. E. Schuster, Q. Wei, and K. T. Ramesh, "The design of accurate micro-compression experiments," *Scr. Mater.*, vol. 54, no. 2, pp. 181–186, 2006.

[82] Y. M. Wang, S. Cheng, Q. M. Wei, E. Ma, T. G. Nieh, and a. Hamza, "Effects of annealing and impurities on tensile properties of electrodeposited nanocrystalline Ni," *Scr. Mater.*, vol. 51, no. 11, pp. 1023–1028, 2004.

[83] a. C. Lund and C. a. Schuh, "Strength asymmetry in nanocrystalline metals under multiaxial loading," *Acta Mater.*, vol. 53, no. 11, pp. 3193–3205, 2005.

[84] S. Cheng, J. a. Spencer, and W. W. Milligan, "Strength and tension/compression asymmetry in nanostructured and ultrafine-grain metals," *Acta Mater.*, vol. 51, no. 15, pp. 4505–4518, 2003.

[85] M. J. Burek and J. R. Greer, "Fabrication and microstructure control of nanoscale mechanical testing specimens via electron beam lithography and electroplating," *Nano Lett.*, vol. 10, no. 1, pp. 69–76, 2010.

[86] M. Hakamada, Y. Nakamoto, H. Matsumoto, H. Iwasaki, Y. Chen, H. Kusuda, and M. Mabuchi, "Relationship between hardness and grain size in electrodeposited copper films," *Mater. Sci. Eng. A*, vol. 457, no. 1–2, pp. 120–126, May 2007.

[87] B. Farrokh and A. S. Khan, “Grain size, strain rate, and temperature dependence of flow stress in ultra-fine grained and nanocrystalline Cu and Al: Synthesis, experiment, and constitutive modeling,” *Int. J. Plast.*, vol. 25, no. 5, pp. 715–732, 2009.

[88] R. K. Guduru, K. L. Murty, K. M. Youssef, R. O. Scattergood, and C. C. Koch, “Mechanical behavior of nanocrystalline copper,” *Mater. Sci. Eng. A*, vol. 463, no. 1–2, pp. 14–21, 2007.

[89] J. Chen, L. Lu, and K. Lu, “Hardness and strain rate sensitivity of nanocrystalline Cu,” *Scr. Mater.*, vol. 54, no. 11, pp. 1913–1918, 2006.

[90] S. Cheng, E. Ma, Y. M. Wang, L. J. Kecskes, K. M. Youssef, C. C. Koch, U. P. Trociewitz, and K. Han, “Tensile properties of in situ consolidated nanocrystalline Cu,” *Acta Mater.*, vol. 53, no. 5, pp. 1521–1533, 2005.

[91] H. Mughrabi and H. W. Höppel, “Cyclic deformation and fatigue properties of very fine-grained metals and alloys,” *Int. J. Fatigue*, vol. 32, no. 9, pp. 1413–1427, Sep. 2010.

[92] H. Mughrabi, “The cyclic hardening and saturation behaviour of copper single crystals,” *Mater. Sci. Eng.*, vol. 33, pp. 207–223, 1978.

[93] J. Schiøtz, “Strain-induced coarsening in nanocrystalline metals under cyclic deformation,” *Mater. Sci. Eng. A*, vol. 375–377, pp. 975–979, Jul. 2004.

[94] K. M. Youssef, R. O. Scattergood, K. L. Murty, J. a. Horton, and C. C. Koch, “Ultrahigh strength and high ductility of bulk nanocrystalline copper,” *Appl. Phys. Lett.*, vol. 87, no. 9, p. 091904, 2005.

[95] P. G. Sanders, J. a. Eastman, and J. R. Weertman, “Elastic and tensile behavior of nanocrystalline copper and palladium,” *Acta Mater.*, vol. 45, no. 10, pp. 4019–4025, Oct. 1997.

[96] C. J. Youngdah, P. G. Sander, J. A. Eastman, and J. R. Weertman, “COMPRESSIVE YIELD STRENGTHS OF NANOCRYSTALLINE Cu AND Pd,” vol. 37, no. 6, pp. 809–813, 1997.

[97] G. W. Nieman, J. R. Weertman, and R. W. Siegel, “Mechanical behavior of nanocrystalline Cu and Pd,” *J. Mater. Res.*, vol. 6, no. 05, pp. 1012–1027, Jan. 2011.

[98] J. Schiøtz and K. W. Jacobsen, “A maximum in the strength of nanocrystalline copper.,” *Science*, vol. 301, no. 5638, pp. 1357–9, Sep. 2003.

[99] T.-H. Fang, C.-I. Weng, and J.-G. Chang, "Molecular dynamics analysis of temperature effects on nanoindentation measurement," *Mater. Sci. Eng. A*, vol. 357, no. 1–2, pp. 7–12, 2003.

[100] K. Zhou, B. Liu, Y. Yao, and K. Zhong, "Effects of grain size and shape on mechanical properties of nanocrystalline copper investigated by molecular dynamics," *Mater. Sci. Eng. A*, vol. 615, pp. 92–97, Oct. 2014.

[101] Y. W. Zhang, P. Liu, and C. Lu, "Molecular dynamics simulations of the preparation and deformation of nanocrystalline copper," *Acta Mater.*, vol. 52, no. 17, pp. 5105–5114, 2004.

[102] K. Maekawa and a. Itoh, "Friction and tool wear in nano-scale machining—a molecular dynamics approach," *Wear*, vol. 188, no. 1–2, pp. 115–122, 1995.

[103] Y. Leng, G. Yang, Y. Hu, and L. Zheng, "Computer experiments on nano-indentation: A molecular dynamics approach to the elasto-plastic contact of metal copper," *J. Mater. Sci.*, vol. 35, no. 8, pp. 2061–2067, 2000.

[104] X. W. Zhou, R. a. Johnson, and H. N. G. Wadley, "Misfit-energy-increasing dislocations in vapor-deposited CoFe/NiFe multilayers," *Phys. Rev. B - Condens. Matter Mater. Phys.*, vol. 69, no. 14, pp. 1–10, 2004.

[105] M. W. Finnis and J. E. Sinclair, "A simple empirical N-Body Potential for Transition Metals," *Philos. Mag. A*, vol. 50, no. 1, pp. 45–55, 1984.

[106] J. Monk and D. Farkas, "Tension–compression asymmetry and size effects in nanocrystalline Ni nanowires," *Philos. Mag.*, vol. 87, no. 14–15, pp. 2233–2244, May 2007.

[107] S. J. Plimpton, "Fast parallel algorithms for short-range molecular dynamics," *J. Comput. Phys.*, 1995.

[108] M. Sun, F. Xiao, and C. Deng, "Near-ideal strength in metal nanotubes revealed by atomistic simulations," *Appl. Phys. Lett.*, vol. 103, no. 23, p. 231911, 2013.

[109] A. Stukowski, "Visualization and analysis of atomistic simulation data with OVITO–the Open Visualization Tool," *Model. Simul. Mater. Sci. Eng.*, vol. 18, p. 015012, 2009.

[110] A. Stukowski, V. V Bulatov, and A. Arsenlis, "Automated identification and indexing of dislocations in crystal interfaces," *Model. Simul. Mater. Sci. Eng.*, vol. 20, no. 8, p. 085007, 2012.

[111] S. Kumar, X. Li, A. Haque, and H. Gao, "Is stress concentration relevant for nanocrystalline metals?," *Nano Lett.*, vol. 11, no. 6, pp. 2510–2516, 2011.

[112] H. Van Swygenhoven, P. Derlet, and a. Hasnaoui, "Atomic mechanism for dislocation emission from nanosized grain boundaries," *Phys. Rev. B*, vol. 66, no. 2, pp. 1–8, 2002.

[113] Y. B. Wang, B. Q. Li, M. L. Sui, and S. X. Mao, "Deformation-induced grain rotation and growth in nanocrystalline Ni," *Appl. Phys. Lett.*, vol. 92, no. 1, pp. 2006–2009, 2008.

[114] A. Stukowski and K. Albe, "Extracting dislocations and non-dislocation crystal defects from atomistic simulation data," *Model. Simul. Mater. Sci. Eng.*, vol. 18, no. 8, p. 085001, 2010.

[115] A. Stukowski, K. Albe, and D. Farkas, "Nanotwinned fcc metals: Strengthening versus softening mechanisms," *Phys. Rev. B - Condens. Matter Mater. Phys.*, vol. 82, pp. 1–9, 2010.

[116] L. Lu, X. Chen, X. Huang, and K. Lu, "Revealing the Maximum Strength," vol. 323, no. January, pp. 2007–2010, 2009.

[117] J. Diao, K. Gall, M. L. Dunn, and J. a. Zimmerman, "Atomistic simulations of the yielding of gold nanowires," *Acta Mater.*, vol. 54, no. 3, pp. 643–653, 2006.

[118] C. Nan, X. Li, K. Cai, and J. Tong, "Grain size-dependent elastic moduli of nanocrystals," *J. Mater. Sci. Lett.*, vol. 7, pp. 1917–1919, 1998.